

Bioengineering Novel Reporter Proteins

by

Benjamin B. Bartelle

A dissertation submitted in partial fulfillment

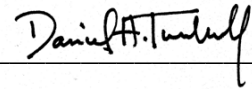
of the requirements for the degree of

Doctor of Philosophy

Department of Basic Medical Science

New York University

January, 2013



Daniel H. Turnbull

UMI Number: 3556976

All rights reserved

INFORMATION TO ALL USERS

The quality of this reproduction is dependent upon the quality of the copy submitted.

In the unlikely event that the author did not send a complete manuscript and there are missing pages, these will be noted. Also, if material had to be removed, a note will indicate the deletion.



UMI 3556976

Published by ProQuest LLC (2013). Copyright in the Dissertation held by the Author.

Microform Edition © ProQuest LLC.

All rights reserved. This work is protected against unauthorized copying under Title 17, United States Code



ProQuest LLC.
789 East Eisenhower Parkway
P.O. Box 1346
Ann Arbor, MI 48106 - 1346

DEDICATION

My mother for her courage

My father for his curiosity

My brother for his tenacity

AKNOWLEDGEMENTS

I would like to thank the following people for their support: Dan Turnbull for his ongoing support of the work covered in this thesis and demonstrating the level of patience necessary to conduct science *in vivo*; Alex Joyner for her invaluable advice regarding *in vivo* experiments; Jim Canary for his advice regarding Mn binding proteins and for sharing data critical for development of MntR; David Stokes for steering the committee, providing insights regarding metal pumps, and for admitting me into the program based on, “what the hell”; Glynn Johnson for his valuable insights regarding T1; Youssef Wadghiri for teaching me how to use the first MRI console. Brian Nieman for figuring out how to use the new one. Abby Deans and Jeff Blind for showing me how to handle mice and scan *in vivo*. Xin Yu for introducing me MEMRI and some interesting conversations; Cesar Berrios for collaborating on the Biotag project, and bumming around Berlin; Kamila Szulc for the laughter, tears and figuring out the T1 mapping protocol; Giselle Suero for showing that cancer research isn't so bad, changing my negative view of doctors and rescuing that mouse from the sharps container; Makis Parasaglou for pulse sequences, matlab scripts and scandal; Joe Rodriguez for countless surgeries, endless sectioning and general tomfoolery; Anne Friedland for her dedicated work on Biotag, suffering under my first foray as a manager and karmic retribution; David Bae for his contributions to wound response studies; Chris Parkhurst for generating bone marrow chimeras and bearing my pestering neuroimmunology questions; Katrin Deithart for providing reagents and suffering through a cloning collaboration; The Skirball Mouse Facility for taking care of my colony over the years; The Skirball Transgenic Facility for generating the

Biotag mouse and the extra 75 injections (111 and 121 were the winners!); The Skirball Flow Cytometry Core for sorting numerous stable cell lines and staying open late that one time; The NYU Center for Systems Biology for 24 hour access to their spinning disk confocal; Andrew Waight, for deft wit and spiritual counsel; Ryan Cinalli for the collegiality and late night conversations; Andrea Gomez for, also, doing everything the hard way; Rosemary Sherlock for sending me to Cold Spring Harbor; Rob Marteinssen for starting me in biology; Leslie Vosshall for critical career advice; Kevin Lee, Gilles Herrada, Brian Kloss, Walter Strapps and all of Sentigen for demonstrating how the pros do it; Andreas for the rescue operation; The Madagascar Institute for letting me keep all of my fingers; Todd, and Imagenode for the creative outlet and for “The Prototype”; Drapatz! for the weekly sanity check; NYCSparkworks for maintaining my fire for dance; Gwynn and David for my earliest concept of nature; and to Chuck, I still believe you could have made it.

Finally, and most of all to Miyeko Mana for her love and passion for life, research, dance, art, salt and rice. I love you. Thank you for everything.

PREFACE

Humans draw an incredible ability to conceptualize and interpret their environment from their visual system. We have highly developed brains that reconstruct the world in 3 spatial dimensions, in a panoply of colors of varying intensity, and a memory system to further interpret all these dimensions of information over time. Visualization is essential to understanding our world in any deep sense, whether it comes from direct viewing or internal modeling from abstract information. Our innate ability to create visual models has been fully employed to interpret ever more complex and abstract information into visual models, or maps, of the natural world. In practice, to the human mind, the representational can be even more significant than the real.

More than graphically reproducing the observable world, a representational map can render abstract information into a visual story about the real world. For example, in conceptualizing a geographical region such as a state, a map can provide more information than actually viewing the region from the air. In the map, topology and sociopolitical constructs such as cities and borders, have been codified into visual and sometimes written language to represent a body of information innate to the external world and yet invisible to the eye. Similarly, in our observation of the natural world, only a tiny fraction of life's processes are apparent. Organisms have visible

morphologies and measurable phenotypes, yet these are higher order effects of complex systems that express themselves in a language we cannot hear let alone understand.

To this end, the scientific community has developed a host of technologies to take in visual information beyond the capability of the unaided eye and express that information in a human readable format. At the most basic level, these are assistive technologies such as the ubiquitous camera and microscope. These devices supplement our innate vision and memory, but with these devices alone we are still limited to morphology and phenotype.

To visualize biology such as gene transcription or protein function, a fundamentally different technology has been developed. There are rare biological events can be observed directly, the most famous examples being antibody binding, DNA hybridization and the expression of the protein GFP. Using these technologies as visible analogs for otherwise invisible biological events has revolutionized biology. Now we race to generate comprehensive maps of gene expression in complex organisms and probe specific events using these technologies as new and artificial dimensions of information.

The work herein is a contribution of new technology to this branch of biological research. The existing technologies have their limitations, which this work evaluates and seeks to supplement, but like any reporter or biological probe, they remain the best available analog for the invisible processes of life.

ABSTRACT

Visualization of gene expression has led to a revolution in biology over the past two decades. Primarily this visualization has occurred using fluorescent proteins, like GFP, that can be directly visualized with microscopy. Fluorescence imaging is limited by depth of penetration when applied to living mice or humans however. For this, MRI, ultrasound and other modalities are under continual development for *in vivo* applications. Ideally, every *in vivo* imaging modality would have their own reporter genes, allowing for unconstrained genetic studies of structure and function. The current wealth of bioinformatics data presents a rich pallet of starting materials for bioengineering this next generation of reporter proteins.

This work utilized multiple approaches to creating reporters: cell labeling with, “Biotag” derived from a bacterial biotinylation enzyme and substrate; genetically controlled absorption of the MRI contrast agent Mn via the metal transport protein DMT1; and sequestration of Mn using the metal sensing transcription factor MntR. The reporter proteins were implemented in tissue culture and living mice to give a new view of gene expression in processes such as neural and vascular development. Moreover, the development process yielded new insights into the proteins themselves and the context in which they function. Each method has particular strengths and limitations but are, at present, the vanguard of *in vivo* molecular imaging.

TABLE OF CONTENTS

DEDICATION.....	iii
AKNOWLEDGEMENTS.....	iv
PREFACE.....	vi
ABSTRACT.....	viii
LIST OF FIGURES.....	xiv
1. INTRODUCTION.....	1
1.1. PRIOR ART:.....	1
1.2. MRI FUNDAMENTALS.....	4
B ₀ :.....	4
SPIN EXCITATION:.....	6
SPIN LATTICE RELAXATION:.....	6
FREE INDUCTION DECAY:.....	7
1.3. MRI CONTRAST.....	8
1.4. METALS AS CONTRAST AGENTS.....	10
IRON:.....	11
GADOLINIUM:.....	11
MANGANESE:.....	12
MEMRI:.....	14
A BIOLOGICAL CONTRAST AGENT:.....	15
1.5. AN ENGINEERING APPROACH TO TARGETED CONTRAST.....	16
TRANSFERRIN AND TRANSFERRIN RECEPTOR AS AN ARCHETYPICAL PROBE/TARGET SYSTEM:.....	20
AVIDIN-BIOTIN AS A BEST FIT SYSTEM:.....	23
CANDIDATE GENES FOR EXPRESSIBLE CONTRAST:.....	26
BIOLOGY OF INTERCELLULAR METAL TRANSPORT:.....	27

TRANSFERRIN AND TRANSFERRIN RECEPTOR:	28
FERROPORTIN FPN1:	29
MAGA:	30
DMT1 AND SLCA2 FAMILY TRANSPORTERS:	31
RATIONALE FOR A FOCUS ON DMT1:	32
1.7. SEQUESTERING METALS VIA METALLOPROTEINS.....	32
FERRITIN:	33
INTRACELLULAR MN TRANSPORTER, ATP2C:.....	34
MNTR:.....	36
1.8. OVERVIEW	38
BIOTAG OVERVIEW:	38
DMT1 OVERVIEW:	39
MNTR OVERVIEW:	39
VISUALIZING BIOLOGY WITH BIOLOGICAL CONTRAST:	40
2. A NOVEL GENETIC APPROACH FOR <i>IN VIVO</i> VASCULAR IMAGING IN	
<u>MICE</u>	<u>41</u>
2.1. ABSTRACT	42
2.2. INTRODUCTION.....	43
RESULTS	46
2.3. THE BIOTAG-BIRA EXPRESSION SYSTEM EFFECTIVELY BIOTINYLATES CELL	
MEMBRANES:.....	46
<i>Ts-BIOTAG</i> MICE DISPLAY BIOTIN ON EMBRYONIC VASCULAR ENDOTHELIAL CELLS:.....	52
<i>Ts-BIOTAG</i> EMBRYONIC VASCULATURE CAN BE TARGETED WITH AVIDINATED PROBES:.....	55
<i>IN VIVO</i> TARGETED ULTRASOUND IMAGING OF VASCULATURE IN <i>Ts-BIOTAG</i> EMBRYOS:	59
MULTIMODALITY IMAGING OF VEGF-INDUCED VASCULAR DEVELOPMENT:.....	62
2.4. DISCUSSION.....	71
2.5. METHODS	75
CELL TRANSFECTION AND BIOTINYLATION ASSAY:	75
IMMUNOCYTOCHEMISTRY / IMMUNOHISTOCHEMISTRY:	75
ANIMALS:.....	75
MATRIGEL PLUGS:.....	76
FLUORESCENCE AND NIR IMAGING:	76
UBM IMAGING AND GUIDED <i>IN UTERO</i> INJECTIONS:	76

MRI:.....	77
EXPRESSION CONSTRUCTS:.....	77
CELL TRANSFECTION AND BIOTINYLATION ASSAY:.....	78
IMMUNOCYTOCHEMISTRY / IMMUNOHISTOCHEMISTRY:.....	78
TRANSGENIC MICE:	80
ULTRASOUND CONTRAST AGENTS:.....	81
SYNTHESIS OF AV-DTPA-GD:	81
ULTRASOUND GUIDED MICRO-INJECTIONS:	81
UBM DATA ACQUISITION:.....	82
MICRO-MRI DATA ACQUISITION:	83
EMBRYO IMAGE ANALYSIS:.....	83
MATRIGEL DATA COLLECTION AND ANALYSIS:	84
2.6. ACKNOWLEDGEMENTS.....	85

DIVALENT METAL TRANSPORTER, DMT1: A NOVEL MRI REPORTER

PROTEIN	86
3.	86
3.1. ABSTRACT	87
3.2. INTRODUCTION.....	88
3.3. RESULTS	90
DMT1 EXPRESSION CORRELATES WITH MEMRI SIGNAL IN THE NEONATE MOUSE BRAIN: ..	90
DMT1 WITH MN SUPPLEMENTATION STRONGLY EFFECTS R_1 , A CRITICAL ASPECT OF MEMRI CONTRAST:	92
DMT1 EXPRESSION AFFECTS R_1 IN DIVERSE CELL TYPES WITH MN SUPPLEMENTATION AND CREATES CONTRAST FOR <i>IN VIVO</i> MEMRI:.....	95
ECTOPIC EXPRESSION OF DMT1 CREATES CONTRAST FOR <i>IN VIVO</i> MEMRI OF THE NEONATE MOUSE BRAIN:.....	100
3.4. DISCUSSION.....	102
3.5. METHODS	103
CLONING:	103
DMT1 STABLE CELL LINES:.....	104
PROTEIN EXPRESSION ASSAY:	104
MRI OF CELL LINES:	104
ANIMALS AND TUMOR MODELS:	106
<i>IN VIVO</i> MRI:	106
GFP IMAGING AND IHC:	107

STATISTICAL ANALYSIS:.....	107
3.6. ACKNOWLEDGEMENTS.....	108
4. DATA CHAPTER 3: BIOLOGICAL Mn CONTRAST WITH METALLOPROTEIN	
MntR	109
4.1. INTRODUCTION.....	110
4.2. RESULTS AND DISCUSSION.....	114
BACTERIAL EXPRESSION OF MNTR CREATES CELLULAR CONTRAST:.....	114
MNTR DOES NOT CREATE CONTRAST <i>IN VIVO</i> , IN MAMMALIAN CELLS:.....	115
FUSION TO THE GOLGI RESIDENT PROTEIN CAB45 LOCALIZES MNTR TO THAT ORGANELLE:.....	117
THE CAB45-MNTR FUSION PROTEIN IMPROVES R ₁ IN LIVE CELLS, CREATING <i>IN VIVO</i> CONTRAST:.....	118
MNTR EFFECTS R ₁ IN A PH DEPENDENT MANNER:.....	121
4.3. CONCLUSIONS.....	123
4.4. METHODS	125
BACTERIAL MNTR EXPRESSION:	125
CONSTRUCTS:	125
CELL STAINING:	126
STABLE CELL GENERATION:.....	127
RELAXOMETRY:	127
5. CONCLUSIONS ON ENGINEERING REPORTER GENES.....	129
SUMMARY OF CANDIDATE REPORTER PROTEINS:	129
5.1. BIOTAG	130
SUMMARY OF <i>Ts-BIOTAG</i> APPLICATIONS:.....	130
IMPROVING BIOTAG:.....	132
OTHER BIOTAG TRANSGENIC SYSTEMS:	134
5.2. DMT1	136
BBB PERMEABILITY OF Mn:	136
5.3. MNTR.....	139
INSIGHTS FROM MNTR STUDIES:.....	139
ALTERNATIVE TARGETING:.....	140
FUTURE WORK:	141
5.4. A METAANALYSIS OF ENGINEERING REPORTERS	144

6. <u>THOUGHTS ON THE EPISTEMOLOGICAL NATURE OF THIS THESIS:</u>	150
7. <u>APPENDIX 1: IN VIVO STUDIES OF TIE2 EXPRESSION USING THE TS-BIOTAG MOUSE.....</u>	153
7.1. INTRODUCTION.....	153
THE RECEPTOR TYROSINE KINASE TIE2:	154
TIE2 EXPRESSION:.....	155
7.2. RESULTS AND DISCUSSION.....	158
ADULT EXPRESSION OF TIE2:.....	158
TS-BIOTAG OUTSIDE OF THE VASCULATURE:	160
TS-BIOTAG ANIMALS IN A MODEL OF ACUTE INJURY:.....	162
TS-BIOTAG MICE EFFECTIVELY LABEL THE VASCULATURE DURING RESPONSE TO A PERIPHERAL INJURY:.....	163
THE CRYO MODEL OF NEUROINJURY:	165
7.3. CONCLUSIONS.....	167
8. <u>APPENDIX 2: ANALYSIS OF Mn UPTAKE AND EXCRETION BY T₁ RELAXOMETRY.....</u>	169
8.1. INTRODUCTION.....	169
8.2. RESULTS AND DISCUSSION.....	169
R ₁ IS AN ANALOG MEASUREMENT OF THE FIRST ORDER KINETIC RATE:.....	169
R ₁ MEASUREMENTS ASSAY CELL TYPE DEPENDENT MN RETENTION:.....	171
DISTINCT TIMECOURSE R ₁ PROFILES REFLECT DIFFERENT MECHANISMS OF MN EXCRETION:.....	173
R ₁ RELAXIVITY MEASUREMENTS SHOW A NONLINEAR RELATIONSHIP BETWEEN DMT1 EXPRESSION AND MN UPTAKE:.....	173
R ₁ RELAXIVITY IS AN ANALOG FOR THE MN UPTAKE RATE BY DMT1:	175
8.3. CONCLUSION.....	178
9. <u>BIBLIOGRAPHY.....</u>	179

LIST OF FIGURES

Figure 1.1 NMR Zeugmatography	2
Figure 1.2 First publication of ectopic GFP expression.	4
Figure 1.3 Structural view of Transferrin bound to its receptor.	23
Figure 1.4 Structural model of Avidin monomer bound to biotin.	25
Figure 2.1 Schematic of the Biotag reporter system.....	48
Figure 2.2 Co-localization of Biotag and BirA ^{ER} in expressing cells	49
Figure 2.3 Co-expression of Biotag and BirA ^{ER} results in membrane biotinylation.....	51
Figure 2.4 Western blot analyses of transgene levels in Ts-Biotag lines.....	54
Figure 2.5 Ts-Biotag embryonic vasculature is biotinylated but otherwise similar to WT	55
Figure 2.6 Targeted μ -MRI imaging of embryonic vasculature in Ts-Biotag mice.	57
Figure 2.7 E11.5 Ts-Biotag embryonic Tie2 expressing vasculature is bound by avidinated probes.	58
Figure 2.8 UBM imaging of vasculature in Ts-Biotag embryos.....	61
Figure 2.9 Targeted UBM of embryonic vasculature in Ts-Biotag mice.....	62
Figure 2.10 Matrigel plug vasculature is permeable to DTPA-Gd.....	65
Figure 2.11 Targeted fluorescence and NIR imaging of VEGF-induced neovasculature in Ts-Biotag mice.	69
Figure 2.12 Targeted MRI of VEGF-induced neovasculature in Ts-Biotag mice.	70
Figure 3.1 DMT1 expression and MEMRI signal are correlated in the neonatal mouse brain.	91
Figure 3.2 Effect of cellular DMT1 expression on MEMRI signals.....	94
Figure 3.3 MRI analysis of DMT1 expression in B16 cells, in vitro and in vivo.....	98

Figure 3.4 MRI analysis of DMT1 expression in GL261 cells, in vitro and in vivo.	99
Figure 3.5 In vivo MRI analysis of ectopic DMT1 expression in the developing mouse neocortex.	101
Figure 4.1 Metalloenzymes occlude Mn from the H spin lattice.....	112
Figure 4.2 The Mn binding motif of MntR is structurally similar to a chelated contrast agent.	113
Figure 4.3 Bacterial cells expressing MntR yield significant contrast compared to control cells.	115
Figure 4.4 MntR induced contrast in Live vs Fixed HEK cells.	116
Figure 4.5 MntR fusion proteins localize to the Golgi	118
Figure 4.6 R_1 comparison of Mn supplemented HEK cells expressing MntR fusion proteins and DMT1	120
Figure 4.7 R_1 comparison of 24h post Mn supplementation HEK cells expressing MntR fusion proteins and DMT1.....	121
Figure 4.8 R_1 enhancement of ^{55}Mn MntR ^{ER} is dependent upon pH.....	123
Figure 7.1 Overview of Tie2 Protein Signaling:.....	155
Figure 7.2 Tie2 Expression:.....	158
Figure 7.3 Ts-Biotag labeling in tumors	159
Figure 7.4 Avidin-FITC and Iba1 staining in E11.5 embryos	161
Figure 7.5 NIR scans of ear injury response.....	165
Figure 7.6 MRI of cryo-injury in WT and Ts-Biotag mice	166

Figure 8.1 Retention of R_1 as an analog for Mn in multiple cell types. 172

Figure 8.2 Plot of relaxivity vs relative DMT1 expression 175

1. INTRODUCTION

1.1. PRIOR ART:

In 1973 Paul Lauterbur demonstrated a method of spatially encoding nuclear magnetic resonance (Lauterbur 1973) (**Figure 1.1**). In addition to showing spatially encoded signal from two samples of equal proton density, Lauterbur demonstrated that differences in the paramagnetic properties between the samples, due to dissolved $MnSO_4$, resulted in differing signal intensities. Though this technology developed into MRI, Lauterbur himself did not consider his results an image. Instead he named the technique zeugmatography, in effect a map, with spatial information and signal intensity from proton density and magnetic resonance. Changing elements of magnetic resonance can alter relative signal intensities, highlighting differences in magnetic properties and proton densities between tissues in the form of contrast without alter spatial information. In this way, specific tissues can be highlighted based on their innate magnetic resonance properties. Even with almost 40 years of advances this remains the fundamental concept behind MRI.



Figure 1.1 NMR Zeugmatography

The first image generated by MRI, or “NMR Zeugmatography.” Dark spots correlate to 1mm inner diameter tubes of H₂O within a 4.2mm diameter tube of D₂O. The image was generated by combining 4, 1D projections along 20 points for a 20X20 pixel 2D image. (Lauterbur 1973)

One year after Lauterbur’s seminal paper, green fluorescent protein (GFP) was isolated and characterized. Early work on GFP was focused on the extraordinary beauty created by the protein in the form of bioluminescence. GFP itself is not luminescent, but electron transfer to GFP causes excitation. GFP could be similarly excited with a blue light (395 and 470nm), allowing the researcher to literally see the protein. It followed then that if a gene product in the form of a protein could be directly imaged, then expression of GFP would serve as an analog or “reporter” of genetic expression. It took 20 years to realize this potential by Chalfie and colleagues (M Chalfie et al. 1994) (**Figure 1.2**). Visualizing GFP is, in fact, mapping gene

expression with the substitution of a visible analog for the actual, invisible, protein of interest. Furthermore, GFP could be fused to other proteins to serve as a map of protein localization. In these images, spatial information and signal intensity are derived solely from the presence and concentration of the reporter/protein fusion. Over a few years numerous other GFP related proteins were developed for photon based imaging in the visible spectrum. Conceptually these technologies are classified as “reporters,” “reporter genes,” or, more accurately “reporter proteins”(Roger Y. Tsien 1998).

GFP has seemingly little to do with MRI, but both are conceptually related in that they are technologies for mapping biologically relevant information *in vivo*. Because the resultant maps from these technologies are derived directly from real data with often seamless processing it is easy to forget that they are not simply images. This conceptual decoupling of MRI and reporter proteins from direct imaging is absolutely necessary to realize the real potential of these technologies. “Imaging” with either method is not limited to pure observations, but can be spatially complex readouts of any number of experimental perturbations. It is only within this paradigm that the potential of combining a reporter protein as a versatile platform for probing genetics and MRI for minimally invasive, volumetric collection of data can be conceptualized.

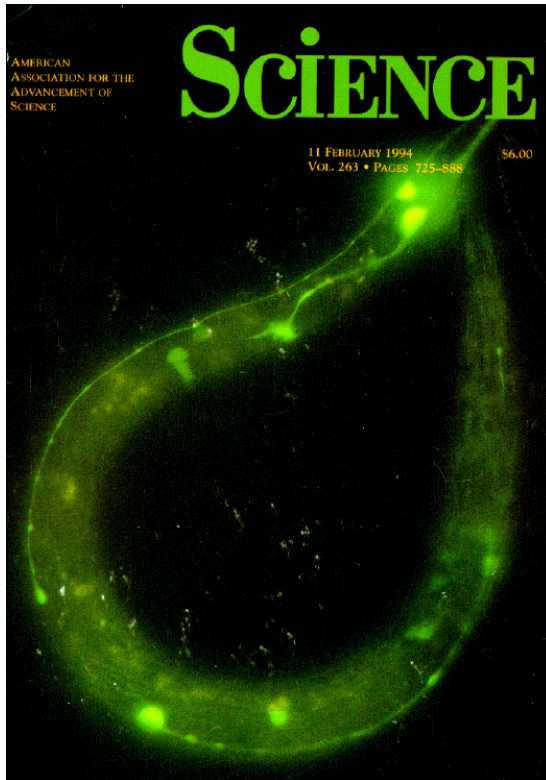


Figure 1.2 First publication of ectopic GFP expression.

The first image of GFP ectopically expressed in a transgenic organism. GFP is driven by the promoter for *mec-7* or beta tubulin which is abundant in only 6 of the ~300 *C. elegans* neurons. This allows for the direct visualization of specific cell types *in vivo*. (Chalfie 1994)

1.2. MRI FUNDAMENTALS

The dynamics of spin systems as they relate to NMR signal and MRI have been elucidated in many textbooks (Nishimura, 1996; Haacke 1999; Bloch, 1953; Purcell, 1985; Fox and Rabi, 1935). The following is a summary of only the elements that pertain to NMR signal and contrast that are critical for understanding subsequent chapters. This overview ignores most elements of, spatial encoding, pulse sequence design, and image reconstruction as they are beyond the scope of this thesis.

B₀:

As described by Larmor over 100 years ago and later by Rabi, all

subatomic particles have innate spin. In nuclei with an even number of protons and neutrons the spins will cancel each other out, but in noneven nuclei, most relevantly the single proton in H, there will be a non-zero net spin and their own magnetic moments. Outside of a magnetic field the spins, and resultant magnetic moments are randomly distributed and the net magnetic moment is zero. However when a magnetic field (\mathbf{B}_0) is applied, the individual magnetic moments will align with \mathbf{B}_0 into net magnetization with distinct energy levels. This organization of spins within \mathbf{B}_0 is called the Zeeman interaction. Roughly stated, the detectable energy levels are directly proportional to \mathbf{B}_0 and the two possible spin states ($\pm 1/2$). The transition between these two states (ΔE) can be induced and measured by excitation with electromagnetic radiation with a matching ΔE , as described by the Planck-Einstein equation.

$$\Delta E = \hbar\omega$$

Here, \hbar is Planck's reduced constant and the angular frequency of the exciting photon is ω . The angular frequency in this case is known as the Larmor frequency or ω_0 .

$$\omega_0 = \gamma \mathbf{B}_0$$

In a typical MRI experiment \mathbf{B}_0 is the known field strength of the magnet and γ is the angular momentum for the nucleus being probed. For example, γ for the single proton of the H^1 nucleus is ($2.675 \cdot 10^8 \text{ rad s}^{-1} \text{ T}^{-1}$). In a 7T magnet,

which all MR experiments here in were conducted the Larmor frequency would be $\sim 300\text{MHz}$, and often magnets used for NMR are described in this way.

Spin excitation:

The basis of NMR is the detectable phenomenon of nuclei changing states when absorbing and emitting their requisite amount of energy. Given the large population of nuclei that must be excited in order to measure the phenomenon, this process is not instantaneous, nor can an emission event be predicted for individual nuclei. Instead, the net magnetization of a population of dipoles in the excited state is treated as a bulk magnetization vector **M**.

M is excited from the ground state by applying a transverse magnetic field, **B**₁, oscillating at ω_0 . This forces the magnetization vector **M** to precess simultaneously about **B**₁ and **B**₀, creating the resonance phenomenon.

Spin Lattice Relaxation:

Ignoring the precession around **B**₀, after excitation, **M**, gradually returns to its ground state in a process called relaxation. Again, the rate at which this happens cannot be determined for a specific nuclei as energy is broadly transferred throughout the system, or “spin lattice,” which is heavily influenced by factors external to the individual spins. Instead, the average rate of relaxation for **M** can be measured. The Bloch theory of NMR describes the

macroscopic relaxation of \mathbf{M} along the z-axis as being an exponential process where T_1 is a first order time constant.

$$M_z(t) = M_z(0)e^{(-t/T_1)} + M_0(1 - e^{(-t/T_1)})$$

Based on this general formula, T_1 can be measured and calculated based on signal recovery from a saturating 90° pulse, where $M_z(0) = 0$. This saturation recovery method is used extensively here in for accurate measurement and comparison on T_1 in different samples. Experimentally signal intensity is directly related to $M_z(t)$ where t = the relaxation time within a pulse sequence (TR). Relaxation times over $5xT_1$ are required for nearly complete longitudinal relaxation (>99%). At 7T the T_1 of pure H_2O is $\sim 3s$, making full relaxation impractical for a typical imaging protocol.

Free Induction Decay:

In addition to the longitudinal component of relaxation M_z , An excitation pulse has transverse components M_x and M_y . Rather than relaxing back to a ground state these components of \mathbf{M} rapidly decay by dephasing of the individual spins known as the free induction decay. Bloch equations describing the macroscopic effects for these components are much simpler than for longitudinal relaxation.

$$M_x(t) = M_x(0)e^{(-t/T_2)}$$

$$M_y(t) = M_y(0)e^{(-t/T_2)}$$

In both equations, T_2 is a time constant determining the rate of decay. Free induction decay is a much faster process than relaxation with the T_2 of H_2O at 55ms at 7T.

Finally T_2 is highly sensitive to inhomogenaities in B_0 , any sample has specific magnetic susceptibilities that can change the field especially at interfaces between different tissues. These incidental effects contribute to T_2 in hard to predict ways. The sum of these effects are denoted as T_2^* and, while related to T_2 , are distinct.

1.3. MRI CONTRAST

As we have seen, the signal of a given sample is dependent upon the density of protons and their innate relaxivity in a magnetic field. This holds true for a simple tube of water to every voxel in an image. In a complex object such as a biological sample the T_1 , T_2 and T_2^* relaxivity can come from a wide range of sources. Importantly, while MRI signal is based on nuclear spin, relaxivity is influenced mostly by electromagnetic effects. This means that the electron interactions that comprise all types of chemical bonding can influence relaxivity and hence MRI signal. Molecules that are polar, such as water or soluble amino acids, can produce a weak diamagnetic effect that somewhat counteracts the external magnetic field. This means that an H^1 proton covalently bound to a carbon such as in fatty acids will have a very different relaxivity from an H^1 proton of water. These differences in relaxivity are

readily apparent in an image and are the basis for proton MRI, since every tissue has its own distinct profile of H^1 protons.

Diamagnetism is very weak compared to paramagnetism. Just as nuclear spin comes from all protons and neutrons, paramagnetism is derived from the quantum spin moments of all orbiting electrons. While all electrons exert this effect, quantum stacking causes electrons sharing an orbital to have opposite spins canceling out their paramagnetism unless there are unpaired electrons in the atom's orbitals. The magnetic moments of all paramagnetic atoms are randomly distributed unless exposed to an external magnetic field. In an applied field the paramagnetic moments align with the field, thus augmenting the field and the relaxivity of nearby H^1 protons. Paramagnetism is an extremely local effect, altering the relaxivity only of H^1 protons a paramagnetic atom is bound to (inner sphere effects) or comes into direct contact with (outer sphere effects). While the paramagnetic effect is considered microscopic, this is not accurately descriptive of longitudinal relaxation since T_1 changes are distributed throughout the spin lattice. As long as there is free exchange of water bound H^1 protons T_1 effects are only limited by diffusion rates.

Finally, some atoms have permanent electron spin couplings that can produce their own magnetic fields in absence of an external field. This is ferromagnetism and these independent magnetic fields can be much more

powerful than that of a paramagnetic atom. Ferromagnetic atoms can exert their own fields beyond a sphere of direct interaction, called a mesoscopic effect. At high concentration ferromagnetic atoms can effectively spoil applied external fields, altering T_2 and T_2^* relaxivity.

Diamagnetic, paramagnetic and ferromagnetic effects can all be at play in a single molecule, and every atom in the environment will affect the relaxivity of an H^1 proton at a micro, meso and even a macroscopic level. The relaxivity of any given voxel is therefore the complex product of T_1 , T_2 and T_2^* combined.

1.4. METALS AS CONTRAST AGENTS

Given a similar proton density in a sample, the signal in a specific region is determined by T_1 , T_2 or T_2^* relaxivity. All tissues have their own distinct profile of T_1 , T_2 and T_2^* and with careful crafting of the MR imaging protocol, differences in these 3 factors can be highlighted in a sample, thereby creating “contrast.” Optimizing a protocol based on endogenous T_1 , T_2 and T_2^* to highlight a specific tissue or pathology however can be time consuming and often differences in relaxivity are too minor to visualize. To improve contrast and selectively enhance tissues there has been extensive research into molecules featuring atoms that exert a para or ferromagnetic effect to change contrast. There are many such “contrast agents” but 3 make up the vast majority of contrast-enhanced imaging and thus are the only agents explored

in this work (Krause 2002). Each has unique properties that make it appropriate for specific applications.

Iron:

Iron (Fe) can be either or both paramagnetic and superparamagnetic, depending on the molecule or material and physical conditions. Fe, in the form of Ferric oxide nanoparticles, exerts a superparamagnetic effect on surrounding H at macroscopic distances. This disrupts the local magnetic field and exerts an effect primarily on T_2 and T_2^* generally creating negative contrast (Bulte & Kraitchman 2004). Despite the less appealing loss of signal, Fe does have the distinct advantage of exerting a stronger T_2^* effect at high field strength. Here the superparamagnetic effect of a single iron nanoparticle can be enough to saturate an entire voxel. This, coupled with the biological phenomenon of cells actively absorbing nanoparticles, has recently enabled single cell detection *in vivo* using commercially available Fe oxide based contrast agents.

Gadolinium:

With 7 electrons in an unpaired orbital creating a powerful paramagnetic and superparamagnetic effect, Gadolinium (Gd) causes the largest change to T_1 relaxivity of any atom discussed here, and is the most commonly used contrast agent in MRI (Krause 2002). Unfortunately Gd is not a biologically endogenous metal. In fact, the free metal ion Gd is very toxic to cells and

whole organisms so Gd must be bound to an organic molecule or chelator. The tight interactions necessary for binding reduce almost all of its inner sphere effects and a large portion of outer sphere effects, with an overall reduction in relaxivity around 75%. Furthermore, Gd relaxivity further reduces with increasing field strength above 0.1T. Despite the loss of efficiency, Gd still causes a readily detectable contrast even high field strength.

Despite being necessarily bound to a chemical chelator Gd offers the advantage of being soluble and freely diffusible. The FDA approved agent diethylene-triamine-pentaacetic-acid-gadolinium (Gd-DTPA or Magnevist) is commonly injected into experimental mammalian models and in human subjects to image enhanced contrast as it circulates through the vasculature or to detect leaks in blood vessels from a hemorrhage or vascular malformation. Perhaps because of the need for a chemical chelator of Gd, a fast growing field of molecular imaging is the conjugation of a chelated Gd to a targeting molecule. Chelated Gd can be easily conjugated to synthetic chemicals or large proteins such as antibodies in order to target contrast in a biologically significant way (Artemov 2003). This concept will be explored in later chapters.

Manganese:

Since the earliest development of MRI, Mn has been recognized as an effective contrast agent (Lauterbur 1973). A paramagnetic ion with 5 unpaired

electrons, Mn shortens the T_1 relaxation time of water molecules at microscopic scale. In solution, Mn can complex with up to 7 protons which exchange many times over the millisecond time spans used in MRI creating strong inner and outer sphere effects as a free ion. Like Gd, its paramagnetic effect on H^1 proton relaxivity is greatly reduced with increasing field strength (Krause 2002).

Mn is a common, naturally occurring metal essential for normal physiology in trace amounts, meaning it does not need to be chelated when used as a contrast agent. Due natural interaction though, Mn is usually biologically chelated *in vivo* (M. Aschner et al. 1999). This natural chelation takes the form of porphyrin rings in many plant pigments and as a cofactor in enzymes such as superoxide dismutase (Guan et al. 1998), arginase (Ilies et al. 2010), or glutamine synthetase (Krajewski et al. 2008). Mn is utterly essential for proper health. While no Mn deficiency related diseases have been reported, experimentally an Mn sparse diet causes skin lesions, bone malformation and epileptic seizures (J. A. Roth & M. D. Garrick 2003). Though necessary as a trace mineral, high levels of Mn can be neurotoxic and both acute and chronic exposure can cause a form of heavy metal poisoning called Manganism (J. A. Roth & M. D. Garrick 2003). There is considerable evidence that free Mn ions can enter the brain, be internalized by neurons via calcium channels and transported along axons and across

synapses (Aschner et al., 1999; Yokel et al., 2003; Crossgrove and Yokel, 2004; Crossgrove and Yokel, 2005). Mn's penetrance into the brain and its tendency to accumulate for up to several days make it very useful as a contrast agent for neuroimaging in small animals (Massaad & Robia G Pautler 2011). Mn enhanced Imaging (MEMRI) is rapidly establishing itself as a field unto itself and will be explored more thoroughly in later chapters.

MEMRI:

The ability of Mn to improve tissue specific contrast, especially in the brain, has been well documented (Aoki et al. 2004). Furthermore, despite known toxicity, MEMRI causes seemingly little harm to mice even when administered repeatedly over several weeks (Bock et al. 2008). What actually causes the selective uptake of Mn and protection from chronic exposure is less understood, but some mechanisms have been elucidated as MEMRI grows as a methodology. Ca^{+2} channels are nonselective and will take up Mn when opened (Narita et al. 1990). Since Ca^{+2} channel opening is a common cellular response to stimuli meaning that most active cells should be permeable to Mn^{+2} . Furthermore, in neurons, locally introduced Mn^{+2} is observed to travel down axons, passing into other neurons presumably via exocytosis and reuptake via the Ca^{+2} channels, active at synapses (Robia G Pautler 2004). These two properties lead to Mn^{+2} labeling active cells in the brain, spreading over the course of hours providing increased labeling in

areas of particularly high activity (Yu et al. 2005).

This would seemingly make Mn the optimal contrast agent for neuroimaging, but there are certainly caveats. Most importantly, Mn^{+2} does not freely cross the BBB (Yokel et al. 2003). There is definitely some transport across the BBB at a low rate, most likely via Ca^{+2} channels and Fe based transport mechanisms. Based on MRI results significantly more Mn^{+2} enters the CSF, diffusing through the brain via the ventricles (Aoki et al. 2004). This means that broad diffusion of Mn takes up to 24 hours, precluding short-term experiments regarding differential Mn uptake without disrupting the BBB. Given the complexity of systemic Mn uptake, especially in the brain, Mn availability will continue to be an issue, even with a cellular uptake mechanism.

A Biological Contrast Agent:

All of these metals can be chelated to an organic molecule, which in turn can be manipulated using biochemical methods (Krause 2002). Theoretically one could take advantage of the plethora of antibodies or RNAs or other biological probes available to target the contrast to any biologically relevant molecule such as a protein or nucleic acid (Artemov 2003). Certainly these methods have been tried, with some success, however practical limitations complicate any such strategy. Chelating molecules and targeting probes are large and usually membrane impermeable, SNR is too limited for

single molecule detection and biological targets are often too sparse for effective labeling. These technical hurdles are not entirely intractable, but they push the limitations of what can be done using endogenous targets, hence the impetus for developing genetically expressible contrast agents. Transgenic technology offers the advantage of developing a single chemical agent and engineering the genetics of the mouse for each application. This requires months rather than years of development, though it is necessarily limited to model organisms.

How then can the expression of a protein result in detectable contrast with MRI? Much like with GFP, there must be an underlying biological phenomenon to reappropriate into detectable signal. There is no obvious first order technology like fluorescence in MRI making direct protein imaging impractical. MRI signal is based, obviously, on magnetic resonance, and while proteins themselves may not be innately magnetic, to any great degree, the function of a protein could potentially create a second order effect that would alter magnetic resonance by binding or accumulating contrast agent. Using this line of reasoning this work explores several strategies to utilize a biological and genetically encodable phenomenon to localize a magnetic resonance effect.

1.5. AN ENGINEERING APPROACH TO TARGETED CONTRAST

The advent of contrast-enhanced imaging has been of vital importance

to MRI. Consequently, there has been extensive development of contrast agents both chemically and biologically. First generation MR contrast agents are relatively simple chemicals with an innate chemical or physical property that provides a unique pattern of contrast upon exposure to tissue (Krause 2002). For example, Gd-DTPA freely diffuses through the bloodstream and, being a small molecule, readily leaks out of poorly formed vasculature. This simple property makes Gd-DTPA the most frequently used clinical contrast agent for highlighting vasculature and for identifying hemorrhages, pathological vasculature, and tumors (de Roos et al. 1988). In contrast, Fe nanoparticles are large and do not pass through vasculature very well. However, many cell types take them up by phagocytosis (Bulte & Kraitchman 2004). Consequently, cellular explants, when incubated with Fe-nanoparticles will take up the labels, allowing them to be tracked.

Research has moved beyond reliance on fortuitous properties of chemical agents, rather extensive efforts have been made to engineer second generation contrast agents that selectively target certain cells or tissues (Artemov 2003). Antibodies and binding peptides have been conjugated to contrast agents to target a variety of proteins, including $\alpha_v\beta_3$ -integrin (Rüegg & Alghisi 2010), epidermal growth factor (EGF) (Agarwal et al. 2008), transferrin receptor (TfR) (Agarwal et al. 2008), membrane metalloprotease-2

(MMP-2) (Stollman et al. 2009), and vascular endothelial growth factor receptor (VEGFR) (Ferrara & Kerbel 2005). Since the endothelial cell surface is accessible by intravascular injection, contrast agents can be delivered by the circulation and generally have some time to bind their targets before being cleared by the liver and kidneys.

A real conceptual strength of targeting is the modularity of the system. There are in fact a host of alternative *in vivo* imaging modalities that are in many ways comparable to MRI. Methods available for small animal micro-imaging include bioluminescence (Prescher & Contag 2010), near infrared (NIR) (Hilderbrand & Ralph Weissleder 2010), ultrasound biomicroscopy (UBM) (Colin K L Phoon & Daniel H Turnbull 2003), micro-positron emission tomography (micro-PET) (Rowland & Cherry 2008), optical coherence tomography (OCT) (Hielscher 2005). Each method has its various strengths and weaknesses but in general they offer enhanced tissue penetration compared to light microscopy at the expense of resolution. Indeed with the particularities of each imaging modality it is often advantageous to conjugate different types of imaging agents onto a single targeting molecule. So called, multi-modality agents are often macromolecules with hundreds or thousands of polymerized targeting and imaging molecules such as multifunctional dendrimers or fluorescent nanoparticles (McCarthy and Weissleder, 2008; Wängler et al., 2008).

With such versatility, targeted imaging is a rapidly expanding area of research, however the field has some clear limitations. There is the obvious drawback that targeted agents will only work if their binding partner is somehow exposed to the vasculature. This limits agents to cell surface molecules that are exposed to the vascular system. Another potential limitation of targeted contrast agents is the relatively low binding affinities to their cognate receptors. Native receptor-ligand partners have affinities appropriate for reversible binding, and even antibodies have a wide range of dissociation constants (K_d). As a result, *in vivo* binding may be inefficient and take a substantial amount of time, which limits both sensitivity and temporal resolution for targeted contrast-enhanced imaging. In the case of targeted contrast particles for vascular imaging, fluid shear forces may also preclude binding to high flow regions, creating localization artifacts (Takalkar et al. 2004). Development of a robust targeting agent is not a trivial matter. Antibodies are plentiful in terms of variety, but remain expensive to produce and often lack the affinity for *in vivo* applications. Short peptides or DNA aptamers are much easier to manufacture, but here, screening for sufficient binding affinity is an even more laborious process.

From the viewpoint of a researcher developing targeting agents for clinical use, these are unavoidable obstacles. Any agent developed must be biologically active only along the narrowest parameters to avoid unwanted

side effects. Devising improved methods to identify new biologically relevant targets and overcoming the technical hurdles to develop a targeted agent is a major area of interest for the field of molecular imaging.

Clinically, targeted imaging is limited to the biochemistry of the agent alone, however basic research has a somewhat different paradigm. The use of model experimental animals allows for both engineering of not just the agent, but also the animal itself. Transgenic technology is a powerful, extensive, and increasingly affordable tool set for basic research. The current amount of time and effort to identify and isolate a gene can be almost trivial compared to the often vast resources required to develop a small molecule that is specific to even a well known gene product. Given these constraints, utilizing a single targeting system that can be genetically encoded, as a reporter protein, offers distinct advantages over engineering probes for endogenous proteins. This single, reusable, tagging strategy affords the luxury of engineering both probe and a target that are ideal for *in vivo* imaging applications. The requirements for the targeted agent have already been discussed. Meanwhile the composition of an ideal target has not been explored.

Transferrin and Transferrin Receptor as an Archetypical Probe/Target System:

To properly design and probe and target system it is necessary to

understand prior art. The best known example of a semi artificial targeting system is transferrin and its receptor which have been used previously with mixed success (Moore et al., 1998; Gilad et al., 2007b). Analyzing the strengths and faults of transferrin (Tf) and its receptor (TfR) as an archetypical system we can properly assess the parameters of probe/target design. In the published structure of conjugated Tf/TfR, we can see the anatomy of a receptor ligand binding pair (**Figure 1.3**) (Cheng et al. 2004). TfR exists as a dimer, a common feature for many receptors. The seam of the binding face of the TfR dimer is also the binding surface for 2 Tf molecules. This broad binding face engages both the homologous N and C terminal lobes of Tf. Despite the large binding surface the Tf/TfR complex is completely reversible and highly sensitive to pH changes.

The Tf/TfR binding relationship may be highly optimized for its purpose, but as a platform for targeting imaging, there are some areas that can certainly be improved upon. Tf/TfR suffers from a major limitation of specificity. Transferrin binds to its receptor with a K_d of $10^{-9}M$. Nanomolar affinity is essential for reversible binding, but insufficient considering the *in vivo* demands of an agent for vascular labeling. Shear forces can overcome such a low affinity in high flow models, especially when large nanoparticles or microbubbles are the agents in question (Takalkar et al. 2004). Also, consider the large binding area of Tf/TfR binding and sensitivity to structural changes.

Attaching imaging probes to Tf could easily disrupt the binding surface directly or indirectly by shifting the structure slightly. These structural considerations, along with the ubiquity of TfR expression, make Tf/TfR one of the worst possible choices for targeting scaffolds.

Understanding the strengths and weaknesses of this system inform engineering efforts. In contrast to Tf/TfR and ideal scaffold would have a binding affinity well below nM concentrations. Rather than being optimized for reversibility, the target and ligand should be insensitive to physiological changes and non-reversible. Also, instead of having a broad and exposed binding surface that could be spoiled by chemical labeling, the binding motif should be small and recessed to reduce the odds of accidental labeling. Finally, like the Tf/TfR complex, the ligand or receptor could be multimeric as long as there was only one repeating binding motif. While this may increase the amount of labeling per unit area, the main advantage of more potential binding sites would be improved kinetics, as the likelihood of interaction is increased as the number of sites per unit of protein increase.

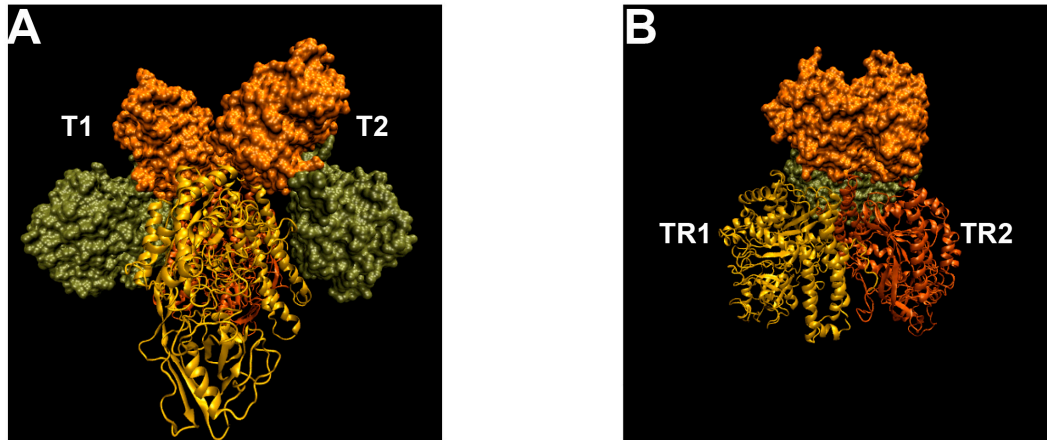


Figure 1.3 Structural view of Transferrin bound to its receptor.

In a side view of the Tf/TfR complex, 2 Transferrin molecules (T_1 T_2) are bound at both N (orange) and C (green) terminal ends (PDB ID 1SUV)(Cheng et al. 2004)(**A**). In a top view of a single Tf molecule bound show the large binding surface involved in the complex (**B**).

Avidin-Biotin as a Best Fit System:

With the above criteria the avidin/biotin complex offers the best available properties for a targeting scaffold. The avidin/biotin interaction is the strongest noncovalent bond in biology (O. H. Laitinen et al. 2007). With a K_d of $10^{-15}M$, it is irreversible under physiological conditions and serves as an effective antibiotic by scouring all available biotin from the egg white from which the protein is derived. Biotin is a small molecule that recognizes a narrow binding cleft on one monomer of avidin (**Figure 1.4**), and heavy labeling of avidin does very little to reduce its binding efficiency. Avidin naturally occurs as a tetramer, but monomeric mutants are common. Recognition of the avidin biotin system has led to its widespread use in biotechnology (Laitinen et al.,

2007; Fernández-Suárez et al., 2008). Nearly every imaging agent commercially available has been conjugated to either avidin or biotin, and kits are readily available for benchtop conjugation to novel agents. From the standpoint of a biologist with limited access to complex chemistry this presents an additional attractive design feature.

Since biotin is a small molecule it would initially make sense to use avidin expressed on the surface of the cell as a tag, however given the irreversibility of binding and the apparent ubiquity of biotin this is an inadequate strategy. This means biotin must be used as the tag and some of the avidinated agent will be neutralized by free biotin. The amount of avidin that is neutralized varies depending on the experimental context, but this limitation is probably the weakest aspect of the avidin/biotin system. Since biotin cannot be directly expressed, it must be conjugated to a protein, fortunately a common biological process (Bagautdinov et al. 2008). As a small molecule, multiple biotins can be displayed at high density, maximizing the chance of a collision leading to binding.

The above design precepts were employed in an experimentally demonstrable optimal synthetic tagging system. We explore the application of the synthetic tag in a transgenic mouse, a powerful research tool in its own right. Ramifications and further applications of the transgenic animal and the tagging technology will be discussed.

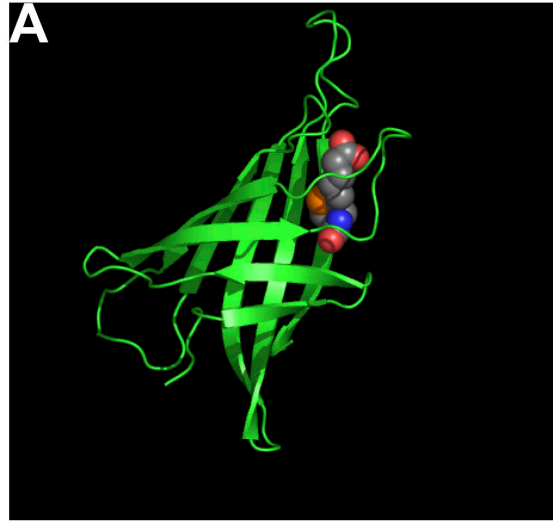


Figure 1.4 Structural model of Avidin monomer bound to biotin.

Looking at a single molecule of Avidin (green) bound to biotin, the small and recessed binding face is readily apparent (PDB ID 2AVI)(Livnah et al. 1993).

1.6. BIOACCUMULATION OF PARAMAGNETIC METALS VIA MEMBRANE TRANSPORTERS

The previous section dealt with a method of genetically targeting an exogenous contrast agent introduced by injection (**Chapter 1.6**). The major strength of that strategy being the versatility of agents one can use for targeting. However, a major and probably insurmountable limitation is that agents are limited to the vascular system and immediate areas outside of pathologically leaking vessels.

Ideally, one would avoid having to inject an agent at all, or at least be able to use a small agent that can penetrate membranes. In this case,

contrast would be a much closer analog to gene expression alone. The paragon example of this in fluorescence imaging would be GFP. This protein produces its own visible probe purely by the expression of the GFP gene sequence allowing for a linear relationship between expression and signal. The para and superparamagnetic contrast agents discussed are elemental metals and therefore not expressible by genetics, however a host of gene products can accumulate and sequester such metals. These proteins, either alone or in concert, could potentially generate contrast as a secondary effect of their function.

Candidate genes for expressible contrast:

As explained previously, para and super paramagnetic metals used as contrast agents can be integrated into functional molecules. Naturally achieving these same effects using integrated biology, but where to begin? Gd is a highly effective contrast agent, but its rarity and toxicity precludes the element from biological processes. Conversely, the paramagnetic agents Fe and Mn are present physiologically and essential to a wide range of biological processes. Because they are biologically active, Fe and Mn have carefully regulated uptake and excretion at the cellular and systemic level. Metabolic metal regulation is a genetically regulated process with many identified and characterized proteins. So while we cannot generate paramagnetic contrast agents directly, we can take advantage of existing processes to localize these

metals through synthetic gene expression. To accomplish this, we must first understand the uptake mechanisms of Fe and Mn. Most known mechanisms of uptake have been elucidated for Fe with less interest in Mn, but there is functional overlap between the two metals, so many proteins thought specific to Fe are also valid Mn transporters.

Biology of Intercellular Metal Transport:

Both Mn and Fe are essential cofactors in many biological processes, yet both can also be toxic even at sub-millimolar concentrations (J. A. Roth & M. D. Garrick 2003). Consequently, all organisms have established complex and redundant systems for uptake, storage, and excretion of both metals. The two elements have some uncanny similarities. Their atoms are similar in atomic size and orbital geometries. Both metals have multiple valence states with their +2 and +3 states being the most biologically active. It is no surprise then, their uptake and storage pathways heavily overlap, often pathologically. For instance, Mn binds to iron responsive elements (IREs) in DNA and RNA (J. A. Roth & M. D. Garrick 2003). Because of this, the regulatory fates of Fe and Mn are intrinsically tied to each other. Lack of Fe can increase Mn uptake to the point of toxicity, just as high levels of Mn will cause storage or excretion of Fe to deficient levels (J. A. Roth & M. D. Garrick 2003).

Fe and Mn pass through several barriers between the external environment and the brain. The canonical method of absorption of either

metal begins with uptake across epithelial tissue of the small intestine and passage through the liver before being transported to the brain and other organs by the circulatory system (Wei Zheng et al. 2003). From here they must be actively transported across either the BBB or the Blood Cerebrospinal Fluid Barrier (BCB). The major proteins involved in transport were first identified expressed at high levels at these points of systemic control and later found at much lower levels in almost every cell type.

Transferrin and Transferrin Receptor:

The fundamental and well studied Fe transport protein, Tf is an 80kDa secreted protein found in serum (Moos & E. H. Morgan 2000). Each molecule binds two atoms of insoluble Fe^{+3} . Tf also has some affinity for Mn^{+3} . The majority of Tf is secreted from the liver, however some Tf is also expressed in the choroid plexus and oligodendrocytes in the brain. Serum Tf transports Fe across the luminal membrane of the capillary endothelium by receptor mediated endocytosis.

Receptor mediated endocytosis of Tf is the most prevalent and important transport mechanism for physiological delivery of iron to the brain (Moos & E. H. Morgan 2000). Tf Receptor (TfR) is a 180kDa integral membrane protein. As previously discussed, it has a high affinity for Tf (Kd 2-7nM) (Aisen 2004). TfR is displayed on the luminal membrane of the capillary endothelial cells where it binds with Fe bound Tf in serum (J. A. Roth & M. D. Garrick 2003).

Upon binding, the receptor is accumulated into Clathrin coated pits and endocytosed. Once endocytosed the Fe-Tf-TfR complexes are drawn into a recycling endosome where low pH disassociates the whole Tf/TfR complex and the enzyme ferrireductase converts the Fe⁺³ atoms to a soluble +2 state (Irie & Tavassoli 1987). Soluble Fe⁺² is then transported out of the endosome by the transport protein DMT1 (Moos & E. H. Morgan 2000).

Ferroportin Fpn1:

The primary function of ferroportin is to transport Fe out of cells. This would imply that Fpn1 is meant to remove excess Fe from the cell, but this is only partially the case (L. J. Wu et al. 2004). In fact, Fpn1 can transport other metals such as Zn, Cd, and Co, making it critical in the response to metal toxicity (Troadek et al. 2010). Furthermore, Fpn1 plays a more balance role in Fe homeostasis. Animals with low levels of Fpn1 actually suffer from Fe deficiency compensated for by an upregulation of Tf and TfR while Fpn1 null mutant mice are embryo lethal due to lack of Fe (L. J. Wu et al. 2004). The reason for this offers one further insight from Tf/TfR as a model targeting system. Tf is too large of a molecule to pass beyond the vasculature and Fe is not allowed to freely diffuse. So while Fe is drawn from the vasculature via TfR it cannot pass beyond the vascular endothelial tissue without Fpn1 activity. In null mutant animals Fe cannot pass through the placenta causing developmental defects in the neural tube similar to sever folic acid deficiency

(J. Mao et al. 2010). The dual and critical role of Fpn1 as a mechanism of metal excretion and dissemination makes for a fascinating protein to study, and presents a cautionary lesson for bioengineering.

MagA:

Certain soil bacteria exhibit magnetotactic behavior lining up with the earth's magnetic field (Yoshino et al. 2010). Electron microscopy studies revealed the presence of Fe nanoparticles in the form of magnetite. To take up sufficient Fe, reduce it to its metallic form and nucleate a particle requires a suite of metalloproteins that have been identified and at least partially characterized. The Fe specific transport protein of this module is MagA (Nakamura et al. 1995).

Limited work with MagA suggests that expression in eukaryotic cells does in fact transport Fe (Goldhawk et al. 2009). Bioinformatics analysis indicates MagA to be homologous with other known prokaryotic transporters of Fe though there are no other domains in the protein that would suggest the ability to reduce Fe or form any sort of particle on its own (Nakamura et al. 1995). Formation of the magnetic particles in bacteria is a fundamentally different process involving the bacterial membrane. Despite the disparity between eukaryotic and bacterial Fe biology, there is some suggestion that endogenous mechanisms, probably ferritin, are sufficient to increase the number of detectable Fe nanoparticles (Goldhawk et al. 2009).

DMT1 and SLCA2 family transporters:

Thus far only proteins specific to Fe transport have been discussed. Divalent Metal Transporter 1 (DMT1) is also a critical part of Fe transport but is also necessary for the transport of a wide range of metals. DMT1 has been shown to pump at least 8 different divalent metal cations including Mn and Fe (Picard et al. 2000). In addition to its versatile metal affinity, DMT1 plays multiple roles in metal transport. In addition to metal homeostasis, DMT1, also known as natural resistance associated macrophage protein (Nramp2), is also highly expressed in immune cells where it forcibly removes essential metals from foreign cells that have been phagocytosed. To accommodate this diverse function, DMT1 mRNA has 2 common alternate splicings with 5 others identified (Lam-Yuk-Tseung & Philippe Gros 2006). DMT1 type 1 exists primarily on the plasma membrane and appears to be meant for generic transport of free metal ions. The type 2 isoform is also present at the plasma membrane, but appears mostly in clathrin coated pits and in early endosomes. There is no fundamental difference between these two isoforms in terms of their metal binding or transport ability (M. D. Garrick et al. 2006). The minimal biochemical differences between isoforms suggest the primary differences are in regulatory regions. For example, the extended tail in the type 2 isoform allows association with TfR and the trafficking proteins that direct TfR endocytosis.

Numerous forms of SLCA2 type transporters have been identified in every organism identified. One form identified in *E. coli*, MnTH is theoretically descended from eukaryotic DMT1 and picked up through horizontal gene transfer (Richer et al. 2003). It is very similar to eukaryotic DMT1 except in that it is missing the entire C-terminal region and the 12th transmembrane region found in all other SLCA2 family members, further evidence that the variable C terminal region is purely regulatory.

Rationale for a focus on DMT1:

DMT1's demonstrated highly efficient transport of metals suggested the real potential that engineered DMT expression could serve as a genetically expressible accumulator of paramagnetic agents. Given the very tight regulation of Fe and the mixed success with Fe based reporter proteins, DMT1's Mn transport capabilities made for a far more attractive direction of research. Mn has its own transport mechanism which are not entirely understood, but this has not prevented its use as a contrast agent in Mn enhanced MRI (MEMRI). It is worth examining the current practice of MEMRI more closely to understand how it might be employed in conjunctions with DMT1.

1.7. SEQUESTERING METALS VIA METALLOPROTEINS

Much of the work herein focuses on ligand based methods for targeted agents (Biotag) and biological methods of taking up non-targeted contrast

agents (DMT1). In both systems, contrast is not retained indefinitely. In the case of DMT1 Mn retention is highly variable between cell types. One strategy that might solve these issues is a biological means of retaining a non-targeted agent. This has actually been the dominant methodology in the field and worth further exploration. Ferritin represents the paragon of these efforts and thus serves as a template for innovation.

Ferritin:

Once inside the cell Fe and Mn must, either be used, excreted, or stored. The dominant storage method for both metals is the protein Ferritin. Ferritin is a 24 subunit heteromer of varying amounts of an H and L subtype. (Chasteen & P. M. Harrison 1999) The Ferritin H subtype includes a ferroxidase center that converts Fe from a +2 to a +3 state. The Ferritin L subtype is very similar, only in lieu of an oxidation center it has a nucleation center which helps form the 5-nm particle of insoluble FePO₃ that makes up the core of the complex. The core particle of ferritin is not pure Fe. A typical Ferritin core could consist of from 20% - 70% PO₃⁻³ and Mn that is also oxidized by Ferritin H. The composition of a single ferritin particle relies on the ratios of H and L subtype. More nucleation centers result in a denser, purer core of metal.

The Ferritin family consists of more than just the eukaryotic H and L subtypes. A third subtype of Ferritin exists in mitochondrion. (Corsi et al.

2002) Ferritin M is similar to the H subtype, but does not need any Ferritin L to form the core. Rather than use expression ratios between two subtypes for particle optimization prokaryotic ferritin have evolved species specific optimizations for their environment. This includes a range of particle sizes from 3-15 nm, and one type of ferritin in thermophilic bacteria *F. fulgidus* that has large solvent exposed pores in its ferritin complex. (E. Johnson et al. 2005)

Ferritin's ability to form this insoluble nanoparticle of Fe has made it the focus of most work in expressible MRI contrast (Cohen et al., 2007; Genove et al., 2005; Deans et al., 2006; Ziv et al., 2010). High levels of Fe are needed to get significant particle formation, which are supplemented, in the animals diet even when coexpressing TfR to improve Fe uptake, and SNR continues to be a major problem especially in transgenics. One major issue in using ferritin is striking the proper balance of H vs. L chain ferritin. Protein engineering efforts have including coexpressing the two ferritin types and linking both proteins together (Iordanova et al. 2010a). It remains undetermined what the optimal ration of H to L would be for maximal T₂ enhancement.

Intracellular Mn transporter, ATP2C:

The specific biology of intracellular Mn is not fully understood, however genetic and biochemical data has identified an Mn specific transporter

expressed only in the Golgi, suggesting a role in Mn sequestration. ATP2C2 is a P type molecular pump originally identified in yeast where it is also expressed in the Golgi with a similar pump ATP2C1(Xiang et al. 2005). Originally these pumps were believed to be functionally similar to the SERCA pumps, which gather Ca into the Endoplasmic and Sarcoplasmic reticulum for signaling. Genetic knock outs have since identified ATP2C1 to be a general pump that favors Ca, and ATP2C2 uniquely specific to Mn.

Why specifically the Golgi would store Mn is poorly understood, however Mn is a necessary cofactor in many glycosylation enzymes and some Matrix Metallo Proteases (MMPs). Given the generally poor specificity most proteins exhibit to Mn having an organelle within the secretory pathway with a high concentration of Mn would allow binding as these proteins fold, ultimately sequestering the Mn from solvent.

More intriguingly, knocking out the ATP2C2 pump in yeast makes desensitizes the cell to the drug rapamycin (Devasahayam et al. 2007). Desensitization is due to the lack of Mn in the Golgi as sensitivity can be rescued by using other Mn pumps or reducing the Ca specificity of ATP2C1 by selective mutation in the knockout strain. ATP2C2's effect on biology is not exclusive to yeast as ATP2C2 knockdowns in cultured hippocampal neurons reduce the dendritic arbors of these cells (Sepúlveda et al. 2009). Mn retention in the Golgi appears to be a biologically important, but poorly

understood process due to a lack of molecular tools available to study its localization in cells.

MntR:

Selective binding with Mn over Ca or Fe is in fact a difficult problem. Mn's toxicity lies in its duplicitous nature. Its capacity to travel through Ca channels has been previously mentioned, as has its ability to bind to Iron response elements (IREs) in RNA and DNA (J. A. Roth & M. D. Garrick 2003). The two edge sword quality of Mn is apparent in bacteria as well, wherein optimization is essential to survival. In order to maintain Mn at a low level that does not interfere with either Ca or Fe metabolism, free Mn must be regulated. Mn can be sequestered into ferritin particles, another overlap between Mn and Fe, but the most effective method of regulation is to control the uptake of Mn (Patzner & Hantke 2001). Determining the optimal concentration of Mn in bacteria is the role of MntR (Glasfeld et al. 2003).

At very low levels of Mn within the bacterium there is active uptake. MnTH, an SLC11A2 protein, is expressed to actively take up trace levels of Mn. In E.coli, this protein is actually a descendent of mammalian DMT1 picked up by horizontal gene transfer (Richer et al. 2003). At a functional concentration of Mn, the ion binds to a sensing protein MntR. The protein gains a more rigid structure and becomes capable of binding DNA, blocking expression of the SLC11A2 protein and allowing for expression of a pump

that sends Mn out of the cell (Golynskiy et al., 2005; Patzer and Hantke, 2001; Waters et al., 2011).

The Mn sensing transcription factor MntR then is the seemingly ideal candidate for an expressible contrast agent. Structurally MntR has all the hallmarks of a successful agent, for example its relatively high specificity for Mn of $K_d \sim 200 \text{ nM}$ is well within the measured levels of Mn in serum ($\sim 10 \mu\text{M}$) (Kliegman et al. 2006). Furthermore its Mn binding domain is distinct from other Mn binding proteins such as arginase, prolinase or super oxide dismutase (SOD) in that the Mn is well exposed to solvent. Because of this, MntR has direct interactions with solvent water with a clear potential for exchange, critical for the T_1 effect. Within the structure of MntR 2 Mn ions are bound in a binuclear manner to the protein. Only proteins with this binuclear binding motif have exposed Mn suggesting that this structure is important for interacting with Mn in a reversible, but specific way (Ilies et al. 2010).

1.8. OVERVIEW

This thesis took multiple approaches to developing *in vivo* reporters. MRI was the imaging modality of primary focus, but alternate imaging modalities were explored where appropriate. No protein examined here was directly detectable in any imaging modality, instead first order properties such as binding specificity or specific transport of Mn was exploited to provide an effect. In all cases, understanding both protein function and second order effects of biology were equally important for proper function.

Biotag Overview:

Drawing from existing methods in targeted imaging, we designed an optimal tagging system to implement in a transgenic mouse. The method uses the well studied property of the protein avidin to bind its substrate biotin with an almost irreversible affinity (O. H. Laitinen et al. 2007). In this way, biotin is displayed on the surface of cells as a tag while avidin is conjugated to a chemical agent that functions as a molecular probe. This strategy offers a distinct advantage in that there are a wide range of molecular probes that use paramagnetic metals or magnetic nanoparticles, which are compatible with existing MRI protocols. Furthermore, this strategy is compatible with molecular probes for any type of imaging, making the system “multimodal.”

DMT1 Overview:

The paramagnetic ion Mn^{+2} , is endogenous to living organisms. Known and characterized proteins actively bind Mn and transport it in and out of cells. One such protein is the Divalent Metal Transporter, DMT1. Even as proteins like DMT1 are being characterized an entire field of MRI has developed around using Mn to enhance contrast in biologically relevant ways based on endogenous mechanism of Mn uptake. It follows that known mechanisms of DMT1 uptake can be reverse engineered to take up paramagnetic Mn in a controlled manner, thus controlling contrast genetically. Mn uptake and retention are biologically regulated process, resulting in second order effects that can have an effect on contrast.

MntR Overview:

Just as there are mechanisms of uptake there are also mechanisms of Mn excretion. Tissues can release Mn within the scope of an imaging protocol. To address this, an Mn chelating protein, MntR, was employed to actively bind Mn, once taken up by the cell. A conceptual feature and potential advantage to this method is that the relationship between Mn binding and relaxivity is a first order effect, and potentially an area for later technological development. The major challenge proved to be that, despite Mn binding being a simple first order effect, bioavailability of Mn remains poorly understood. In addition to being subject to second order uptake and excretion

mechanisms, there are less understood intracellular Mn sequestration systems that must be addressed for *in vivo* functionality.

Visualizing Biology with Biological Contrast:

The resulting data from the development of these reporter proteins and the methods to properly implement them *in vivo* provide data is a synthesis of successive layers of technologies. First order effects of proteins, create a spatially distinct variation in magnetic resonance, which is in turn mapped into an MR image. The potential meaning of this abstract data is completely dependent on the biology in question. A genetic promoter can be constitutively active in a given cell or tissue type, or can switch on and off given specific stimuli. The nature of genetic regulation is so rich and complex that despite decades of research there are an immeasurable number of unknown mechanisms to be elucidated. Reporter assays remain a canon of these efforts, making the tools presented here a necessary and welcome addition to scientific research.

2. A NOVEL GENETIC APPROACH FOR *IN VIVO* VASCULAR IMAGING IN MICE

This chapter was published as:

A Novel Genetic Approach for *In Vivo* Vascular Imaging In Mice

Benjamin B. Bartelle^{1,2}, Cesar A. Berrios-Otero^{1,3}, Joe J. Rodriguez¹
Anne E. Friedland¹, Orlando Aristizábal¹ and Daniel H. Turnbull^{1,2,3,4,5,*}

Circulation Research. 2012; 110: 938-947 Published online before print
February 28, 2012, doi: 10.1161/CIRCRESAHA.111.254375

¹Kimmel Center for Biology & Medicine at the Skirball Institute of Biomolecular
Medicine, ²Structural Biology and ³Developmental Genetics Graduate
Programs, and Departments of ⁴Radiology and ⁵Pathology
New York University School of Medicine, New York NY

Attribution of Data:

B.B.B. C.A.B. and D.H.T. designed the experiments and wrote the
manuscript.

BB: Conceptualized the project, designed and generated all constructs and
mice, collected and analyzed data for all figures

C.A.B. Tested the constructs in cells, collected and analyzed embryo data,

J.J.R Assisted in data collection for embryo analysis

A.E.F. Assisted in screening transgenic mice and data collection for adult
animal studies.

OA Consulted on data analysis for UBM studies

2.1. ABSTRACT

Rationale: The formation and maintenance of a functional vasculature is essential for normal embryonic development, and genetic changes affecting vasculature underlie pathogenesis in many human diseases. *In vivo* imaging in mouse models is required to understand the full complexity of mammalian vascular formation, which is a dynamic and three-dimensional process. Optical microscopy of genetically expressed fluorescent reporter proteins offers high resolution, but limited depth of penetration *in vivo*. Conversely there are a plethora of molecular probes for alternative *in vivo* vascular imaging modalities, but few options for genetic control of contrast enhancement.

Objective: To develop a reporter system for multimodal imaging of genetic processes involved in mammalian vascular biology.

Methods and Results: To approach this problem, we developed an optimal tagging system based on Biotag-BirA technology. In the resulting Biotag reporter system, co-expression of two interacting proteins results in biotin labeling of cell membranes, thus enabling multi-modal imaging with avidinated probes. To assess this approach for *in vivo* imaging, we generated transgenic mice that express the Biotag-BirA transgene from a minimal *Tie2* promoter. A variety of imaging methods were employed to show the utility of this approach for quantitative analysis in embryonic and adult models of vascular

development, using intravascular injection of avidinated probes for near infrared (NIR), ultrasound, and magnetic resonance imaging (MRI).

Conclusions: Our results demonstrate the versatility of the Biotag system for studies of vascular biology in genetically-engineered mice, providing a robust approach for multi-modal *in vivo* imaging of genetic processes in the vasculature.

Keywords: Biotag; BirA; magnetic resonance imaging, MRI; near infrared, NIR; ultrasound imaging

2.2. INTRODUCTION

A functional vasculature must be established for any biological organism to grow beyond a few hundred micrometers in diameter. Therefore it is not surprising that all vertebrate animals form a vascular system early in development, using well-conserved genetic pathways. *In vivo*, three-dimensional (3D) imaging methods are required to study the full temporal and spatial complexity of the developing mammalian vasculature. To this end, genetic approaches have been developed previously, by expressing enhanced green fluorescent protein (eGFP) and its variants from vascular cell-specific promoters. However, the fluorescent reporters themselves present problems for *in vivo* imaging in mice, since the limited penetration of optical microscopy restricts imaging to superficial tissues, explants or early

stage embryos maintained in culture over relatively short temporal windows (Fraser et al., 2005; Hilderbrand and Weissleder, 2010; Phoon, 2006).

Alternative *in vivo* imaging modalities provide 3D data with far greater penetration in mammalian tissues, albeit with lower spatial resolution than optical microscopy. For small animal vascular imaging, available methods include near infrared (NIR) (Hilderbrand & Ralph Weissleder 2010), ultrasound biomicroscopy (UBM) (Colin Kit Lun Phoon 2006), and magnetic resonance micro-imaging (micro-MRI) (Nieman et al., 2007; Turnbull and Mori, 2007). While these modalities vary in their vascular imaging properties, including penetration and spatial resolution, they share a common need for probes or contrast agents that are targeted to molecules expressed on the luminal surface of vascular endothelial cells. Antibodies and peptides have been conjugated to intravascular contrast agents to target them to membrane proteins such as $\alpha_v\beta_3$ -integrin (Rüegg and Alghisi, 2010; Winter et al., 2003; Ellegala et al., 2003) and vascular endothelial growth factor receptor (VEGFR) (Ferrara and Kerbel, 2005; Willmann et al., 2008; De León-Rodríguez et al., 2010). Since the endothelial cell surface is accessible *via* the circulation, contrast agents can be delivered to their target cells by intravascular injection.

There are limitations endemic to targeted contrast agents, primarily the relatively low binding affinities to their cognate receptors. As a result, *in vivo* binding can be inefficient and take a substantial amount of time to bind at detectable levels. Moreover, developing agents targeted to a specific protein is a complex and time consuming process, and each agent can take years to properly optimize, especially for low affinity targets. Finally, targeted imaging is necessarily limited to extracellular proteins, and many critical molecules cannot be targeted simply because they are intracellular.

To address the limitations of current reporter gene and targeted imaging technologies, we developed a synthetic, “Biotag” reporter system that displays a cluster of biotins on cell membranes. Avidin-biotin affinity is several orders of magnitude higher than the strongest antibody-receptor binding, and is essentially irreversible under physiological conditions (O. H. Laitinen et al. 2007). Moreover, a host of avidinated contrast agents are available for many imaging modalities (Diamandis & Christopoulos 1991). Compared to previous biotinylation systems (Beckett et al., 1999; Tannous et al., 2006), our transgene is completely self-contained and can be used with any endothelial promoter as a vascular reporter system. To test this approach, we generated transgenic *Ts-Biotag* mice, using a minimal promoter for *Tie2* (T-short (Minami et al. 2003), denoted Ts). *Tie2* was chosen for its multiple dynamic roles in vascular stability and remodeling (Fukuhara et al. 2009), and the

availability of the regulatory sequences required to generate *Ts* transgenic mice (Motoike et al., 2000; Minami et al., 2003). *In vivo* imaging of *Tie2* expression was demonstrated in *Ts-Biotag* mice, in both embryonic and adult models of vascular development, demonstrating the potential of this general method for vascular imaging of genetic processes in mice.

2.3. RESULTSThe Biotag-BirA expression system effectively biotinylates cell membranes:

Our membrane biotinylation approach is based on the co-expression of two interacting proteins (**Figure 2.1**). BirA, a biotin ligase, was maintained in the endoplasmic reticulum (ER) by including an N-terminal signal sequence derived from the ER chaperone BiP, as well as a C-terminal KDEL ER-localization sequence. The resulting ER-targeted *BirA* (*BirA^{ER}*) was co-expressed, using an internal ribosome entry site (IRES), with a chimeric protein, consisting of the transmembrane domain of the PDGF receptor (PDGFR-TM) fused to multiple (n) biotags: nxbiotag·PDGFR-TM, referred to here as Biotag. The *nxBiotag* DNA was further modified, localizing it to the ER

by including an N-terminal signal sequence similar to *BirA^{ER}*. Our goal was to express and maintain both Biotag and BirA in the secretory pathway, where they could interact and generate a biotinylated membrane protein for targeting with avidinated probes.

To establish that the Biotag reporter system resulted in correct subcellular expression of the two component proteins, HEK-293 cells were transfected with the construct *CMV-Biotag-IRES-BirA^{ER}*, and the transfected cells were subsequently analyzed with immunocytochemistry. Costaining for the BirA-specific HA epitope tag and the endoplasmic reticulum (ER) marker Calnexin showed that BirA was correctly targeted to the ER (**Figure 2.2A**). The Myc tag integrated in the Biotag protein colocalized with Phalloidin staining for F-actin, which largely underlies the membrane (Gervais et al. 2008) (**Figure 2.2B**). Finally, costaining for both the HA and Myc tags showed partially overlapping expression patterns, confirming that BirA and Biotag colocalize in the ER as the Biotag protein is being trafficked to the cell membrane (**Figure 2.2C**).

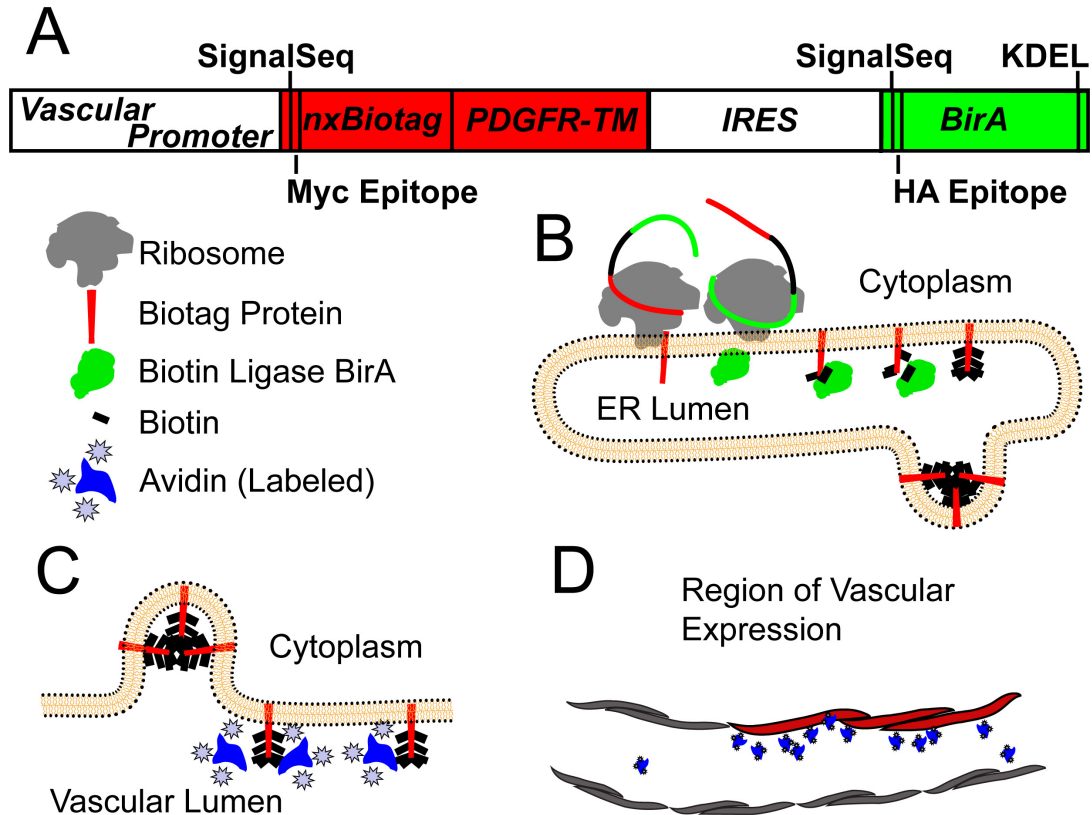


Figure 2.1 Schematic of the Biotag reporter system

The Biotag transgene construct consists of multiple (*nx*) biotags fused to a signal sequence (SS) and the Myc-tagged PDGF receptor *trans*-membrane domain (PDGFR-TM), followed by an internal ribosome entry site (IRES) sequence to co-express the HA-tagged BirA enzyme modified with SS and KDEL sequences (**A**). Expression of this bicistronic construct can be driven by any desired vascular endothelial cell promoter. Upon translation the ribosome recognizes the N-terminal SS to insert each protein into the lumen of the endoplasmic reticulum (ER). As the proteins move through the secretory pathway, the BirA enzyme ligates free biotins onto the Biotag protein (**B**). The resulting biotinylated Biotag protein continues through the secretory pathway to the cell surface while BirA is retained in the ER by the KDEL sequence. Once on the cell surface, the ligated biotins on the Biotag protein are available to bind avidinated probes (**C**). The probes selectively enhance vasculature endothelial cells that express the gene whose promoter was incorporated into the transgene construct (**D**).

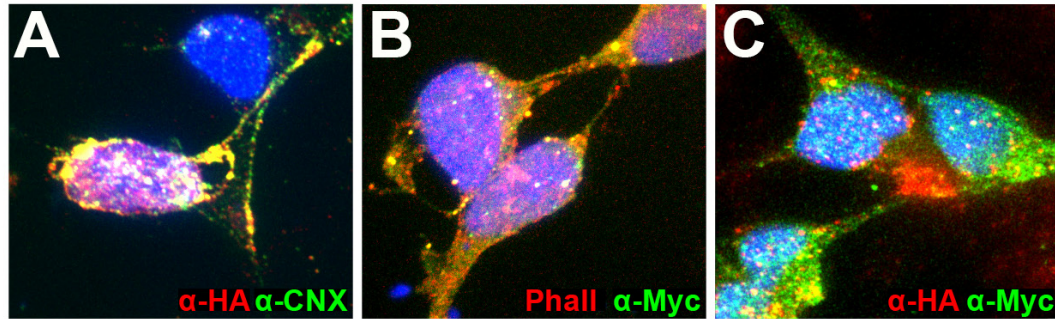


Figure 2.2 Co-localization of Biotag and BirA^{ER} in expressing cells

After co-transfection of HEK-293 cells with Biotag and BirA^{ER}, HA-tagged BirA (red) co-localized with the ER marker Calnexin (CNX, green) (**A**), while Myc-tagged Biotag (green) co-localized with Phalloidin (Phall, red) (**B**), which stains F-actin filaments and highlights the cell membranes. Costaining for both HA (red) and Myc (green) showed partial overlap of the BirA and Biotag proteins (**C**). Blue staining in panels (**A-C**) is DAPI nuclear stain.

To determine the functionality of the membrane biotinylation generated by the Biotag expression system, live cell staining with avidin-fluorescent probes was performed on HEK-293 cells transfected with *CMV-nxBiotag-IRES-BirA^{ER}*, where n ranged from 1 to 12. Compared to non-transfected cells, there was an obvious increase in avidin-fluorescein isothiocyanate (Av-FITC) membrane staining in transfected cells. Moreover, the membrane staining increased with the number of biotags in the expression construct (**Figures 2.3A-C**). The differences in cell membrane biotinylation were quantified with a digital NIR scanner after live cell staining in multiwell plates with the NIR probe, streptavidin-alexa680 (SAv-680). Non-transfected cells and cells transfected with either *1xBiotag* or *BirA^{ER}* alone were included as negative

controls, while HEK-293 cells transfected with a previously described biotin acceptor peptide (*BAP*) (Tannous et al. 2006) served as a positive control (**Figure 2.3D**). Limitations of *BAP* include its large size (387 bases), making it difficult to incorporate into a transgene or to amplify membrane biotin *via* insertion of multiple biotinylation sites, as well as its dependence on an unknown biotinylation enzyme that may not be present in all cells of interest. Statistical analysis showed significant increases in cell staining, comparing wells of cells transfected with *nxBiotag-IRES-BirA^{ER}* and negative controls (**Figure 2.3D**; * $p < 0.005$; $N \geq 8$ in each group). The *1xBiotag-IRES-BirA^{ER}* and *BAP* transfected cells, each with one biotin per molecule of protein, yielded approximately a 2.5-fold signal increase over background. Increasing amounts of biotin per protein molecule with the 6x and 12x versions of the construct gave higher signal enhancement, with *12xBiotag-IRES-BirA^{ER}* transfected cells showing a further 3-fold gain over *BAP* and *1xBiotag-IRES-BirA^{ER}* (**Figure 2.3D**; ** $p < 0.05$; $N \geq 8$ in each group). We conclude that cell membranes can be effectively biotinylated by expression of *nxBiotag-IRES-BirA^{ER}*, and that the level of functional biotin is proportional to the number of biotags included in the expression vector.

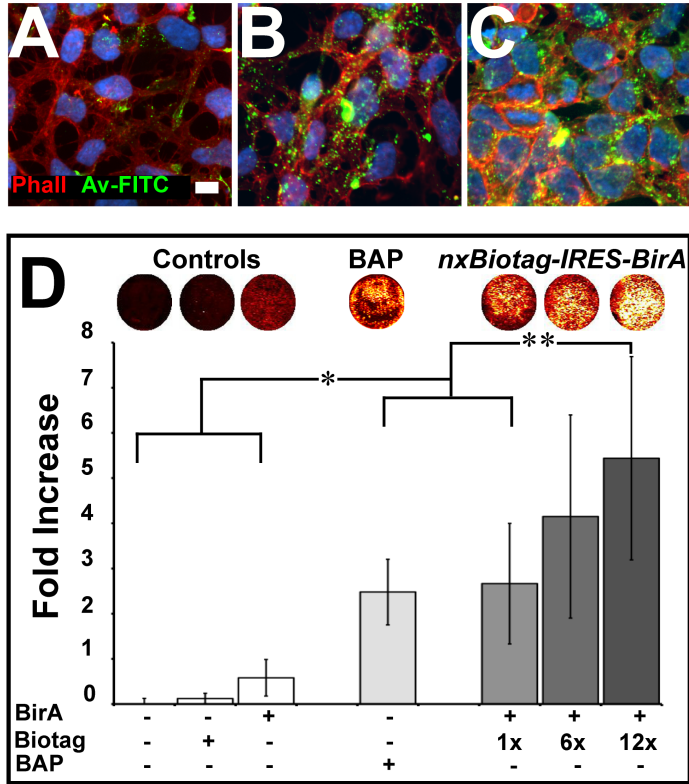


Figure 2.3 Co-expression of Biotag and BirA^{ER} results in membrane biotinylation.

Compared to control cells (A) or cells expressing 1xBiotag (B), cells expressing 12xBiotag (C) showed noticeably more membrane fluorescence after live cell staining with Av-FITC (green). Blue staining in panels (A-C) is DAPI nuclear stain. Differences with increasing numbers of biotags were quantified with NIR imaging after live cell staining with SAv-680 (N≥8 slides per group) (D). Cells expressing both BirA and nxBiotag (right data bars) gave significant increased staining compared to control cells (*left data bars, see text for statistical analysis): nontransfected (BirA-/Biotag-); transfected with 1xBiotag alone (BirA-/Biotag+); or transfected with BirA alone (BirA+/Biotag-). In cells transfected with 1xBiotag-IRES-BirA^{ER}, there was a significant increase in SAv-680 staining, comparable with labeling of BAP (BAP+). An increase from 1x-, to 6x-, to 12xBiotag resulted in significant increase in labeling. (**right data bars, see text for statistical analysis). Representative NIR images from wells of control cells and cells transfected with Biotag, BirA, BAP and nxBiotag-IRES-BirA^{ER} (n=1,6,12) are shown above each data bar (D). (N ≥ 8 wells of cells per measurement).

***Ts-Biotag* mice display biotin on embryonic vascular endothelial cells:**

To investigate the potential of the Biotag reporter system for *in vivo* vascular labeling, we generated transgenic mouse lines, expressing *12xBiotag-IRES-BirA^{ER}* from the *Ts* promoter (Minami et al. 2003) (**Figure 2.4**). The resulting *Ts-Biotag* mice showed no noticeable defects in viability, fertility, or development, compared to wildtype (WT) littermates (data not shown). All the results in this paper were generated from the two highest-expressing lines of *Ts-Biotag* mice.

To assess any possible deleterious effects of transgene expression on vascular development, we analyzed PECAM1 and Tie2 immunohistochemistry (IHC) in brain sections from E11.5-13.5 WT and *Ts-Biotag* embryos (**Figure 2.5A,B**). Neurovascular density, determined by PECAM1 staining, showed no significant differences between WT and *Ts-Biotag* embryos at any stage (**Figure 2.5A**). Comparing expression of endogenous Tie2 normalized against PECAM1 as a marker for vascular integrity there was also no significant difference between WT and *Ts-Biotag* embryos (**Figure 2.5B**). However there was a significant increase in Tie2 expression at E12.5 compared to both E11.5 ($p < 0.001$) and E13.5 ($p = 0.02$) ($N = 3$ for each stage and genotype). Similar results were also observed in histological sections of the hearts of the same WT and *Ts-Biotag* embryos

(data not shown). We conclude that vascular development was not compromised in the *Ts-Biotag* mouse embryos.

Transgene expression and functional tagging of vascular endothelial cells was evaluated using IHC for biotin. We observed an obvious increase in biotin staining in *Ts-Biotag* compared to WT embryos at both E11.5 and E12.5 (**Figure 2.5C**). These differences were quantified by measuring the ratio of biotin to PECAM1 signal in the region where they co-localized (**Figure 2.5D**). These results showed a significant increase in vascular biotin in *Ts-Biotag* vs WT embryos at both E11.5 ($p=0.03$) and E12.5 ($p=0.01$) (N=3 for each stage and genotype). We also observed a significant increase in the Biotin/PECAM1 ratio, comparing E12.5 to E11.5 *Ts-Biotag* embryos ($p<0.001$, N=3 for each stage and genotype), similar to the increase in Tie2/PECAM1 (**Figure 2.5B**). These results indicate that the *Ts-Biotag* transgene expresses biotin in a manner correlative to endogenous Tie2 expression in embryonic mice.

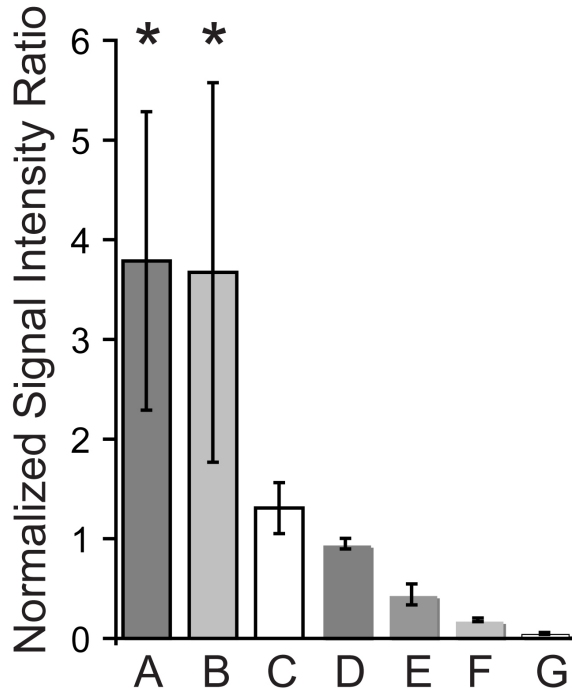


Figure 2.4 Western blot analyses of transgene levels in Ts-Biotag lines.

Protein samples were generated by PAGE-SDS electrophoresis on homogenized tissue from E11.5 embryos, generated from the 7 Ts-Biotag mouse lines (**A-G**) that produced transgenic offspring from the 8 founder mice (1 founder did not produce offspring). Protein was transferred to Immobilon-P membranes and costained with Rabbit anti-Myc (Abcam 9106) and Mouse anti- β -actin (Abcam 8226). Secondary antibody costaining was performed with Goat anti-Mouse-IRDye800 (Odyssey 926-32210) and Goat anti-Rabbit-IRDye-680 (Odyssey 926-32221). Blots were imaged on a NIR scanner (Odyssey Licor). Quantitative expression ratios were measured, using region-of-interest (ROI) measurements of signal intensity in each band divided by the signal intensity in the background (ROI/Background). Normalized signal intensity ratios were simply calculated as the normalized Myc intensity (red) divided by the normalized β -actin intensity (green), providing a quantitative measure of expression levels. Data were represented as mean \pm standard deviation (n=4-7 embryos per mouse line). The 3 highest expressing lines (**A-C**) were maintained by breeding. All the results in this paper were generated from the two highest expressing lines (**A,B**)*.

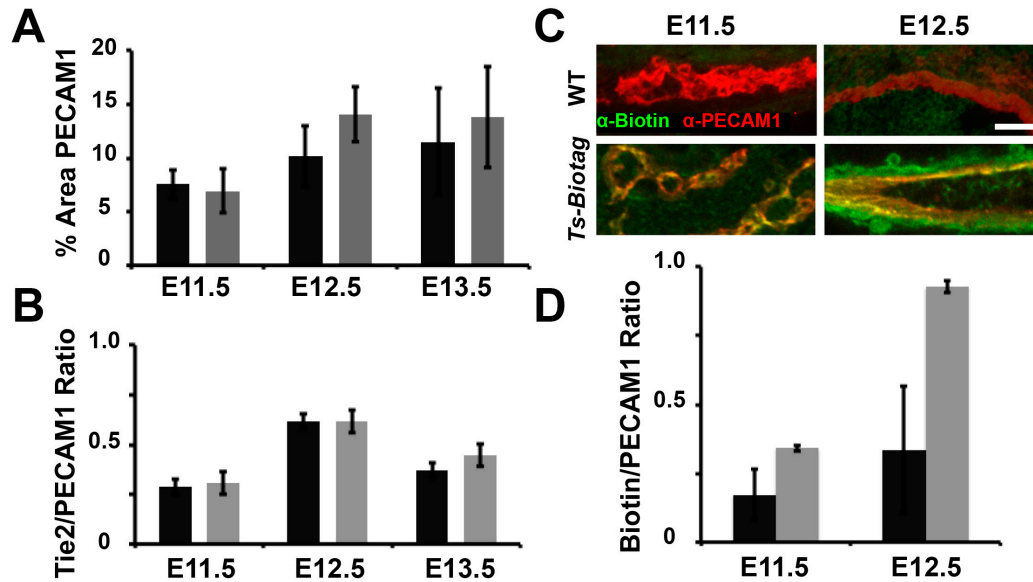


Figure 2.5 Ts-Biotag embryonic vasculature is biotinylated but otherwise similar to WT

Quantification of PECAM1 staining in the brain from E11.5-13.5 showed no significant differences in vascular density between WT (dark bars) and Ts-Biotag embryos (light bars) (**A**). Similarly, quantification of Tie2 normalized against PECAM1 staining showed no significant differences between WT and Ts-Biotag embryos (**B**). There was however a significant increase in Tie2 expression between E11.5 and E12.5. At both E11.5 and E12.5, biotin was readily detectable at much higher levels, specifically in PECAM1-expressing regions, due to selective expression of the Biotag transgene (**C**). Quantitative analysis of Biotin staining normalized against PECAM1 in E11.5-12.5 embryos showed a significant increase Biotin in Ts-Biotag compared to WT embryos, with an increase at E12.5 similar to Tie2 expression (**D**). (N = 3 embryos in each group; 3 sections per embryo). Scale bar = 25 μ m

Ts-Biotag embryonic vasculature can be targeted with avidinated

probes:

To explore the versatility of the Biotag system for embryonic vascular imaging, we used *in vivo* UBM-guided cardiac injection of avidinated probes into E11.5 WT and *Ts-Biotag* embryos. Injection of Av-FITC resulted in bright labeling in *Ts-Biotag* compared to WT embryos (**Figure 2.6A**). Light

scattering prevented resolution of individual blood vessels under the dissection microscope, but subsequent sectioning and costaining with PECAM1 showed vascular labeling clear vascular labeling in *Ts-Biotag* embryos, and minimal or no labeling in WT embryos (**Figure 2.7B,C**). As expected, there was also a good qualitative agreement between endogenous Tie2 expression and Av-FITC labeling in *Ts-Biotag* embryos (**Figure 2.7A,C**). To better resolve vasculature in 3D, embryos were injected with Av-DTPA-Gd for *ex vivo* micro-MRI (**Figure 2.6B-D**). Robust labeling was visible in a wide range of blood vessels in *Ts-Biotag* embryos, including the aorta, cardinal veins, cerebral and inter-somitic vessels (**Figure 2.6B**). Quantitative analysis was performed, using an automated segmentation method (threshold = background mean + 3 standard deviations, SD) to generate a 3D map of labeled voxels (**Figure 2.6C**). This analysis showed an obvious and statistically significant increase in labeled voxels in *Ts-Biotag* vs WT embryos (**Figure 2.6D**; * $p < 0.003$, N=5 for each genotype). These results demonstrate that the vascular endothelial cells of *Ts-Biotag* mouse embryos can be targeted *in vivo* using avidinated contrast agents.

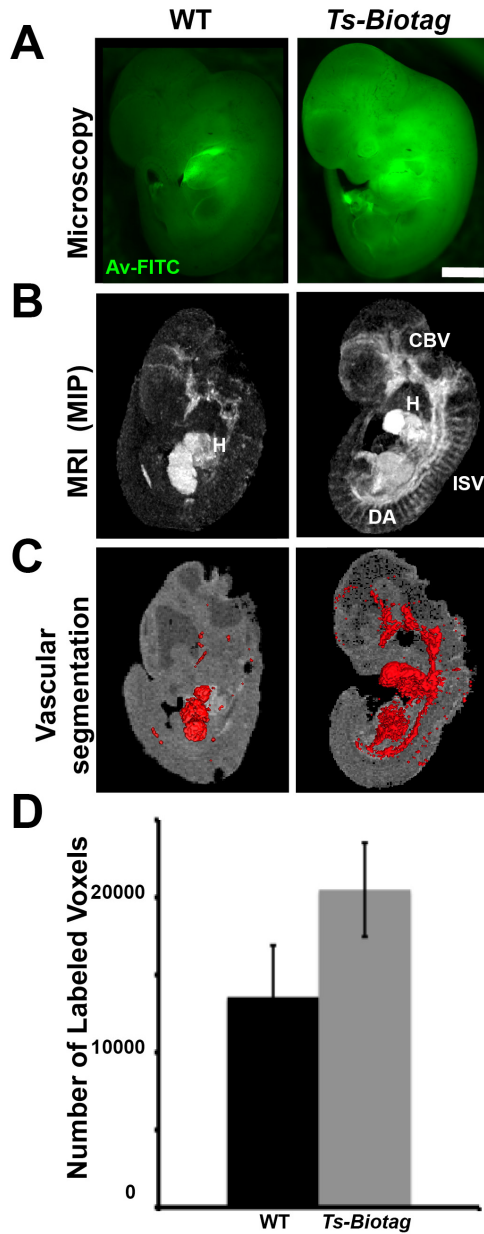


Figure 2.6 Targeted μ -MRI imaging of embryonic vasculature in Ts-Biotag mice.

Av-FITC injection selectively enhances vasculature in E11.5 Ts-Biotag embryos, but light scattering prevents resolution of individual blood vessels ($N \geq 8$ for each genotype) (**A**). Using Av-DTPA-Gd, labeling and ex vivo 3D micro-MRI of E11.5 WT ($N=5$) and Ts-Biotag ($N=5$) embryos, the vasculature was rendered volumetrically at $50\mu\text{m}$ isotropic resolution (**B**). In WT embryos, MRI contrast was largely confined to the injection site in the heart (H), while Ts-Biotag embryos showed extensive labeling, including in the cerebral blood vessels (CBV) and inter-somitic vessels (ISV). Vascular labeling was quantified over multiple whole embryos ($N=5$ for each genotype) by segmenting the voxels (red) above a threshold (mean background signal intensity + 3 SD) in both WT and Ts-Biotag embryos (**C**) (red voxels superimposed on central 2D section). Quantitative analysis showed a significant (*) increase in the number of labeled voxels in Ts-Biotag (grey bar) vs WT (black bar) embryos ($N=5$ for each genotype) (**D**) (see text for statistical analysis). Other labels: dorsal aorta, DA. Scale bar = 1 mm.

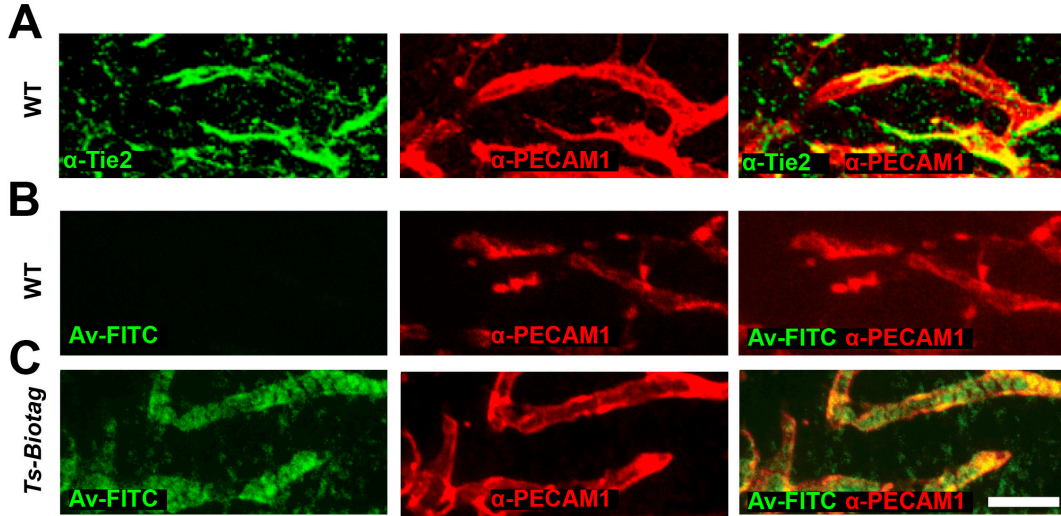


Figure 2.7 E11.5 Ts-Biotag embryonic Tie2 expressing vasculature is bound by avidinated probes.

IHC of E11.5 mice shows Tie2 expression in the neurovasculature. **(A)** The majority of Tie2 colocalizes with PECAM1 with some extravascular expression. In Av-FITC(green) injected WT and Ts-Biotag embryos co-stained with PECAM1 (red) **(B-C)** almost no Av-FITC signal is visible in WT **(B)**, In contrast, Ts-Biotag animals show highly specific co-localization of Av-FITC with the vascular endothelium in the Ts-Biotag embryos, similar to the Tie2 PECAM staining **(C)**. (N≥8 each group) Scale bar = 25 μm.

***In vivo* targeted ultrasound imaging of vasculature in *Ts-Biotag* embryos:**

UBM is an established real-time, *in utero* method for cardiovascular imaging in live mouse embryos^{3,22}. To determine the utility of the *Ts-Biotag* mice for transgene mediated UBM contrast-enhancement, we imaged E11.5 and E12.5 embryos before and after UBM-guided injection of Av-microbubbles. There was an obvious increased persistence of vascular enhancement in *Ts-Biotag* embryos compared to WT littermates over the time period up to 20 minutes following injection (**Figure 2.8**). This difference was most obvious on time-averaged images, calculated from cine (2D) UBM data acquired 20 minutes after injection of Av-microbubbles (**Figure 2.9, Figure 2.8**). This method of image processing was found to minimize the signal from circulating microbubbles compared to stationary (bound) microbubbles. Most embryos gave signal around the heart, probably as a result of microbubbles being trapped in the pericardium (**Figure 2.9A**). Time-averaged images of *Ts-Biotag* embryos (**Figure 2.9B**) showed enhancement in a much more extensive vascular network in the brain that included increased numbers of smaller cerebral blood vessels, compared to WT (**Figure 2.9A**). Similar *ex vivo* micro-MRI, quantitative analysis was performed on *in vivo* UBM images using an automated segmentation method (threshold = background mean + 5SD). These results showed an obvious and statistically significant increase

in labeled pixels in *Ts-Biotag* vs WT embryos (**Figure 2.9D**) at both E11.5 ($p < 0.001$, N = 7 WT, 7 *Ts-Biotag*) and E12.5 ($p < 0.01$, N = 7, 7). Furthermore, there was an increase in labeled pixels in E12.5 vs E11.5 *Ts-Biotag* embryos (**Figure 2.9D**), consistent with the increase in Tie2 and vascular biotin (**Figure 2.5**), though variability of labeling prevented significance.

To assess the potential of this method for longitudinal imaging studies, selected *Ts-Biotag* embryos were injected with Av-microbubbles and imaged at E11.5, and then injected again and reimaged at E12.5 (**Figure 2.9C**). Quantitative analysis of the longitudinal data showed an obvious and statistically significant increase in labeled pixels at E12.5 vs E11.5 (**Figure 2.9D**; $p = 0.02$, N = 3), and no difference in labeling comparing single time point and longitudinal data at E11.5 ($p = 0.26$) or E12.5 ($p = 0.35$). These results demonstrate the feasibility of the Biotag system for longitudinal UBM imaging of vasculature during mouse embryogenesis.

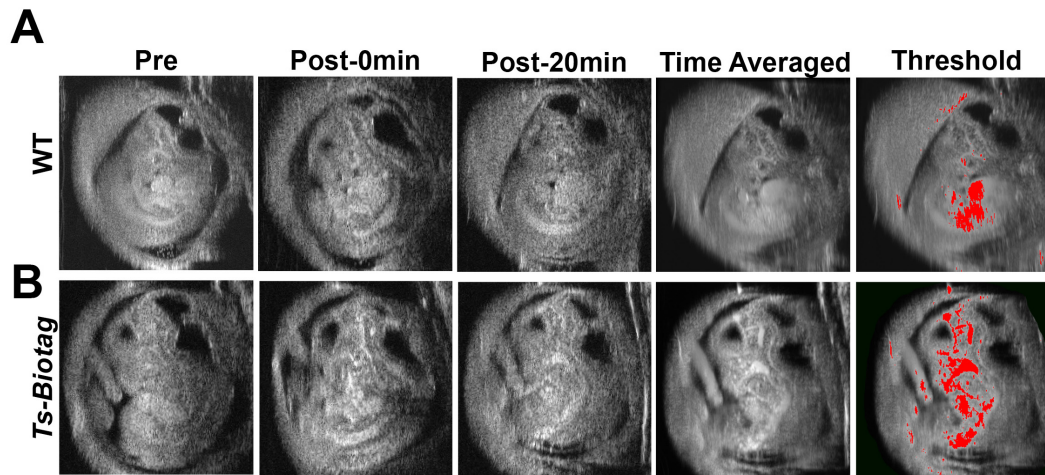


Figure 2.8 UBM imaging of vasculature in Ts-Biotag embryos

In vivo longitudinal UBM imaging of E11.5 WT (**A**) and Ts-Biotag (**B**) embryos, before (Pre), immediately after (Post-0min) and 20 minutes after (Post-20min) injection of Av-microbubbles, demonstrated a higher and prolonged level of vascular enhancement in transgenic embryos, this is especially apparent in time averaged images where signal from moving bubbles is reduced. Threshold analysis (red pixels, threshold = mean background signal + 5 standard deviations) was used to quantify vascular labeling (n=7 for each genotype).

Scale bar = 1 mm.

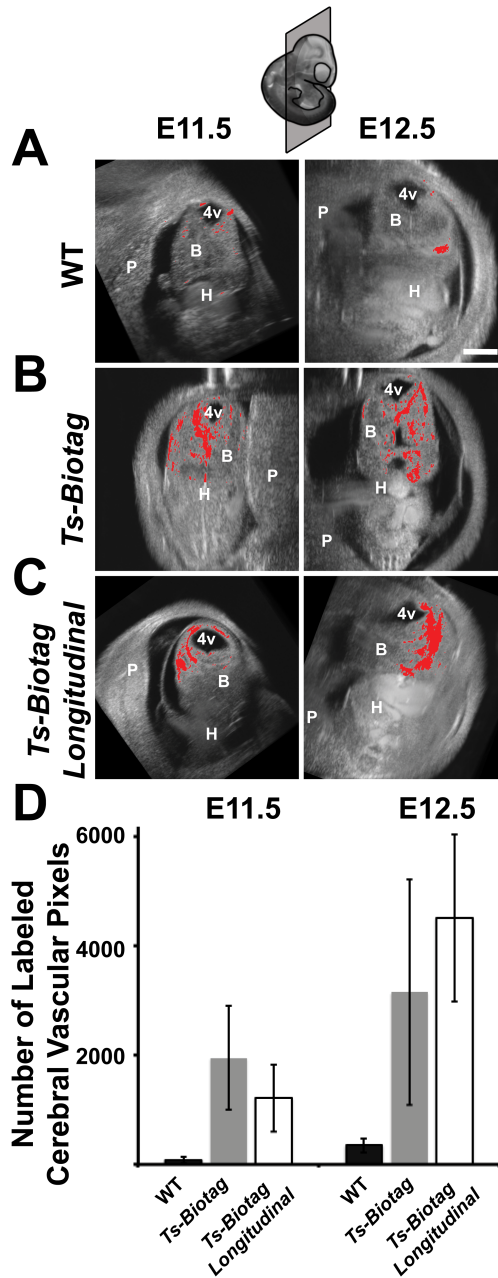


Figure 2.9 Targeted UBM of embryonic vasculature in Ts-Biotag mice.

Time averaged images were generated from 2D cine *in vivo* ultrasound biomicroscopy (UBM) images of E11.5 and E12.5 WT (**A**) and Ts-Biotag (**B**) embryos (N=7 for each genotype and stage), 20 minutes after injection of Av-microbubbles. Threshold analysis (threshold = mean background signal intensity + 5 SD) demonstrated increased vascular labeling in transgenic embryos compared to WT, especially obvious in the cerebral blood vessels (CBV). The *in vivo* capability of UBM allowed for longitudinal targeted imaging. To demonstrate the practicality of this method, selected embryos were injected and imaged first at E11.5, and then again at E12.5 (N=3) (**C**). Quantitative analysis of cerebral vasculature showed significant increases in labeling in Ts-Biotag vs WT embryos at both E11.5 and E12.5, and between E12.5 and E11.5 in the longitudinal data (see text for statistical analyses). There were no significant differences between longitudinal and single time point measurements at either E11.5 or E12.5 (**D**). Other labels: heart, H; dorsal aorta, DA. Scale bar = 1mm.

Multimodality imaging of VEGF-induced vascular development:

In vivo models have shown that Tie2 signaling by Angiopoietin (Ang1) enhances VEGF induced angiogenesis (Asahara et al., 1998; Chae et al., 2000), while upregulation of Ang1 has also been observed in response to

VEGF (Gamble et al. 2000). Based on data showing Ang1 signaling was sufficient to increase Tie2 expression in cell culture(Christensen et al. 2002), we asked whether the *Ts-Biotag* transgene was upregulated in an adult model where neovascular development was induced by VEGF alone. For this purpose, we used a subcutaneous implantation of matrigel supplemented with VEGF(Akhtar et al. 2002). Similar to many tumors, matrigel plugs have poor vascular integrity, readily extravasating small molecular probes such as DTPA-Gd (Magnevist, Berlex) (**Figure 2.10**). Using larger molecular-weight probes based on avidin and streptavidin, we did not detect any obvious vascular permeability in the matrigel plugs (**Figure 2.10**), which allowed us to use time-dependent signal changes to assess vascular labeling.

VEGF-supplemented matrigel plugs in both WT and *Ts-Biotag* mice were highly vascularized 5-days after implantation. Intravascular injection of Av-FITC and exposure of the plugs under a fluorescence dissecting microscope showed virtually no labeling in WT mice (**Figure 2.11A**; N=4 WT; N=6 *Ts-Biotag*) compared to highly specific vascular labeling in *Ts-Biotag* mice (**Figure 2.11B**; N=6). At 14-days post implantation, matrigel plugs were still highly vascularized in both WT and *Ts-Biotag* mice (N=4 for each genotype), but minimal Av-FITC labeling was observed in *Ts-Biotag* mice (**Figure 2.7A**), indicating that transgene expression was only elevated in developing vasculature, similar to previous reports in other *Ts* transgenic

mice¹⁶. Immediately after imaging the matrigel plugs, we also dissected the brain and spleen of *Ts-Biotag* mice, observing low-levels of Av-FITC vascular labeling in these adult tissues, far below the levels seen in the matrigel plugs or in E11.5 mouse embryos (data not shown).

Comparing noninvasive NIR images of matrigel plugs after intravascular injection of the NIR probe SAV-680 into 5-day WT (**Figure 2.11D**; N=8) and *Ts-Biotag* mice (**Figure 2.11E**; N=15), there was obvious labeling, in patches, only in the transgenic mice, especially around the periphery of the plugs and in blood vessels feeding into the brightly labeled patches. This labeling in vessels feeding into the plugs was consistently observed in all *Ts-Biotag* mice, even at the relatively low spatial resolution of whole body NIR. This more distal activation of *Tie2* has not been previously described in other *Tie2* transgenic mice, likely because of the lack of whole animal imaging to assess regions away from the active angiogenesis.

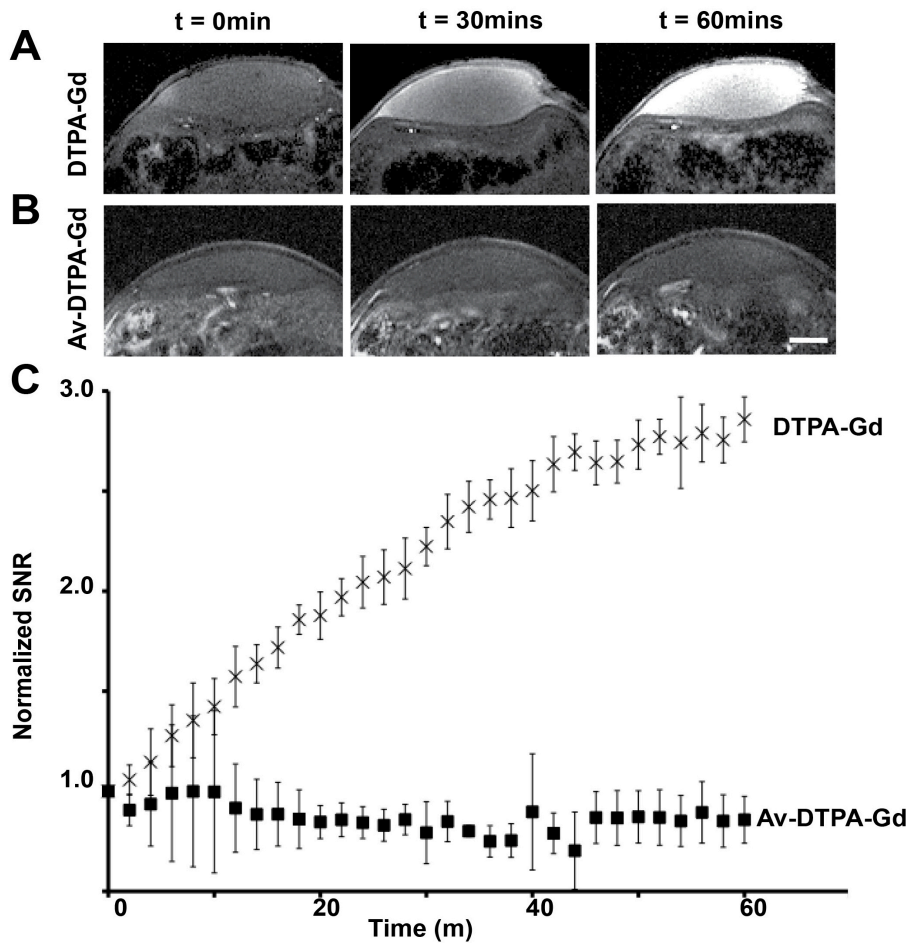


Figure 2.10 Matrigel plug vasculature is permeable to DTPA-Gd

Before injection of contrast agents, matrigel plugs had no obvious contrast compared to surrounding tissue (**A**). Injection of DTPA-Gd (Magnevist, Berlex) led to contrast beginning around the edges of the plug, moving towards the interior and nearly becoming uniform throughout the plug by 60 minutes post injection. Conversely, Av-DTPA-Gd injections into WT animals showed no increase in contrast over the entire time course (**B**). Quantitative ROI analysis of WT matrigel plug signal-to-noise ratio (SNR) was performed over time for DTPA-Gd and for Av-DTPA-Gd (**C**). The DTPA-Gd line shows an increase over time, fitting with first order saturation kinetics curve. Non-specific labeling due to extravasation of agent was not apparent in WT mice injected with Av-DTPA-Gd, most likely due to the much higher molecular weight of the agent compared to DTPA-Gd (~100x). DTPA-Gd (Magnevist) was administered via tail vein injection at 0.2mmol/kg, 50x the Av-DTPA-Gd dosage but only 2x the standard clinical dosage. (N=4 for each contrast agent). Scale bar = 2mm.

As with Av-FITC, SAv-680 labeling of *Ts-Biotag* matrigel plugs was virtually undetectable 14 days post matrigel implantation (**Figure 2.11B**). In longitudinal studies in 5-day matrigel, labeling of larger feeding vessels faded away approximately 6 hours after injection of SAv-680, though some areas persisted (**Figure 2.11C**; N=3). Using a second avidinated probe, SAv-800, injected 6h after the initial injection of SAv-680, most of the faded vessels could be relabeled and even areas of persistent labeling readily took up new agent (**Figure 2.11D**; N=4). In addition, some new regions of labeling appeared at the 6h relabeling time. Based on the observation that persistent areas consistently relabeled in these experiments, an area that does not relabel is most likely legitimately devoid of Tie2 expression rather than saturated with photobleached agent. This is an important distinction especially at longer time-points up to 24 hours where differences in relabeling were even more prevalent (data not shown). These data indicate that Tie2 regulation in vascular development changes within hours, but *Ts-Biotag* still works well as a pulse label during this highly dynamic process.

To obtain information related to vascular labeling deep below the surface of the skin, 5-day matrigel plugs were also imaged with MRI before and after injection of Av-DTPA-Gd, in WT (**Figure 2.12A**; N=8) and *Ts-Biotag* (**Figure 2.12B**; N=9) mice. WT plugs remained unchanged after injection of Av-DTPA-Gd, while there was an obvious increase in post-injection signal

intensity in all *Ts-Biotag* mice. Labeling was obvious in the surface vasculature feeding the plug, consistent with NIR imaging, and in vascular tissue below the plug, which was not accessible by any other method. Mice awake and behaving normally during the time between injection and MRI, showed highly significant differences in contrast between WT and *Ts-Biotag* mice (**Figure 2.12B**; $p < 0.001$, $N = 4$ in each group). This increase in contrast in the *Ts-Biotag* mice could be blocked with an equivalent dose of unlabeled avidin (**Figure 2.12B**; $N = 4$). The blocking study indicates that the 10mg dosage of Av-DTPA-Gd was near saturation of all available biotin, suggesting that higher doses would not significantly improve MRI contrast. Time course MRI data acquired in (anesthetized) WT ($N=4$) and *Ts-Biotag* ($N=5$) mice demonstrated a gradual increase in signal-to-noise ratio (SNR) in the transgenic mice over an hour (**Figure 2.12C**).

Finally longitudinal MRI experiments were performed in *Ts-Biotag* mice after implanting matrigel plugs ($N=4$). Pre- and post (1h)- Av-DTPA-Gd images were acquired in each mouse at 4, 7, 9 and 14 days after implantation (**Figure 2.12D**). The results showed peak contrast enhancement at 7-days, with no enhancement at 14-days, consistent with the NIR results (**Figure 2.11**). It should be noted that although the MRI data acquired from matrigel plugs had spatial resolution below the level of individual blood vessels, they provided quantitative *in vivo* information related to *Tie2* expression and vascular labeling in this adult model of angiogenesis, impossible to obtain by

other existing methods. It is also apparent from the *in vivo* imaging results (both NIR and MRI) that *Tie2* upregulation occurs both within and distal to regions of VEGF-induced neovasculature, revealing a broader involvement of *Tie2* in vascular development, not easily appreciated from higher-resolution microscopic images. Taken together, our results show that the *Ts-Biotag* mice can be used for multimodal imaging and quantitative *in vivo* analysis of vascular development, from embryonic to adult stages.

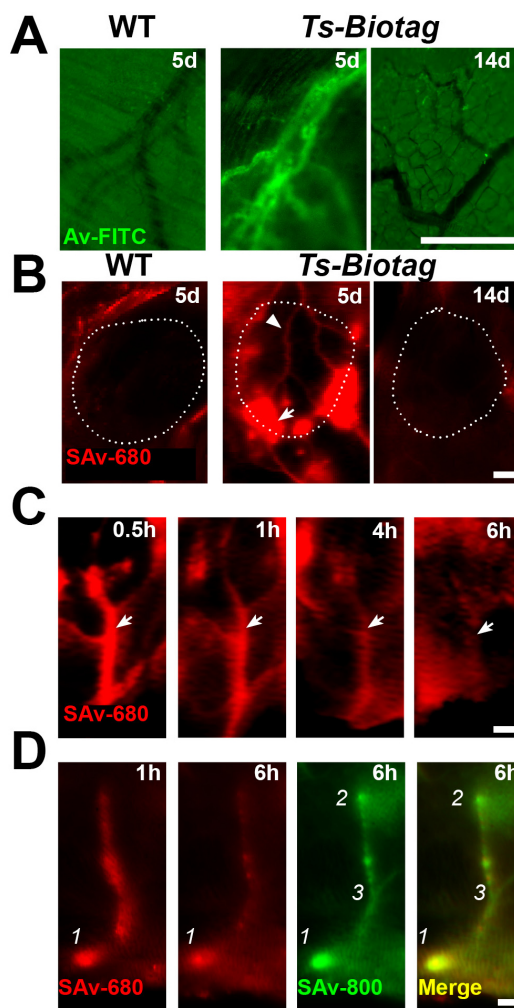


Figure 2.11 Targeted fluorescence and NIR imaging of VEGF-induced neovasculture in Ts-Biotag mice.

VEGF-doped matrigel plugs were imaged *in vivo* with a fluorescence dissection microscope (N=4 WT; N=6 Ts-Biotag) **(A)**. In 5-day (5d) plugs, injection of Av-FITC yielded no appreciable signal in surgically exposed WT plugs. Compared to WT, distinct labeling of blood vessels was obvious in Ts-Biotag mice. By 14d after matrigel implantation, Ts-Biotag mice showed almost no labeling. Similarly, *in vivo* NIR imaging 30 minutes after SAv-680 injection yielded no detectable labeling in 5d WT mice (N=8), while in 5d Ts-Biotag mice (N=15) bright labeling was visible through the skin in focal peripheral regions (arrows) and in blood vessels feeding into the plugs (arrowheads) **(B)**. As with the fluorescence imaging, NIR labeling was gone by 14d in Ts-Biotag mice (N=15). Time-course NIR imaging after SAv-680 injection showed obvious vascular labeling (arrows) in the feeding vessels up to 1h after injection, which faded significantly by 6h (N=3) **(C)**. Two color relabeling experiments demonstrated additional labeling in some areas (1), novel labeling in new regions of expression (2), and relabeling in faded vessels to show structural or expression changes over time (3) (N=4) **(D)**. Scale bars = 0.5 mm **(A)**, 1.5 mm **(B-D)**.

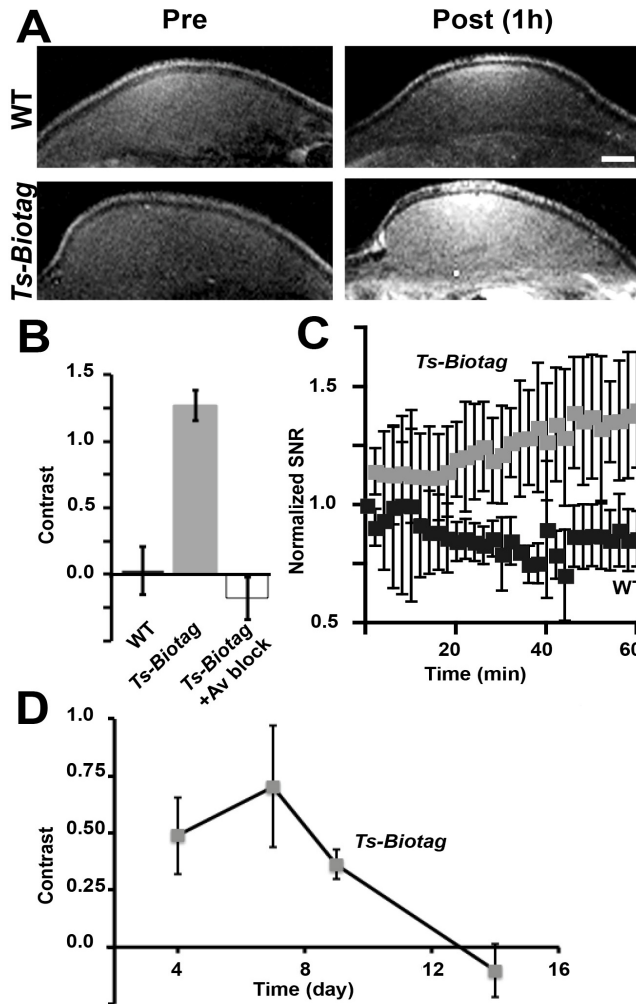


Figure 2.12 Targeted MRI of VEGF-induced neovasculation in Ts-Biotag mice.

In vivo MRI images acquired 1h after injection of Av-DTPA-Gd showed Ts-Biotag plugs (N=4) and the immediate surrounding tissue were clearly enhanced compared to WT (N=4) (A). Quantitative analysis of contrast 1h after injection of Av-DTPA-Gd showed a significant increase in Ts-Biotag (grey bar) compared to WT (black bar) mice (N=4 for each genotype) (B) (see text for statistical analysis). Administration of unlabeled avidin 1h before injection of Av-DTPA-Gd effectively blocked labeling in Ts-Biotag mice (N=4) (B). Rate of label uptake was imaged in time-course MRI (N=4 WT; N=5 Ts-Biotag). Injection of Av-DTPA-Gd showed an increase in signal-to-noise ratio (SNR) in Ts-Biotag (grey squares) compared to WT (black squares) mice over 1h (C). Matrigel plugs implanted into Ts-Biotag mice were imaged longitudinally, showing peak contrast enhancement at day 7 and no enhancement by day 14 (N=4) (D). Scale bar = 1mm.

2.4. DISCUSSION

The results presented in this paper clearly demonstrate the ability of the Biotag reporter system to display biotin on cell membranes, and the utility of the *Ts-Biotag* transgenic mice as a tool for research in vascular development. Our novel transgene was shown to amplify the amount of biotin labeling per reporter molecule, significantly improving cellular labeling efficiency with avidin-probes. After incorporation into *Ts-Biotag* transgenic mice, the Biotag reporter system was shown to enable efficient labeling of endothelial cells during vascular development in both embryos and adults. Using intravascular injection of commercially available or easily synthesized avidinated agents, we further demonstrated the potential of the *Ts-Biotag* mice for multimodality vascular imaging, including NIR, UBM, and micro-MRI. Our results strongly suggest that the *Ts-Biotag* mice will also be readily amenable to an extended range of applications, including studies of neovascular formation during tumor progression and wound healing, and for other imaging modalities such as micro-CT with avidin-iodinated agents, or for higher resolution, albeit more superficial imaging studies using multi-photon microscopy after injection of Av-FITC or other fluorescent probes.

The approach described in this study provides a modular, self-contained system for cell membrane biotinylation that can be used generally as a genetic reporter system in vascular endothelial cells. Compared to the

previously reported *biotin acceptor peptide (BAP)* (Tannous et al. 2006) or the 1xbiotag transgene, the 12xbiotag transgene resulted in a significant increase in membrane biotin (**Figure 2.3D**). Though we found the 12xbiotag construct to provide excellent biotin labeling in mice, our *in vitro* results suggest that the Biotag-BirA system is amenable to even more biotags per protein molecule with proportional improvements in biotin labeling, although there may be some risk of impairing vascular development with very high numbers of biotags.

In this study, we demonstrated the first labeling and analyses of *Tie2* expressing blood vessels in early stage embryos using avidin-coated ultrasound and MRI contrast agents. Furthermore, the longitudinal UBM imaging presented here is the first such analysis of mouse embryonic gene expression with ultrasound. The UBM images did require minor post processing before analysis in this study. However, “persistence imaging”, similar to the time-averaging approach adopted here, is already available on commercial ultrasound systems for online image processing. With recent advances in ultrasound imaging technology and image processing, we now have the means to analyze vascular development in individual embryos at multiple stages using truly *in utero* and real-time imaging.

Ex vivo micro-MRI images were acquired in fixed mouse embryos after *in vivo* labeling with Av-DTPA-Gd. Compared to previous reports of *ex vivo* micro-MRI of embryonic vasculature, the *Ts-Biotag* mice enable clearer

visualization of smaller cerebral and inter-somitic vessels at E11.5, suggesting that the contrast agent is more effectively delivered to these micro-vessels by the normal circulation than by perfusion of fixed embryos with a Gd-loaded gelatin solution (Cesar A Berrios-Otero et al. 2009). We have recently demonstrated *in utero* micro-MRI of late stage (E17.5) embryonic vasculature (Nieman et al., 2009; Berrios-Otero et al., 2011), providing optimism that future 3D and longitudinal MRI studies will be possible in developing mouse embryos. It should also be noted that ferritin-expressing transgenic mice were generated previously for MRI imaging of vascular endothelial cells (Cohen et al. 2007). Unfortunately, in these mice, the MRI signal and contrast change resulting from ferritin expression is very similar to the endogenous contrast produced by fetal blood (Cesar A Berrios-Otero et al. 2011), making it difficult to detect transgene expression. In comparison, the *Ts-Biotag* mice now provide an opportunity to test a range of MRI contrast agents and data acquisition methods to optimize *in utero* detection of embryonic vasculature.

Regarding the use of the *Ts* promoter for visualizing vasculature in embryonic and adult mice, it is important to understand the normal temporal and spatial patterns of *Tie2/Ts* expression. Consistent with previous studies in *Tie2-eGFP* mice, *Ts-Biotag* expression is minimally detectable in most adult tissues (data not shown) (Minami et al., 2003; Motoike et al., 2000; Schlaeger

et al., 1997). In addition, the *Tie2* receptor has recently been shown to express and function during lymphangiogenesis (Shimoda 2009). Future studies, utilizing avidinated probes delivered to the lymphatic system in *Ts-Biotag* mice, could therefore provide valuable new insights into this less studied part of the circulatory system.

In addition to *Tie2*, a number of alternative vascular promoters are also available, including *Flk1*, an earlier marker of vascular development that has been shown to be effective for expressing fluorescent proteins in vascular endothelial cells of transgenic mice (Fraser et al., 2005; Larina et al., 2009). Also, there are many intracellular markers of vascular development and inflammation that currently defy targeted imaging approaches such as HIF1, COX2 or any number of downstream elements that are upregulated in vascular endothelial cells but not displayed on their luminal surface. Promoters of these genes could be used to drive the expression of the Biotag reporter to visualize their expression patterns, for example using gene targeting to knock-in the *12xBiotag-IRES-BirA^{ER}* cassette into the HIF1 or COX2 locus. Visualizing the spatial and temporal dynamics of genetically-defined cells critically requires *in vivo* imaging with high temporal resolution and deep tissue penetration. The current studies represent the vanguard of vascular reporter gene imaging in mouse models. Indeed, this new technology introduces the full power of multimodal genetic imaging to the field of vascular biology.

2.5. METHODS

Cell transfection and biotinylation assay:

The *nxBiotag-BirA* constructs were transfected into HEK-293 cells and live cell staining was performed 36h later by incubating cells for 1h with avidin-FITC (Av-FITC; A2050, Sigma) or streptavidin-Alexa680 (SAv-680; 926-32231, Li-Cor). After live cell staining, cells were fixed prior to immunostaining and/or imaging with a fluorescence microscope (DM RXE, Leica) or a NIR scanner (Odyssey, Li-Cor).

Immunocytochemistry / Immunohistochemistry:

Immunostaining was performed on cells and cryo-histological sections (16- μ m) acquired from mouse embryos, using antibodies and protocols described in the Online Supplement. Images were acquired with a fluorescence microscope (DM RXE, Leica).

Animals:

Ts-Biotag mice were generated by zygote injection in the Skirball Transgenic Mouse Facility, and maintained under protocols approved by the Institutional Animal Care and Use Committee at NYU School of Medicine. All the results were generated from the two highest-expressing mouse lines (Figure 2.4).

Matrigel plugs:

Matrigel (BD Matrigel Matrix phenol-red free, BD Biosciences) was supplemented with VEGF (100ng/mL, V4512 Sigma) and injected subcutaneously (100 μ l) into anesthetized 5-8 week mice. All probes/contrast agents were injected *via* tail vein using a 27g needle: 150 μ g (1mg/ml) Av-FITC or 100 μ g (1mg/ml) SAv-680; 10mg (40mg/ml) Av-DTPA-Gd; 1.5 μ g (15 μ g/ml).

Fluorescence and NIR imaging:

After injection with Av-FITC, dissected mouse embryos and surgically exposed matrigel plugs were imaged using a fluorescence dissection microscope (MZ16F, Leica). For *in vivo* imaging of matrigel plugs, mice were injected with SAv-680 and imaged using a NIR scanner (Odyssey, Li-Cor) at a nominal resolution of 180- μ m.

UBM imaging and guided *in utero* injections:

Ultrasound biomicroscopy (UBM) experiments were performed on a Vevo-770 UBM scanner (VisualSonics) using an RMV-704 40-MHz transducer with nominal axial and lateral resolution of 40 and 80 μ m respectively. UBM-guided injections were performed using methods similar to those previously described (A. Liu et al. 1998). For targeted UBM imaging of the embryonic vasculature, 1- μ l of avidin microbubbles (Av-microbubbles)

was injected directly into the embryonic cardiac ventricle at E11.5 (1- μ l) and E12.5 (2- μ l).

MRI:

All MRI images were acquired on a 7-Tesla micro-imaging system (Bruker). For micro-MRI, embryos were injected with an avidinated chelated gadolinium, Av-DTPA-Gd (1- μ l), using the UBM-guided injection system. 1h after *in utero* injection, embryos were dissected and fixed, and imaged overnight using a 3D, T₁-weighted gradient echo (GE) sequence at isotropic resolution of 50- μ m (Cesar A Berrios-Otero et al. 2009). Matrigel plugs were imaged *in vivo* using a multi-slice 2D, T₁-weighted GE sequence, with 100- μ m in-plane resolution and a slice thickness of 500- μ m acquired in 2 minutes.

Expression constructs:

DNA constructs were based on the cassette *nxbiotag-PDGFR-TM-IRES-BirA^{ER}* (“*nxBiotag-BirA*”). ER-targeted *BirA^{ER}* was generated using long oligonucleotides and synthetic PCR on a codon optimized version of *BirA*¹. The single Biotag was constructed using synthetic oligos ligated into the pDisplay vector (Invitrogen). A modular multi-Biotag was designed and synthesized (BioBasic) The synthetic construct consists of a 3x Biotag flanked by a 5' Bgl2 and 3' BamH1 site. This 3x tag was concatenated into 6x and 12x versions by iteratively ligating into the BamH1 site. The 12x Biotag was then ligated Bgl2/BamH1 into a pDisplay vector (Invitrogen), then into

pCDNA3.1 (Invitrogen) upstream of *IRES-BirA^{ER}* for cell transfection. The *CMV* promoter was replaced with the *Ts (Tie2)* regulatory elements to generate transgenic mice.

Cell transfection and biotinylation assay:

The *nxBiotag-BirA* construct was transfected into HEK-293 cells (TransIT-LT1, Mirus). For optical microscopy, cells were cultured on poly-L-ornithine treated glass coverslips (26023, Fisher). Live cell staining was performed 36h after transfection by incubating cells for 1h with avidin-FITC (Av-FITC; A2050, Sigma) or streptavidin-Alexa680 (SAv-680; 926-32231, Li-Cor). After live cell staining, cells were fixed in 4% paraformaldehyde (10 minutes at 4°C) prior to immunostaining and/or imaging with a fluorescence microscope (DM RXE, Leica) or an NIR scanner (Odyssey, Li-Cor).

Immunocytochemistry / Immunohistochemistry:

Immunostaining was performed on HEK293T cells and cryohistological sections (16-µm) acquired from mouse embryos. Staining was accomplished using the following antibodies: mouse anti-HA (1:200 / abcam); goat anti-Myc (1:500 / abcam); rabbit anti-CNX (1:100 / abcam); mouse anti-Tie2 (1:500 / abcam); rabbit anti-biotin (1:1000 / abcam); rat anti-CD31/PECAM1 (1:100 / BD Biosciences). Secondary antibody staining was performed with Cy3 (red; polyclonal goat anti-rat IgG /Jackson Immunoresearch); Cy2 (polyclonal

donkey anti-goat IgG / Jackson Immunoresearch) FITC (green; polyclonal goat anti-rabbit IgG / Jackson Immunoresearch). Cell F-actin staining was performed using Phalloidin-546 (1:500 / Molecular Probes)¹⁹. Nuclear staining was performed using DAPI, dilactate (1:10,000 / Sigma). Images were acquired using a Leica DMIRE, CSU10 Yokogawa confocal scanner unit with EM-CCD Hamamatsu digital camera controlled using Volocity 5.2 (Improvision). ICC images were acquired using a 40X oil lens 1.25NA while IHC was acquired with a 20X air lens 0.7NA.

Measurements of neurovascular density were made using PECAM1 stained sections of embryos staged E11.5-E13.5 (N=3 animals/group 3 slides/animal). Vascular staining was defined as regions of signal +2SD above the mean signal and the fraction of threshold voxels was displayed as a %. Tie2 and Biotin expression was analyzed by selecting an ROI within the defined vasculature and measuring signal from Tie2 or Biotin staining normalized against PECAM1 (N=3 animals/group 3 slides/animal). Measurements were presented as a ratio of Tie2 or Biotin over PECAM1. All image visualization and analysis was performed using ImageJ (v1.4, NIH freeware).

Transgenic mice:

Genotype analysis on founder lines and their offspring was performed using PCR of tissue-derived (ear, tail, embryo) DNA, using the following primers:(5':CCARCAACAAGCACATCCAG;3':TCCCATCTGCTCAGGTAAGG. A limb from each embryo was separated and digested in proteolysis buffer (50mM Tris pH 8.8, 1mM EDTA, 0.5% Tween20, 20 μ g/mL Proteinase K) for genotype analysis by PCR. The remainder of each embryo was homogenized in tissue lysis buffer (RIPA buffer [50 mM TrisHCl pH7.4, 150 mM NaCl, 2 mM EDTA, 1% NP-40, 0.1% SDS] with 10 μ g/mL DNase1 and 1 Complete Mini protease inhibitor tablet/10 mL [Roche Diagnostics]) and incubated for 30min on ice before being combined with PAGE SDS loading buffer and incubated for 5 min at 95°C.

Samples were run on a PAGE-SDS gel and transferred to a PVDF-FL membrane for Western Blot using an antibody against the Myc epitope (1:2000 Abcam ab8226) integrated into the Bio-tag protein and against β -Actin as a normalization control(1:5000Abcam ab9106). The blots were then incubated with 2 secondary antibodies conjugated to Alexaflour-680 (1:800 Licor 926-3221) and 800 (1:800 Licor 926-32210) and quantitatively imaged for fluorescence on an NIR scanner (Licor Odyssey). The 3 highest expressing lines were retained for further studies.

Ultrasound contrast agents:

Targeted ultrasound contrast agents (Target-Ready MicroMarker, Visualsonics), consisting of avidin-coated, lipid shelled microbubbles, were reconstituted according to the manufacturer's specifications to a stock concentration of 2×10^9 micro-bubbles/ml with a mean diameter of 2.3 to 2.9 μm . Nontargeted microbubbles (MicroMarker, Visualsonics), without avidin, were used for visualizing injection of optical and MRI agents.

Synthesis of Av-DTPA-Gd:

Avidin (Av)-DTPA-Gd was synthesized by modifying a previous protocol²⁻³. Diethylene-triamine-pentaacetic dianhydride was reacted at a 20:1 molar ratio to avidin overnight at 4°C in 0.1M carbonate buffer (Ph8). The mixture was dialyzed in 1000X volume 0.1M NaCl overnight at 4°C. Gd was then directly combined with the Av-DTPA at a 10:1 ratio, and dialyzed again in 1000X volume 0.1M NaCl overnight at 4°C. The final Av-DTPA-Gd was concentrated to 40mg/ml using a 0.5mL centrifugal concentrator (Millipore).

Ultrasound guided micro-injections:

Pregnant mice were anesthetized with isoflourane. A single uterine conceptus was exposed through a midline incision of an anesthetized mouse into a phosphate buffered saline (PBS) filled Petri dish, carefully maintaining intact all maternal and embryonic vascular connections. With both the mother and PBS maintained at 37°C, the imaging transducer was lowered and the

beating heart located. A 50- μm beveled micro-injection needle was placed inside the most proximal cardiac ventricle for injection and UBM monitoring. Intracardiac injections of optical and MRI contrast agents were visualized by coinjection of 100-nl of non-targeted microbubbles.

UBM data acquisition:

For each injected embryo, 2D cine loops (300 frames acquired in 10s) were acquired preinjection, immediately postinjection, and again 20 minutes postinjection. Temperature was maintained at 37°C during the imaging session, and heart rate maintained above 160 beats per minute to ensure proper circulation of contrast agent throughout the vasculature. For longitudinal analysis, this procedure was performed on 2 embryos per pregnant females. Mice were sutured and allowed to recover for 24h before the procedure was repeated at E12.5. Image visualization and average intensity projection (AIP) analysis were performed using ImageJ (v1.4, NIH freeware). Averaged images were thresholded at 5SD above the average signal from a non-enhancing ROI. Pixels above threshold are labeled in red. Further quantitative analysis was conducted by selecting an ROI around the head of the embryo. Analysis focused on neurovasculature and to avoid injection artifacts around the heart.

Micro-MRI data acquisition:

For micro-MRI, embryos were injected *in utero* with an avidinated, chelated gadolinium, Av-DTPA-Gd (1- μ l), using the UBM-guided injection system. Embryos were dissected 1h after *in utero* injection, and maintained in warm PBS at 37°C for 30 minutes to clear the blood. Embryos were then fixed in 4°C, 4% paraformaldehyde (PFA), and mounted inside a 30-ml syringe for multi-embryo imaging. Imaging was performed using a 3D T₁-weighted gradient echo sequence (echo/repetition times, TE/TR = 6.25/50 ms; flip angle, FA = 40°; matrix = 512³; isotropic resolution = 50 μ m; total imaging time = 7 h 17 min).

Embryo image analysis:

Individual embryo images were segmented from 2D UBM or 3D micro-MRI datasets containing images of multiple embryos using a combination of Analyze (v7.0, AnalyzeDirect) and Amira (v4.1, Visage). Histogram analyses were performed with ImageJ to detect the voxels more than 3 standard deviations above the mean background signal intensity, measured in a region-of-interest (ROI) placed over a non-enhanced region of the embryo. Amira was used to generate micro-MRI MIPs and visualizations of threshold-segmented vasculature for both UBM and micro-MRI.

Matrigel data collection and analysis:

Matrigel (BD Matrigel Matrix phenol-red free, BD Biosciences) was defrosted to 4°C on ice and supplemented with VEGF (100ng/mL, V4512 Sigma). 5-8wk WT and *Ts-Biotag* mice were anesthetized with isoflurane and injected subcutaneously (100µl), waiting at least 2 minutes post implantation before removing anesthesia to allow the matrigel to warm and solidify.

All probes/contrast agents were injected *via* tail vein using a 30g needle in the following amounts: 150µg (1mg/ml) Av-FITC; 100µg (1mg/ml) SAv-680; 10mg (40mg/ml) Av-DTPA-Gd. For florescence imaging 30min after Av-FITC injection, the dermis of anesthetized mice were opened to expose the matrigel plugs. NIR imaging was also conducted 30min post injection of agent and animals were again anesthetized using isoflourane for the duration of the imaging procedure. Mice were carefully shaved and placed on an NIR scanning bed for whole animal imaging (Li-cor). Scanning took ~15min/mouse.

MRI data were acquired with a 2D multi-slice T₁-weighted gradient echo sequence (TE/TR = 4.7/25ms; FA = 90°; 100µm in-plane resolution; slice thickness = 500µm; total imaging time = 2min). Signal intensities from regions-of-interest covering the matrigel plug were divided by the standard deviation of the background (air) noise to compute signal-to-noise ratio (SNR),

and normalized to the SNR of the pre injection image. Contrast was computed as (Post-Pre)/Pre normalized SNR. Post injection images were acquired 45m-1h post injection owing to variability in setup time. Longitudinal data was acquired at 4,7,9 and 14 days post implantation. In these experiments, signal from the matrigel ROI was normalized against that of an external $GdCl_3$ standard that also served to mark the location of the plug. Contrast was computed as (Post-Pre)/Pre normalized CR.

2.6. ACKNOWLEDGEMENTS

This research was supported by NIH grant R01 HL078665. We acknowledge the assistance and support of the Transgenic Mouse Core Facility of the NYU Cancer Institute in generating the *Ts-Biotag* transgenic mouse lines. We thank Dr. William Aird (Beth Israel Deaconess Medical Center, Boston MA) for providing the *Ts* promoter-enhancer elements, Dr. Vasily Orgryzko (Institut Gustave Roussy, Paris France) for providing the codon-optimized *BirA* cDNA, and Drs. Ralph Weissleder and Bakhos Tannous (Massachusetts General Hospital, Cambridge MA) for providing the *BAP* cDNA. We also thank Kamila Szulc and Brian Nieman for advice on the MRI protocols, and Sida Li for assistance with the initial genotyping and immunohistochemistry of the *Ts-Biotag* mice. Finally, we thank Dr. Glenn Fishman (NYU School of Medicine) and Dr. Alexandra Joyner (Sloan Kettering Institute, New York NY) for critical review of the manuscript.

3. DIVALENT METAL TRANSPORTER, DMT1: A NOVEL MRI REPORTER PROTEIN

This chapter is in submission for publication as:

Divalent Metal Transporter, DMT1: A Novel MRI Reporter Protein

Benjamin B. Bartelle^{1,2}, Kamila U. Szulc^{1,3}, Giselle A. Suero-Abreu^{1,3}, Joe J. Rodriguez¹ and Daniel H. Turnbull^{1,2,3,4,5,*}

¹Kimmel Center for Biology & Medicine at the Skirball Institute of Biomolecular Medicine, the ²Molecular Biophysics and ³Biomedical Imaging Graduate Programs, and the Departments of ⁴Radiology and ⁵Pathology
New York University School of Medicine, New York NY

Attribution of Data:

B.B.B. and D.H.T. designed the experiments and wrote the manuscript. B.B.B. performed all the experiments and analyzed the results. K.U.S. contributed methods for MRI acquisition and analysis. J.J.R. and G.A.S-A. contributed methods and assisted in the tumor implantation and imaging experiments.

3.1. ABSTRACT

Manganese (Mn)-enhanced MRI (MEMRI) has found a growing number of applications in anatomical and functional imaging in small animals, based on the cellular uptake of Mn ions in the brain, heart and other organs. Previous studies have relied on endogenous mechanisms of paramagnetic Mn ion uptake and enhancement. To genetically control MEMRI signals, we reverse engineered a major component of the molecular machinery involved in Mn uptake, the divalent metal transporter, DMT1. DMT1 provides positive cellular enhancement in a manner that is highly sensitive and dynamic, allowing greater spatial and temporal resolution for MRI compared to previously proposed MRI reporters such as ferritin. We characterized the MEMRI signal enhancement properties of DMT1-expressing cells, both *in vitro* and *in vivo* in mouse models of cancer and brain development. Our results show that DMT1 provides an effective genetic MRI reporter for a wide range of biological and pre-clinical imaging applications.

3.2. INTRODUCTION

MRI is a widely used and powerful tool for biological and clinical imaging, providing a wealth of *in vivo* anatomical and functional data from the most widely used animal model systems, including the mouse. Compared to other live animal imaging methods, MRI does not suffer the limitations in tissue penetration of optical microscopy or ultrasound, and has much better spatial resolution than bioluminescence or micro-PET (Nieman et al. 2007). Despite these advantages, moving MRI into the realm of “molecular imaging” by developing effective MRI reporter genes continues to be a major challenge (Gilad, Winnard, et al. 2007).

Development of an MRI reporter is fundamentally different from the fluorescent proteins commonly used for optical imaging. While protein sequences have been identified recently that can induce changes in chemical shift or frequency of the NMR signal (Gilad, McMahon, et al. 2007), no known protein directly affects the T_1 and/or T_2 relaxation times, which are the basis for image contrast in conventional MRI. Instead second order effects of proteins have been explored, mostly their interactions with paramagnetic metals such as iron (Fe), which function as contrast agents by reducing T_1 and/or T_2 . MRI also suffers from low sensitivity compared to fluorescence, which has motivated studies of enzymatic (Louie et al., 2000; Westmeyer et al., 2010) and cumulative (Moore et al., 1998; Weissleder et al., 1997)

mechanisms to localize metals. Thus far, the strongest candidate for an MRI reporter has been the Fe storage protein, Ferritin (Genove et al. 2005) (B. Cohen et al. 2007). Despite initial promise, Ferritin continues to face technical challenges that have limited its application for *in vivo* imaging, including the need for very high levels of Ferritin (Genove et al. 2005) and/or Fe (Deans et al. 2006), slow switching of MRI signals as Fe accumulates in Ferritin (Iordanova et al. 2010b), and unpredictable effects on T_2 relaxation in different cell types and tissues (B. Cohen et al. 2007).

Given the limitations of Ferritin, we decided to take a fundamentally different approach to developing an MRI reporter. The field of manganese (Mn)-enhanced MRI (MEMRI) is already rapidly growing in terms of versatility and applications (Silva et al., 2004; Pautler, 2006). In the nervous system, MEMRI has been developed for both activity imaging and tract tracing based on the permissivity of calcium (Ca) channels for Mn ions and subsequent axonal transport of Mn (Lin and Koretsky, 1997; Pautler et al., 1998; Aoki et al., 2004; Yu et al., 2005). However, Ca channels are not the sole means of Mn uptake in cells; indeed, DMT1 has been shown to actively transport Mn and other divalent metals (M. D. Garrick et al. 2006), and the high affinity of DMT1 for Mn has been characterized in several tissues (Bai et al. 2008). Based on this observation, we explored the utility of DMT1 as a reporter protein for MRI.

3.3. RESULTS

DMT1 expression correlates with MEMRI signal in the neonate mouse brain:

Using standard MEMRI protocols to image the brain of a post natal day 5 (P5) mouse, two of the most apparent areas of contrast are the cerebellum (**Figure 3.1A,B**) and the hippocampus (**Figure 3.1D,E**). Immunohistochemistry showed these regions of T_1 enhancement correlate with immunostaining (**Figure 3.1C,F**). However, other tissues such as the olfactory bulb were also enhanced on MEMRI images, but without appreciable DMT1 staining (data not shown). These data show that DMT1 expression correlates with MEMRI enhancement in selected brain regions, but enhancement is not dependent solely on the presence of DMT1, as expected since alternative mechanisms of cellular Mn uptake, for example *via* active Ca channels, are well established (R G Pautler 2006). This evidence, together with previous reports of cellular Mn uptake *via* DMT1 (M. D. Garrick et al. 2006), provided the motivation to investigate the potential of DMT1 expression to control MEMRI signal enhancement.

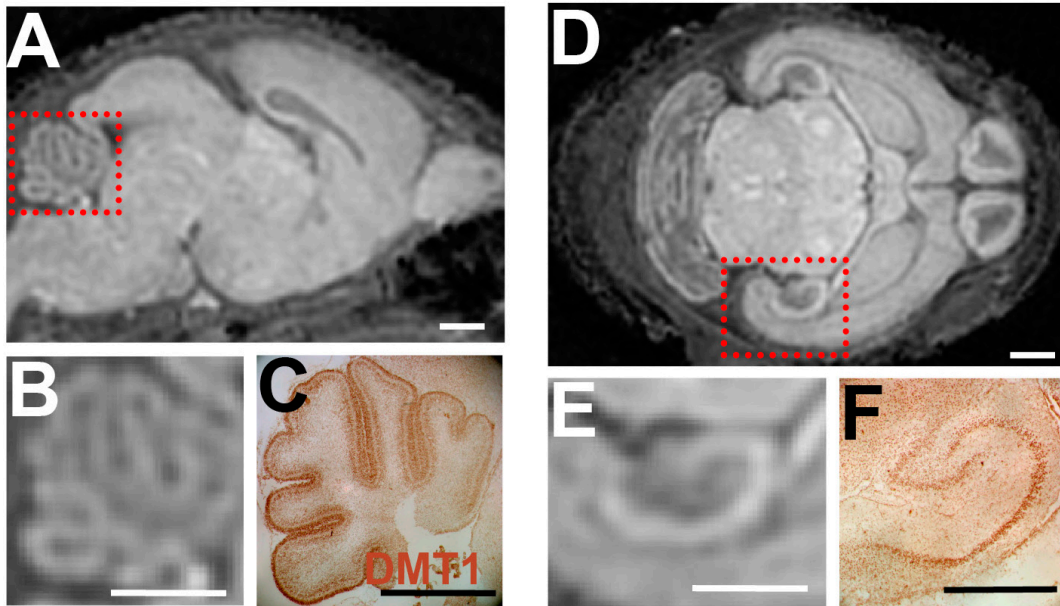


Figure 3.1 DMT1 expression and MEMRI signal are correlated in the neonatal mouse brain.

Immunostaining for DMT1 was compared qualitatively to MEMRI enhancement patterns at postnatal day (P)5. Sagittal MRI images showed enhancement in the outer layer of the cerebellar cortex, corresponding to the external granule layer (EGL) (A, and magnified inset in B). This enhancement pattern in the cerebellum was very similar to the DMT1 immunostaining results in matched histological sections (C). In addition to cerebellum, MEMRI also showed marked enhancement in the hippocampus (D, and magnified inset in E). Again, DMT1 immunostaining correlated with the MEMRI enhancement pattern in the hippocampus (F). Scale bars = 1.0-mm (A-F).

DMT1 with Mn supplementation strongly effects R_1 , a critical aspect of MEMRI contrast:

To study the effects of DMT1 on MEMRI signal and contrast, we first generated cell lines with varying levels of DMT1, by expressing the protein or an shRNA to knockdown DMT1 expression (**Figure 3.2**). The knockdown cell line (-DMT1) reduced DMT1 expression to approximately 0.6-fold, while the overexpressing (+DMT1) lines increased DMT1 levels up to 3-fold (**Figure 3.2A**). It should be noted that these differences in expression level are very low compared to the reported 60-fold overexpression of Ferritin necessary to detect significant changes in MRI contrast (Iordanova et al. 2010b). Cells were supplemented for 1h with $MnCl_2$ at a level approximating that of a standard dose for rodent MEMRI ($300\mu M$) (Yu et al. 2005), and the live cells were imaged using a T_1 -weighted sequence. The results showed excellent qualitative correlation between DMT1 expression and MEMRI signal levels (**Figure 3.2B**; $n \geq 6$ for each cell type). Notably, the level of signal enhancement in the +DMT1 cells was on par with even the most recently engineered targeted chemical agents (Westmeyer et al., 2010; Strauch et al., 2011).

To quantify the Mn-dose dependent effects of *DMT1* expression in the HEK cell lines, we analyzed the relaxation rate, R_1 ($=1/T_1$), which is directly related to T_1 -weighted signal level (**Figure 3.2C**). Without supplementation

with MnCl_2 there was no difference between cell lines, but even low levels of Mn ($100\mu\text{M}$) had a significant effect on R_1 . All cell lines showed some response to increasing levels of Mn, but naive HEK cells and the knockdown cell line were relatively insensitive compared to the +*DMT1* cells, which demonstrated up to a 4-fold increase in R_1 above control HEK cells following supplementation with $300\mu\text{M}$ Mn. This substantial shift in R_1 was consistent with a large increase in Mn uptake caused by DMT1 overexpression, as shown in previous studies (M. D. Garrick et al. 2006). To address the concern that these levels of Mn might cause cell toxicity, especially in the +*DMT1* cells, an MTT assay for cell viability (Deans et al. 2006) was performed, showing no significant difference between control and +*DMT1* HEK cell lines, with or without $300\mu\text{M}$ Mn supplementation (data not shown). The fact that *DMT1* expression can induce R_1 increases 4-fold above control cells within 1h of Mn supplementation is a major advantage compared to even the most recently engineered Ferritin, which required 24h supplementation with 1mM Fe for a 1.8-fold increase in R_2 (Iordanova et al. 2010b), or tyrosinase (a melanin-related enzyme), which required 96h in $250\mu\text{M}$ Fe to achieve a 1.4-fold increase in R_1 (Paproski et al. 2011). Taken together, these results indicated a high potential for *DMT1* to be used as an MRI reporter gene.

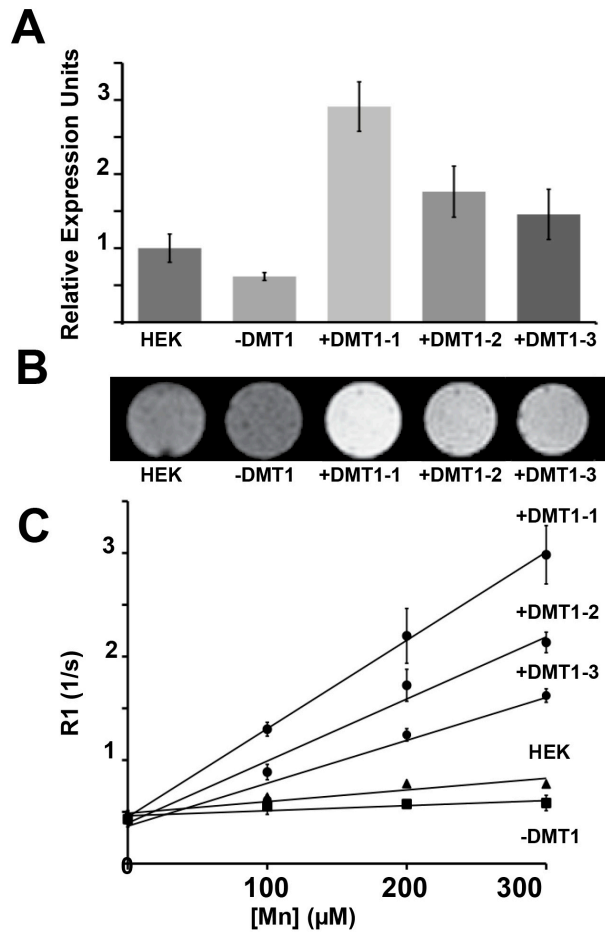


Figure 3.2 Effect of cellular DMT1 expression on MEMRI signals.

Relative levels of DMT1 expression were assayed in HEK293 cells, including an shRNA knock down line that reduced expression to 0.6-fold (-DMT1) and three cell lines that ectopically overexpressed DMT1 by up to 3-fold (+DMT1-1,2,3) (A). In T₁-weighted images after Mn supplementation, -DMT1 cells had a small but visibly reduced contrast compared to control HEK cells while +DMT1 cells had obvious increased contrast consistent with their relative expression levels (B). The effect of DMT1 expression on T₁ relaxation was quantified by measuring the Mn-dose dependent relaxation rate, R₁ (=1/T₁) for all cell lines (C). Without Mn supplementation all cell types had equivalent R₁ values. The +DMT1 cell lines showed substantial increases in R₁ up to 4-fold at 300μM MnCl₂, consistent with the measured DMT1 expression levels. The -DMT1 cells showed a small but significant reduction in R₁ at MnCl₂ concentrations above 100μM.

DMT1 expression affects R_1 in diverse cell types with Mn supplementation and creates contrast for *in vivo* MEMRI:

HEK cells in culture were convenient for initial testing because of their high levels of expression, but do not necessarily reflect physiological conditions where transgene levels can be quite limited and Mn exposure is not nearly so controlled. We therefore characterized DMT1 related MRI effects using two tumor cell lines: B16 melanoma, and GL261 glioma (**Figure 3.3**). Both cell lines are tumorigenic after implantation in C57Bl/6 mice, allowing comparisons under *in vitro* and *in vivo* conditions. Since *in vivo* MEMRI imaging typically begins 3 to 24 hours after injection of Mn (Silva et al., 2004; Pautler, 2006), we also examined the long-term retention of Mn in each cell line to establish parameters for *in vivo* imaging.

Naive B16 cells showed a slightly higher response to increasing Mn levels than HEK cells (**Figure 3.3A**). Retroviral transfection of DMT1 into B16 cells generated a maximal 1.4-fold overexpression of *DMT1* ($p=0.009$, $n=6$), which resulted in a 1.8-fold increase in R_1 in *+DMT1* compared to control B16 cells after 1h supplementation in $300\mu\text{M}$ Mn ($p<0.001$, $n=9$; **Figure 3.3A**). Upon removal of Mn, R_1 decreased rapidly for both control and *+DMT1* B16 cells, returning to baseline levels within 4 hours (**Figure 3.3B**), suggesting that Mn was quickly excreted from B16 cells and that *in vivo* imaging would require minimal time between Mn supplementation and data collection. Mice

were subcutaneously implanted with control and +*DMT1* B16 melanoma cells on opposite flanks and allowed to grow to overt tumors, allowing for direct comparison of the two cell types in each mouse. R_1 differences characterized in culture translated to a significant difference between *in vivo* T_1 -weighted MRI images of control and +*DMT1* B16 tumors ($+22 \pm 9\%$ contrast in +*DMT1* tumors: $p=0.01$, $n=3$; **Figure 3.3C**), acquired 3h after Mn administration *via* intraperitoneal (IP) injection of $MnCl_2$. Consistent with the cell culture experiments, Mn-enhancement and contrast between +*DMT1* and control B16 tumors was markedly reduced by 4h ($+13 \pm 2\%$ contrast: $p<0.001$, $n=3$) (data not shown).

GL261 glioma cells were also investigated, using retroviral transfection to generate cells with maximal 1.3-fold overexpression of *DMT1* ($p=0.001$, $n=6$). Similar to B16 cells, *DMT1* overexpression in GL261 cells resulted in a 1.6-fold R_1 increase after 1h supplementation with $300\mu M$ Mn ($p<0.01$, $n=9$; **Figure 3.4A**). Interestingly, GL261 cells demonstrated very different timecourse characteristics compared to B16 cells. After the initial uptake of Mn, the R_1 gain in +*DMT1* relative to control GL261 cells persisted over more than 24h (**Figure 3.4B**). These cellular dynamics fit well into the 24h post Mn injection imaging paradigm used for many previous *in vivo* MEMRI studies (Afonso C Silva et al. 2004) Yu et al. 2005; (R G Pautler 2006).

After stereotaxic implantation into the brain, control and +*DMT1* GL261 cells were allowed to grow into overt tumors (one per mouse). Before Mn-injection, control and +*DMT1* GL261 tumors were both hypo-intense compared to adjacent brain tissue ($-14 \pm 4\%$ contrast in controls vs $-14 \pm 6\%$ in +*DMT1* tumors, $n=4$ for each tumor type; **Figures 3.4C, D**). Images acquired 24h after Mn-injection showed minimal enhancement in control tumors, resulting in further hypo-intensity compared to adjacent brain tissue ($-21 \pm 15\%$ contrast, $n=4$; **Figure 3.4C**), while +*DMT1* tumors showed significant enhancement compared to adjacent brain tissue ($+33 \pm 13\%$ contrast, $n=4$; **Figure 3.4D**). Comparing +*DMT1* to control GL261 tumors, the overall gain in contrast was $+75 \pm 30\%$ ($p<0.001$).

The substantial difference between the two tumor models points to an important area for future development of *DMT1* as an MRI reporter. Despite slightly higher levels of expression and initial R_1 gain of B16 over GL261 cells, +*DMT1* B16 melanomas showed reduced *in vivo* contrast due to their relatively poor retention of Mn. The Mn retention of a cell or tissue type is readily measurable using standard MEMRI, and this property will be important to determine for each application. Of note, the long-term retention of Mn in neural tissues has been well characterized for MEMRI, enabling a wide variety of neuroimaging studies in the mouse brain, from fetal to adult stages (Pautler et al., 1998; Aoki et al., 2004; Silva et al., 2004; Wadghiri et al., 2004; Pautler, 2006; Yu et al. 2005; Deans et al., 2008).

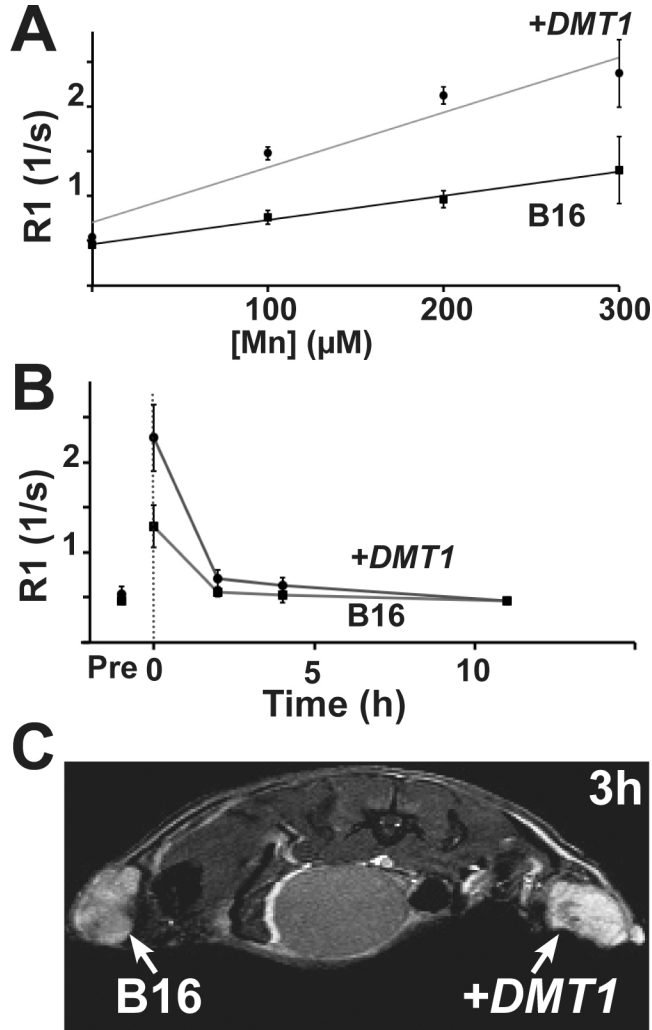


Figure 3.3 MRI analysis of DMT1 expression in B16 cells, *in vitro* and *in vivo*

Control B16 melanoma cells and a line overexpressing DMT1 (+DMT1) by 1.4-fold were investigated. In measurements of R_1 vs Mn concentration of a 1h supplementation of $MnCl_2$, DMT1 overexpression increased R_1 up to 1.8-fold in +DMT1 compared to control B16 melanoma cells (A). In time course measurements from cells before (Pre) and after $MnCl_2$ was removed (dotted line) (B). R_1 differences disappeared within 4 hours. MEMRI images were acquired 3h after $MnCl_2$ injection in mice with control (left) and +DMT1 (right) B16 melanomas. +DMT1 tumors had significantly higher signal than control B16 tumors in each mouse (n=3) (C).

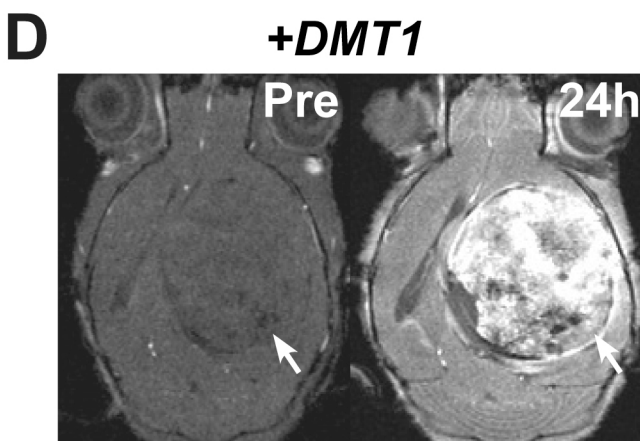
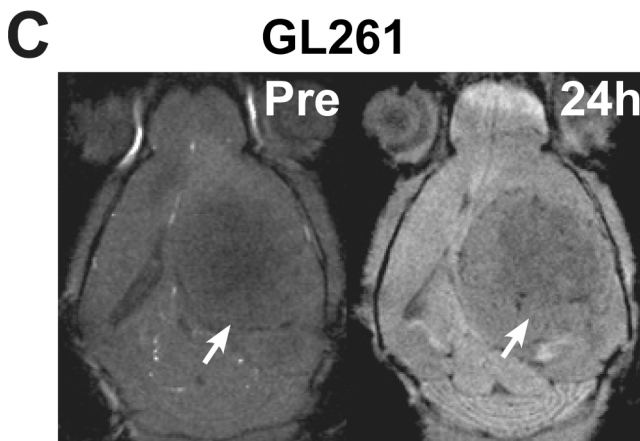
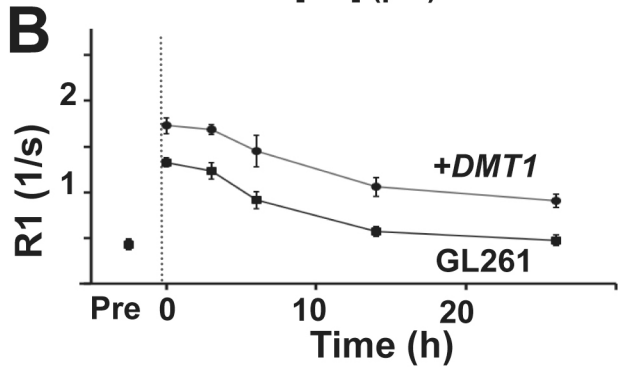
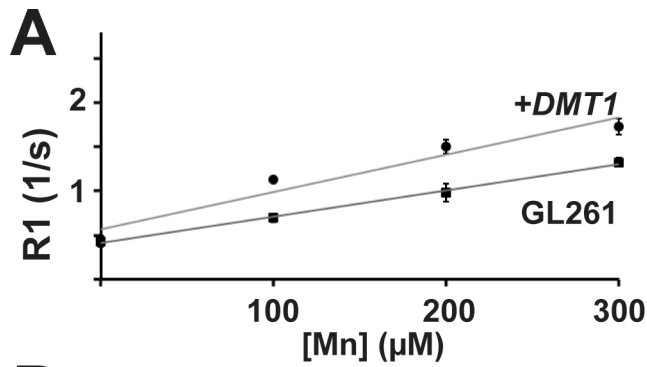


Figure 3.4 MRI analysis of DMT1 expression in GL261 cells, *in vitro* and *in vivo*.

Control GL261 glioma cells and a 1.3-fold overexpressing DMT1 cell line (+DMT1) were investigated. Increased DMT1 expression improved R_1 with a maximal R_1 gain of 1.6-fold, comparing +DMT1 and control GL261 cells (A). Time course R_1 measurements of control and +DMT1 GL261 cells before (Pre) and after $MnCl_2$ was removed (dotted line) (B). Unlike the B16 cells, contrast between control and +DMT1 GL261 cells was maintained for over 24h. Control GL261 tumors showed initial negative contrast compared to surrounding tissue (Pre) which became more pronounced in MEMRI 24h after injection of $MnCl_2$ (C). DMT1 expression did not alter the initial negative contrast in +DMT1 GL261 tumors (Pre), but Mn injection robustly enhanced +DMT1 tumors compared to adjacent brain tissue and control GL261 tumors (D).

Ectopic expression of DMT1 creates contrast for *in vivo* MEMRI of the neonate mouse brain:

To investigate the utility of the *DMT1* reporter gene for studies of mouse brain development, we used *in vivo* electroporation of a bicistronic vector (*DMT1-IRES-eGFP*) to ectopically co-express *DMT1* and *eGFP* in the neocortex. After electroporation at embryonic day (E)13.5 (Saito 2010) or postnatal day (P)0 (Boutin et al. 2008), mice were imaged with MEMRI at P1 or P5, respectively (**Figure 3.5**), with Mn delivery to the pups *via* lactation after a single maternal IP injection of $MnCl_2$ 8h before imaging. The patterns and levels of enhancement following electroporation were more variable than in the tumor studies, but there was an obvious unilateral enhanced region in each animal, as expected.

Overall, E13 electroporation resulted in expression that was diffuse and dorsal (**Figure 3.5A-C**), while P0 electroporation yielded more focal and lateral patterns of expression (**Figure 3.5A-E**). In all cases there was a clear qualitative correlation between *in vivo* MEMRI enhancement (**Figures 3.5A,D**) and both *DMT1* (**Figures 3.5B,E,F**) and *eGFP* (data not shown) expression, assessed in whole mount dissected brains and histological brain sections acquired immediately after imaging. The three-dimensional (3D) nature of MRI enabled volumetric rendering and segmentation of the enhanced regions using 3D analysis software (**Figure 3.5C,G**), making it easier to appreciate the full extent and pattern of each transfected region.

Quantitative analysis of the electroporation results showed an average 18% increase in contrast, comparing transfected and contralateral cortex (full range = 8-43%; $p < 0.001$, $n=6$).

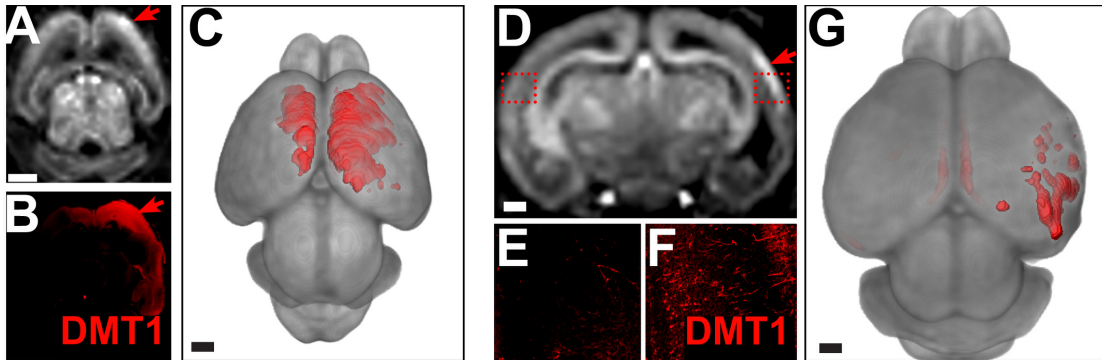


Figure 3.5 *In vivo* MRI analysis of ectopic DMT1 expression in the developing mouse neocortex.

MRI and histology of a brain electroporated at E13.5 with DMT1-IRES-eGFP, imaged *in vivo* at postnatal day (P)1, and harvested for correlative microscopy (**A-C**). MEMRI showed a largely unilateral pattern of dorsal cortical enhancement (**A**). Staining for DMT1 correlated well with the MEMRI enhancement pattern (**B**). Volumetric rendering of MEMRI data revealed the full 3D pattern of DMT1 expression (red = 1.5 sd above the mean cortical signal intensity) (**C**). MRI and histology of a brain electroporated at P0 with DMT1-IRES-eGFP, imaged *in vivo* at P5, and harvested for correlative microscopy (**D-G**). MEMRI showed a focal, unilateral region of cortical enhancement (**D**). Immunohistochemistry for DMT1 on coronal sections matched to the MEMRI images showed minimal expression in the contralateral cortex (**E**) compared to high levels of DMT1 expression in the region of MEMRI enhancement (**F**). Volumetric rendering of MEMRI data clearly demonstrated the lateral, focal cortical DMT1 expression pattern (red = 1.5 sd above the mean cortical signal intensity) (**G**). Scale bars = 0.5-mm (**A-G**).

3.4. DISCUSSION

These results clearly demonstrate how *DMT1*-expression, in combination with Mn supplementation, alters the T_1 -relaxation properties of a wide range of cell types, and creates readily visible signal enhancement in multiple *in vivo* models of expression and imaging with MEMRI. In all models, only a systemic dose of Mn was required through an IP injection to the adult mice or to nursing mothers for neonatal imaging. The two mouse tumor models demonstrate immediate applications in pre-clinical cancer imaging, and the electroporation studies demonstrate *in vivo* cell labeling and imaging of gene expression in the developing mouse brain.

There are several important areas for future development related to this new technology. Many tissues have some degree of endogenous Mn uptake, making optimization of signal to noise a challenge at low levels of *DMT1* expression. This may be addressed through more advanced image analysis methods, in which 3D MRI data is volumetrically registered to a reference atlas for differential analysis (Dorr et al. 2008). In this way, even very minor changes in contrast could be mapped, allowing for 3D imaging that is both quantitative and sensitive. Other areas for development are in the pharmacodynamics of Mn and the transient nature of *DMT1*-induced signal enhancement. Here we chose to use a single injection of $MnCl_2$, but Mn could also be delivered in multiple smaller doses (Bock et al. 2008) or in a

continuous low dose to minimize differences in Mn retention (Mok et al. 2012). The dynamic effect of *DMT1* on MEMRI contrast has advantages for longitudinal imaging in cases where rapid changes in expression occur, such as developmental studies or *in vivo* reporter assays.

Taken together, our results demonstrate that the divalent metal transporter, *DMT1* can be used as a robust and effective reporter system in combination with MEMRI, providing positive signal enhancement in *DMT1*-expressing cells, with much higher sensitivity and faster switching times than previously proposed MRI reporters. These advances now make it possible to access the power of mouse genetics and molecular imaging with the full 3D and *in vivo* capabilities of MRI.

3.5. METHODS

Cloning:

A *DMT1* construct including an integrated HA tag (Lam-Yuk-Tseung & Philippe Gros 2006) was cloned into a *pCAG* vector along with *IRES-eGFP* for co-expression of *DMT1* and *eGFP*. DNA was grown to high concentration for *in vivo* electroporations. The *pCAG-DMT1-IRES-eGFP* element was also cloned into a retroviral vector, and virus prepared as described previously (Gaiano et al. 1999).

DMT1 Stable Cell Lines:

All cell lines were cultured in DMEM +10%FBS. DMT1 expressing HEK, B16 and GL261 stable expressing cell lines were obtained by exposing cells to the DMT1 retrovirus for 48 hours. Cells were suspended placed and sorted with cell cytometry for eGFP for culture (Coulter MoFlo).

DMT1 knockdown cell lines were generated using a lentivirus carrying shRNA against the protein (Open Biosystems V2LMM_29721). Cells were exposed to virus according to product guidelines and placed under puromycin selection (1.5mg/mL) for 5 days.

Protein Expression Assay:

All cell lines were assayed for expression levels of DMT1 relative to β -actin. Cells were cultured on a 24 well plate, fixed with PFA, and stained for DMT1 (Abcam ab55812) and β -actin (Abcam ab8226) using infrared (IR) labeled secondary antibodies (LI-COR goat anti mouse IR-800 926-32210; and goat anti rabbit IR-680 926-3221). Plates were assayed on an IR scanner (Odyssey, LI-COR) and relative expression levels (DMT1/ β -actin) were shown as a fold change relative to control cells.

MRI of Cell Lines:

Each cell line was cultured to 90% confluency, and media was supplemented to the desired concentration of $MnCl_2$ for 1h. Cells were subsequently washed with PBS and removed from their plates using trypsin.

Loose cells were gently centrifuged for 1 minute at 800xg in 1.5mL microcentrifuge tubes, the trypsin was aspirated away and replaced with 1mL of cold DMEM and gently repelleted. The loose cell pellets were then pipetted directly into a 2.4mm NMR tube (New Era SK-210907) and centrifuged in the NMR tubes for an additional 1-minute at 800xg before being placed in a syringe phantom filled with cold DMEM for MRI.

Cell pellets were imaged on a 7T Bruker Biospec system, using a T_1 -weighted 2D multislice Gradient Echo (2DGE) sequence (echo time, TE = 3.1ms; repetition time, TR = 100ms; flip angle, FA = 45°) and a 2D multislice Spin Echo (2DSE) saturation recovery sequence (TE = 11ms; TR = 190ms, 500ms, 900ms, 1.5s, 3s), both with in-plane resolution of 100 μ m x 100 μ m and 500 μ m slice thickness. Slices with noticeable susceptibility artifacts due to air bubbles were excluded from measurements.

The 2DSE images with increasing TR values were used to calculate a T_1 map using the MRI Analysis Calculator Plugin for ImageJ. T_1 maps were calculated using $I(x,y) = K\rho(x,y) [1 - e^{-TR/T_1(x,y)}]$, where $I(x,y)$ is the signal intensity for a given pixel (x,y), K is a constant and $\rho(x,y)$ is the proton density, assumed to be constant for every pixel (x,y). Data were plotted as $R_1(=1/T_1)$ (mean \pm standard deviation, sd).

Animals and Tumor Models:

All mice used in these studies were maintained under protocols approved by the Institutional Animal Care and Use Committee at NYU School of Medicine. Melanomas were generated by injecting 10^6 B16 melanoma cells subcutaneously into both flanks of each C57Bl/6 mouse, and grown *in vivo* for 7-10 days before imaging. GL261 cells were prepared and injected stereotaxically into the brain of each C57Bl/6 mouse as described previously (Cha et al. 2003), and grown *in vivo* for 3 weeks before imaging. Mice were also electroporated with *pCAG-DMT1-IRES-eGFP* DNA according to published protocols at both E13.5 (Saito 2010) and P0 (Boutin et al. 2008), and imaged as neonates at P1 and P5, respectively.

***In Vivo* MRI:**

Mice were imaged using 2DGE (TE/TR=3.1/100ms; FA=45°; in-plane resolution = $100\mu\text{m} \times 100\mu\text{m}$; slice thickness = $500\mu\text{m}$) and 3DGE (TE/TR=3.1/100ms; FA=45°; isotropic resolution = $[150\mu\text{m}]^3$). Mice with tumors were given an IP injection of aqueous MnCl_2 (80mg/kg) and imaged 3h/24h post injection for B16/GL261 tumors. After electroporation, neonatal mice were imaged using the 3DGE sequence 8h after IP injection of MnCl_2 into the nursing mothers. All mice were anaesthetized with 1.5% isoflurane in air during MRI. 3D datasets were imported into Amira (Visage Imaging) for semiautomated segmentation of the brain and cortex. Within the cortex, a

threshold of 1.5-sd above the mean signal intensity was rendered as a surface (in red) and superimposed on semi-transparent 3D projections of the whole brain.

GFP imaging and IHC:

Perfusion fixed neonatal brains were extracted and imaged directly or dissected into 1mm coronal slices for imaging eGFP (Leica MZ16F). The brains were further sectioned (30 μ m) on a cryostat (Leica CM350S) and stained for DMT1 (Primary DMT1 antibody: Abcam ab55812; secondary antibody: Jackson Immuno 215-165-005 for microscopy and IR-680 926-3221 for IR brain slice imaging).

Statistical Analysis:

Expression and R_1 values were presented as ratiometric fold change compared to mean values of control cells (Test/Control). MRI contrast was computed as:

$$\text{Contrast} = (\text{Test}-\text{Control})/\text{Control}$$

The control regions were either contralateral tumors (**Figure 3.3C,D**), healthy brain tissue (**Figure 3.4CD**) or unelectroporated tissue (**Figure 3.5A,D**). All contrast values were expressed as a percentage difference. All p-values were calculated using a two-tailed Student's t-test, and variation was expressed as the sd.

3.6. ACKNOWLEDGEMENTS

This work was supported by NIH grant R01 NS038461 (to DHT) and the NIH/NYU GPP program for Structural Biology (to BBB). MRI was performed in the Mouse Imaging Core at NYUSOM, which was partially supported by the NYU Cancer Center Support Grant (NIH P30 CA0016087). We thank Anne Friedland (NYUSOM) for contributing to Figure 3.1, Dr. Songhai Shi (Sloan-Kettering Institute) for advice and instruction on electroporation methods, and Dr. Alexandra Joyner (Sloan-Kettering Institute) for general discussions and her loan of the electroporation equipment. We also thank Dr. Laura Garrick (SUNY at Buffalo) for providing *DMT1*-overexpressing cell lines used in early studies, and Dr. Philippe Gros (McGill University) for providing the *DMT1* DNA used to generate the constructs for these studies.

4. DATA CHAPTER 3: BIOLOGICAL Mn CONTRAST WITH METALLOPROTEIN MntR

Benjamin B. Bartelle^{1,2} and Daniel H. Turnbull^{1,2,3,4,5,*}

¹Kimmel Center for Biology & Medicine at the Skirball Institute of Biomolecular Medicine, the ²Molecular Biophysics and ³Biomedical Imaging Graduate Programs, and the Departments of ⁴Radiology and ⁵Pathology
New York University School of Medicine, New York NY

Attribution of Data:

B.B.B. and D.H.T. designed the experiments.
B.B.B. performed all experiments and analyzed results and wrote the manuscript.

4.1. INTRODUCTION

Metal chelates of paramagnetic metals are the workhorse agents of contrast enhanced MRI (Krause 2002). Attaching Gd or other paramagnetic atom to a chemical linker allows for chemical or biologically targeted imaging. Chelation also protects the subject from possible toxicity of a heavy metal ion. All of this comes with the cost of relaxivity as potential interactions between the paramagnetic atom and the spin lattice are reduced by chelation.

Compare this with Mn Enhanced MRI. The unchelated Mn can diffuse faster than any larger chelated agent, and the benefit of full coordination with the lattice certainly helps with a less potent paramagnetic metal like Mn, but the cost here is reliance upon the endogenous biology of Mn. Previously, methods to accrue Mn in cells by expressing the transporter DMT1 were explored (**Chapter 4**), yet experimental data suggested endogenous biology still heavily influenced Mn retention in any given cell type. Ideally the retention of Mn could be controlled such that enduring contrast would be available in any cell type. The most readily apparent way to achieve this is through biological chelation of Mn. MntR is the best available candidate for this method.

MntR is a metalloprotein originally identified in the bacteria *B. Subtilis*. Like all living organisms, *B. Subtilis* requires Mn as a trace element.

Excessive Mn can be toxic to cells as Mn readily interacts with Fe or Ca binding sites. To maintain a low level of Mn within the cell at all times, the bacteria must have a means of sensing Mn. MntR is that sensor (Patzner & Hantke 2001). In its Mn bound state MntR binds DNA, and acts as a repressor of SLCA2 metal transport proteins similar to DMT1 (Waters et al. 2011). The 17kD protein binds Mn with an affinity around 100nM, around the minimum necessary for healthy metabolism (Golynskiy et al. 2005). Moreover, MntR binds Mn with high specificity, meaning physiological levels of Fe or Ca are not competitive for binding. Only Cd has a similar affinity for the protein.

MntR's small size and specificity to Mn certainly are useful attributes, but the true promise of MntR lies in how it binds Mn. Mn is an essential cofactor for many enzymes such as Arginase II (Ilies et al. 2010), Prolidase (Vyas et al. 2010), and Superoxide Dismutase (Guan et al. 1998). Each of these proteins bind Mn, but upon analysis of their structure it is clear that Mn is kept deep within a binding pocket (**Figure 4.1**). This is not atypical of an enzyme reaction center, but such a conformation prevents ready exchange of water and therefore minimizes the ability of Mn to transfer energy to the spin lattice.

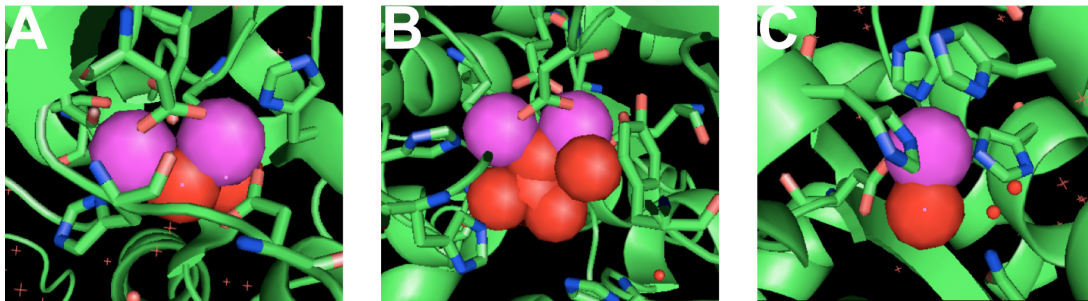


Figure 4.1 Metalloenzymes occlude Mn from the H spin lattice.

Structural data from several proteins shows binding of Mn (purple) to O (red) atoms from H₂O and PO₄. Arginase coordinates binuclear Mn directly with 2 O atoms from H₂O, with another structured H₂O in close (PDB ID 3MMR)(Ilies et al. 2010)(**A**). This Mn binding domain is inside of the protein and cannot interact with solvent. Prolinase has a similar binuclear motif, but coordinates with the O from PO₄ (PDB ID 3L7G)(Vyas et al. 2010)(**B**). Only H₂O is visible in this structure within 3 Å. SOD coordinates 1 Mn with 1 H₂O in a deep binding pocket (PDB ID 1QNM)(Guan et al. 1998)(**C**). (H₂O within 3-10Å of Mn are shown as smaller red spheres, >10Å are red +)

MntR is distinct from other Mn binding proteins in that its Mn binding motif leaves Mn exposed to interact with the spin lattice (**Figure 4.2**). MntR is meant to bind Mn reversibly, taking shape when enough ambient Mn is present (**Figure 4.2A**). This makes solvent exposure essential for its function. In the MntR structure, Mn coordinates with 3 H₂O molecules with a number of other structured H₂O molecules within a few Å (**Figure 4.2B**). This structure is quite similar to a typical chelated contrast agent like Gd-DOTA where Gd interacts directly with 1 H₂O. The exposed H₂O can exchange energy with the H spin lattice or physically exchange with another molecule of H₂O. The structural similarities between a Gd chelate and MntR suggest a similar function (**Figure 4.2C**).

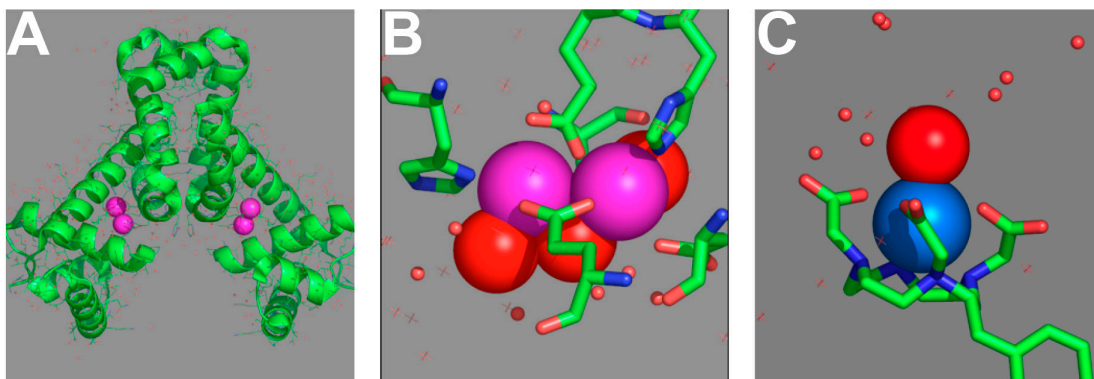


Figure 4.2 The Mn binding motif of MntR is structurally similar to a chelated contrast agent.

Structures of MntR bound to Mn, showing water coordination. The Mn bound MntR dimer binds to 2 Mn ions per subunit (purple) (PDB ID 1ON1)(Golynskiy et al. 2005)(A). The Mn binding motif allows for direct coordination with 3 H₂O molecules (red spheres) with more water nearby (B). Gd-DOTA, a contrast agent coordinates with 1 H₂O, with many other H₂O molecules close by (PDB ID 1NC4)(Cornellie et al. 2003)(C). (H₂O within 3-10Å of Mn are shown as smaller red spheres, >10Å are red +)

While MntR is clearly a chelator of Mn, it is also a protein expressed within the cell. Recent sub cellular imaging studies have shown Mn is very sparse in the cytoplasm and localized in specific organelles (Morello et al. 2008). Using electron microscopy, the unique structure of the nucleus and mitochondrion have been facilitated their identification as organelles that retain Mn. A third organelle in these studies retained the majority of Mn, but could not be identified by its structure alone. Correlative imaging using fluorescence staining and a technique called X-ray fluorescence suggest that this Mn storage organ is the Golgi apparatus (Carmona et al. 2010).

There is no short sequence such as KDEL that will localize a soluble protein specifically to the Golgi, however there are soluble proteins that are resident there, such as Cab45 (Y. Zhang et al. 2009). Also, the C-terminal KDEL sequence will allow a tagged protein to travel out to the *cis*-Golgi before the recognizing its receptor which binds the KDEL sequence and undergoes a conformational change that recruits COP1 vesicle forming proteins and facilitates retrograde transport back to the Golgi (Murshid & Presley 2004). Leveraging the mechanisms that retain proteins in the Golgi could bring MntR to where Mn was being hypothetically localized within the cell.

Given the biological evidence that Mn is sequestered in the Golgi, a strategy for engineering MntR became apparent. MntR was localized to potentially Mn rich regions along the secretory pathway. We hypothesized that fusion to a Golgi resident protein would target MntR to that organelle. This strategy allowed MntR to work in concert with existing Mn biology within the cell, functioning not only as a biological Mn chelator, but as a biological contrast agent.

4.2. RESULTS AND DISCUSSION

Bacterial expression of MntR creates cellular contrast:

For our initial experiments with MntR, we used an existing bacterial expression construct from the lab of John Helman. This construct had already been optimized for maximal expression for crystallization purposes (Glasfeld

et al. 2003). Our initial experiments expressing MntR using an inducible promoter in the BL21 strain of *E. coli* showed 57% contrast compared to uninduced bacteria (**Figure 4.3**). Supplementation of the cells with any amount of Mn only served to raise the background signal in the control cells without significantly altering the signal from the MntR expressing cells. 1.0mM or 25 μ M supplementation of Mn reduced contrast to statistically insignificant levels unless fixed cells were left in PBS for 24h. These data suggest that MntR is binding Mn in the cell, but the effects are not noticeable unless unbound Mn leaves the cell.

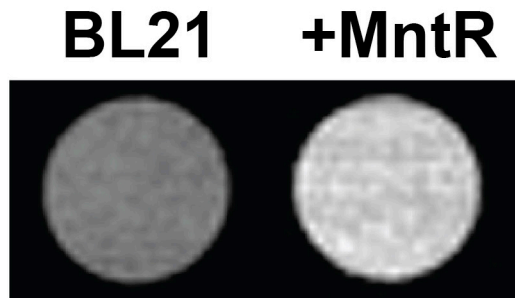


Figure 4.3 Bacterial cells expressing MntR yield significant contrast compared to control cells.

BL21 strain *E. coli* cells with inducible MntR. Addition of IPTG induces expression of the MntR protein (+MntR), causing induced cells to appear brighter in a T₁ weighted image.

MntR does not create contrast *in vivo*, in mammalian cells:

Given all of its attributes, MntR should be the perfect candidate for an expressible Mn based reporter gene for MRI. Early analysis suggested as

much especially in bacteria. This difference was somewhat lessened to 30% contrast in fixed mammalian cells, but given the reduced expression capacity of eukaryotic cells all evidence supported the MntR as a robust T_1 contrast agent. **(Figure 4.4)** Upon scanning live cells however, MntR failed to perform. Cells yielding contrast when fixed in PFA and washed gave no contrast *in vivo*. We hypothesized that this drastic difference between living and fixed cells was due to an active biological process keeping Mn at sufficiently low levels to preclude binding to MntR.

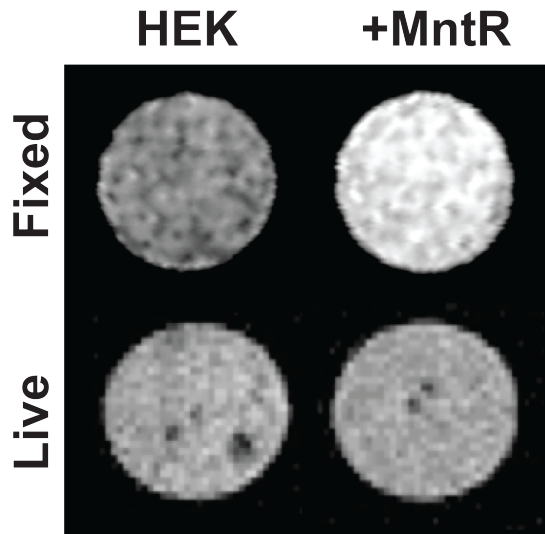


Figure 4.4 MntR induced contrast in Live vs Fixed HEK cells.

When fixed, *ex vivo* HEK cells expressing MntR yield significant contrast compared to controls. There was no apparent contrast when the same cell types were imaged *in vivo*.

Fusion to the Golgi resident protein Cab45 localizes MntR to that organelle:

Without any specific targeting sequences, MntR is translated into the cytoplasm of HEK cells with some leakage into the nucleus through large nuclear pores similar to untargeted eGFP. Coexpression with eGFP showed a homogeneous pattern of colocalization for both proteins throughout the cell (**Figure 4.4A**). MntR fused to the Golgi resident protein Cab45 (CabMntR) successfully colocalized with the Golgi marker 58k (**Figure 5.4B-C**). Cab45 may localize to the Golgi, but EM and ATP2C2 expression data suggested that Mn was specific to cis-Golgi. In the hopes of retaining MntR in this subsection of the Golgi, the Cab45 fusion to MntR was further labeled with a C-terminal KDEL sequence. The Cab45-MntR-KDEL fusion (CabMntRER) colocalized with the Golgi marker similarly to the single fusion (**Figure 4.4C**). Localization here was not likely to be absolute to specific points along a dynamic pathway, and it is possible a larger portion of the MntR fusion was closer to the cis-Golgi. If the KDEL sequence was functioning to maintain the construct in the ER/*cis*-Golgi, the shift was subtle.

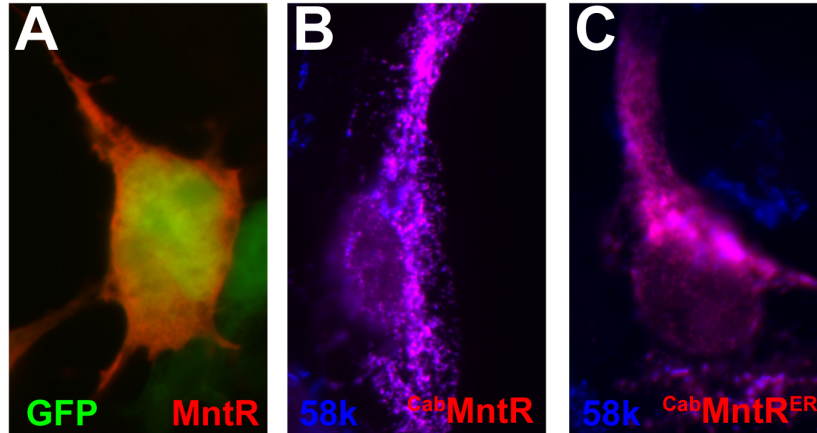


Figure 4.5 MntR fusion proteins localize to the Golgi

Cell staining for MntR with subcellular markers. MntR in absence of localization signals expressed in the cytoplasm similar to GFP (**A**). MntR fused to a Golgi resident protein colocalized with Golgi marker 58k (**B**). Adding an additional ER targeting sequence results in a similar pattern (**C**).

The Cab45-MntR fusion protein improves R_1 in live cells, creating *in vivo* contrast:

Despite the immunocytochemistry data, the double fusion of MntR to Cab45 and the C-terminal KDEL sequence proved to be very important when comparing R_1 relaxation values between all MntR chimeras and control HEK cells (**Figure 4.6**). ^{Cab}MntR did not give any significant contrast when expressed in HEK cells supplemented with 100 μ M Mn. Only the ^{Cab}MntR^{ER} chimera yielded significant R_1 improvements compared to control cells. R_1 gains were a modest 20%, only half of what DMT1 yielded at the given

concentration. Coexpression of $^{Cab}MntR^{ER}$ with DMT1 had a cumulative effect (**Figure 4.6**).

Considering the rapid fall in R_1 in HEK cells post supplementation we hypothesized that MntR expression would improve Mn retention and hence retain R_1 gains well after supplementation (**Figure 4.7**). At 24h post supplementation and wash, the single $^{Cab45}MntR$ construct did give some 10% contrast compared to control cells. The R_1 value of $^{Cab}MntR^{ER}$ did fall similar to HEK control cells, with little absolute difference between the two. The relative difference did improve to 30% in the $^{Cab}MntR^{ER}$ fusion, much better than the t=0h measurements. Even though DMT1 expression did yield some gains in R_1 by itself, similar to previous experiments, coexpression with DMT1 did not yield any further R_1 gains over $^{Cab}MntR^{ER}$ at this time point. It is possible $^{Cab}MntR^{ER}$ binding to available Mn within the Golgi inhibits endogenous mechanisms of Mn retention triggered by saturation.

While the R_1 gains due to $^{Cab}MntR^{ER}$ expression are not as impressive as those due to DMT1, the long term retention offers potential. DMT1 expression in HEK and B16 melanoma cells offered little contrast only a few hours post Mn supplementation and washout. Given the kinetics of Mn uptake and circulation in a living animal MntR might be a better candidate for certain applications where Mn is likely to wash out from cells before imaging is possible.

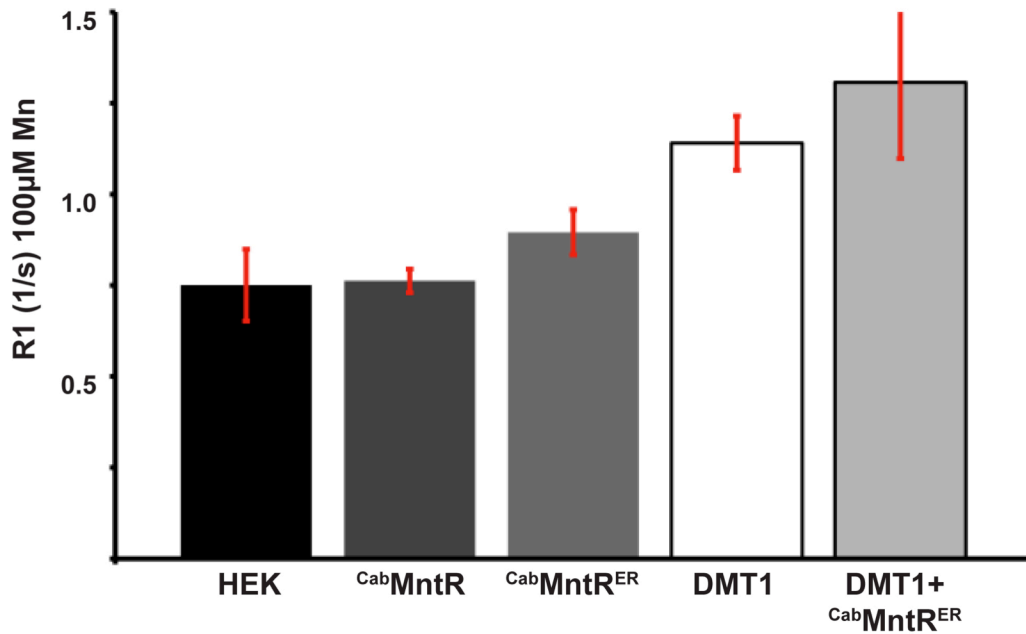


Figure 4.6 R₁ comparison of Mn supplemented HEK cells expressing MntR fusion proteins and DMT1

R₁ measurements of HEK cells supplemented with 100µM Nb and expressing MntR Chimeras and DMT1. CabMntR^{ER} yielded contrast though not at as high a level as DMT1. Coexpression of CabMntR^{ER} with DMT1 increased R₁ but sample variability prevented significance.

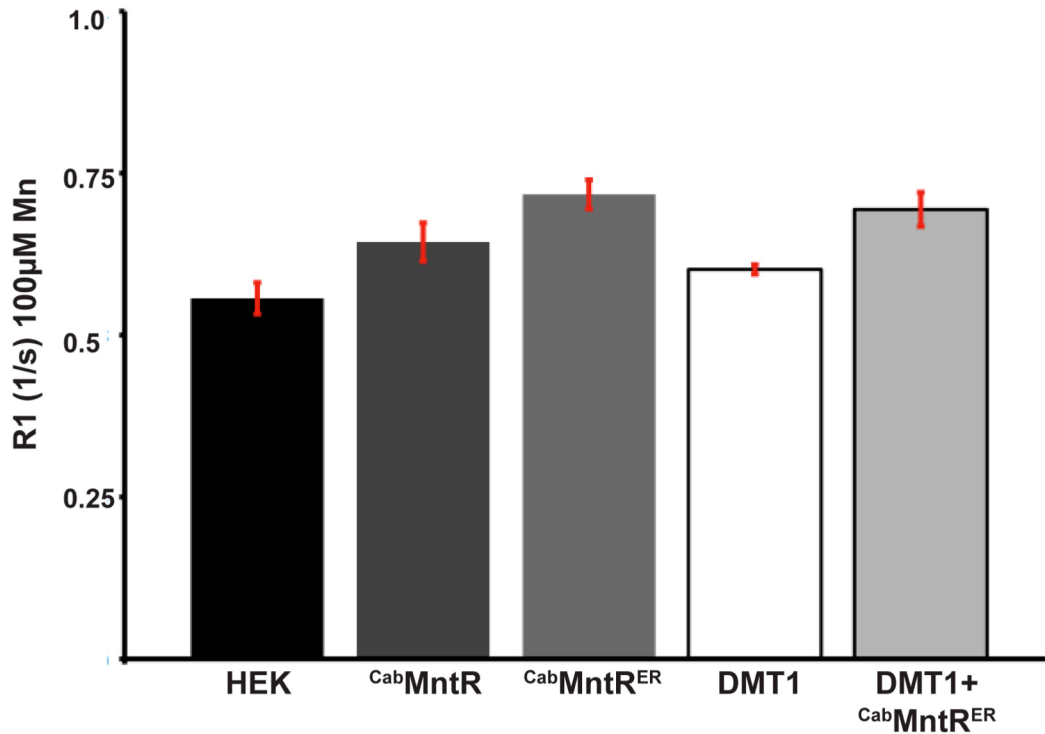


Figure 4.7 R₁ comparison of 24h post Mn supplementation HEK cells expressing MntR fusion proteins and DMT1.

MntR fusions both show improved R₁ at 24h. Significantly better than DMT1 expression alone. Combined expression of DMT1 and CabMntR^{ER} did not give a cumulative effect.

MntR effects R₁ in a pH dependent manner:

An additional, and intriguing feature of MntR is that it shows a structural shift between pH 6.5 and pH 8.5 (Golynskiy et al. 2005). Based on the two available structural models only the pH 6.5 structure exposes Mn to solvent. At pH 8.5 a hydrophobic tyrosine residue occludes the Mn binding site. Furthermore the metal coordination between Mn and MntR changes with pH creating potential, though hard to predict changes in the spin dynamics of

Mn. T_1 based agents are highly dependent upon solvent exposure and sensitive to coordination when chelated, properties that have been exploited to create switchable agents (Louie et al. 2000). Given the structural data, the R_1 effect of MntR should be dependent upon the exposure of Mn to solvent, and thus pH sensitive.

The Golgi is known to be slightly acidic compared to the rest of the cell with a pH near 6.5 (Llopis et al. 1998), but sensitive to pH changes (Rivinoja et al. 2009). In order to induce a pH change in the Golgi, the cell media pH was raised to pH 9.0 after Mn supplementation. In HEK cells this did not significantly reduce R_1 . In cells expressing $^{Ca^{2+}}$ MntR^{ER}, the pH increase reduced R_1 to a level no longer significantly greater than control cells (**Figure 4.8**).

This dynamic structural and pH dependent R_1 shift in MntR has both positive and negative implications. pH changes are a potential artifact in future applications of MntR as a reporter. This is ameliorated by the relative acidity of the Golgi as well as the acidity of many types of pathologies such as tumors. More interestingly the sensitivity of MntR to pH is an excellent starting point for deeper engineering efforts. Mutations could potentially shift or narrow MntR's range of sensitivity to more physiologically tractable conditions. Furthermore, the structural changes could be induced by other conditions such as Ca^{+2} abundance or through interactions with other proteins.

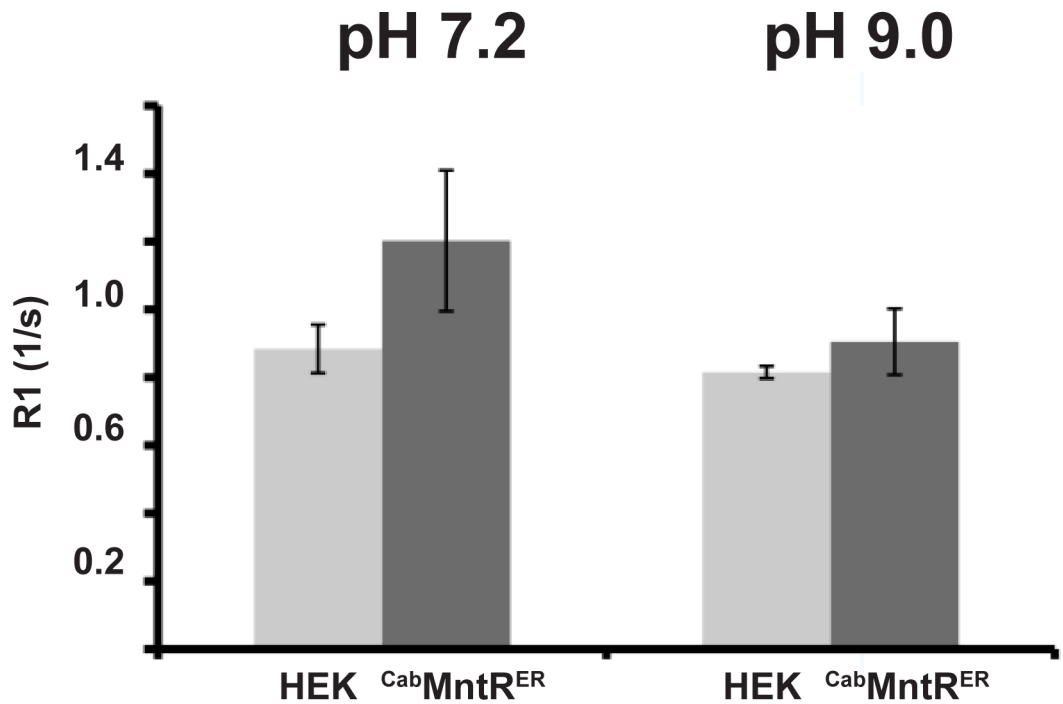


Figure 4.8 R₁ enhancement of ^{Cab}MntR^{ER} is dependent upon pH

HEK and ^{Cab}MntR^{ER} expressing cells supplemented with 300µM Mn for 1h and then placed in control media pH7.2 or alkaline media pH9.0 before relaxometry. ^{Cab}MntR^{ER} improves R₁ with supplementation. Raising the pH extinguishes this improvement without significantly effecting R₁ in control cells.

4.3. CONCLUSIONS

MntR clearly functions as a Mn chelator, but only with significant engineering would it work as a contrast agent *in vivo*. MntR could not function

outside of its cellular context. Instead it only enhanced the function of existing biology to hold Mn in the Golgi for longer. It is possible that this was only because our methods of engineering MntR were limited to generating chimeric fusions. MntR evolved to reversibly bind Mn, but using more specific methods such as directed evolution, it may be possible to make MntR an irreversible binder of Mn, opening up the possibility of cytoplasmic function. This could be important because the Golgi comprises only a small portion of a cell (Murshid & Presley 2004). With such limited volume, achieving enough signal could pose a real challenge *in vivo*. Another reason is that MntR could potentially be used as a sensor, and being limited to the Golgi would greatly limit the applications. Probing genetics using orthogonal reporter systems is highly useful in its own right, however the pH sensitivity of MntR raises the tantalizing potential for it to function as a molecular switch with some deeper engineering efforts.

Interestingly the steps required to functionalize MntR provided a new understanding of Mn in the cell and what we are imaging in MEMRI. These data suggest that in the context of MEMRI, Mn is actually a Golgi stain and marker of the secretory pathway. This view greatly illuminates MRI tract tracing with Mn, which depends on the tendency of Mn to travel down axonal pathways (R G Pautler et al. 1998). While data supports that Mn transport is

an active process the data presented here implies that tract tracing is specifically transport from the Golgi.

4.4. METHODS

Bacterial MntR expression:

MntR was received from the lab of John D Helman in an inducible pET17b vector and transformed into chemically competent BL21 cells. 2mL bacterial cultures were grown overnight in LB under ampicillin selection overnight and used to inoculate 50mL cultures of 2XYT media. Cultures were grown to an optical density (O.D.) of 1.0 and IPTG was added to 1mM to induce MntR expression. Cultures were grown for an additional 2 hours and Mn supplemented cultures were administered Mn at this time. 1mL aliquots were removed from each culture and centrifuged into 1.5 mL tubes. Bacteria was washed in 1mL PBS and fixed for 15m in cold PFA. The bacterial pellets were transferred to NMR pellets immediately and at 24h post fixation. Cells were imaged using a T_1 weighted sequence and contrast was measured as a function of signal intensity.

Constructs:

A mammalian expression optimized version of the MntR gene was synthesized by BioBasic Inc. The original sequence was run through an algorithm that reassigned the codons most compatible for mouse tRNAs and

for the most stable mRNA. A Myc tag was introduced to the C terminus of the protein. The reengineered gene was then put into the pIRES eGFP expression vector and pCDNA3.1 for transfection and into a retroviral construct to generate stable cells and for *in vivo* expression. Retroviral MntR stable cell lines were generated using previously described methods. The reengineered gene was then put into the pCDNA and pIRES eGFP expression vectors each with a CMV promoter driving expression. An ER targeted version of MntR was generated by fusion to known targeting signals. The N-terminal signal sequence and C-terminal KDEL ER retention sequence were derived from the ER chaperone protein BiP and fused to MntR using synthetic PCR with long oligonucleotides of the targeting sequences. A Golgi targeted version of MntR was generated by fusion to the full length Golgi native protein Cab45 and its shortest isoform by alternative splicing. The whole mCherry-Cab45 gene was generated by gene synthesis and included convenient sites for fusion of the Cab45 element to both isoforms into MntR or MnER using restriction site cloning.

Cell Staining:

All constructs were transiently transfected into HEK293T growing on glass slides cells using a chemical reagent. (Trans-IT) Cells were fixed with PFA and immunocytochemistry was conducted using anti-Myc antibody for the integrated Myc tag in all chimeras of MntR (1:500 Abcam), anti-

Calnexin as an ER-marker (1:500 Abcam) and anti-58K as a Golgi marker (1:500 Abcam). Fluorescent Red, Green, and Blue secondary antibodies were used to colabel all markers in each cell. Immunolabeled cells were imaged using an epifluorescence microscope. (Leica)

Stable cell generation:

Transfections of all chimerical versions of MntR in pIRES eGFP were grown for 7 days and sorted using flow cytometry for cells with 10^3 log units of GFP fluorescence. A value equivalent to cells at peak transient expression that also quantifiably matched eGFP expression in each cell line.

Relaxometry:

For contrast measurements, HEK cell lines were cultured in 10cm dishes to 90% confluence. Cells were freed from plates with Trypsin EDTA, washed with PBS. In early experiments cells were fixed with PFA and measured up to 24h post fixation. *In vivo* experiments required the cells to be washed with cold DMEM and measured within 30minutes of removal from culture conditions. Contrast in all cell lines was measured as a function of signal intensity of a T_1 weighted image.

Whole plates of each cell line were cultured in 10cm tissue culture plates until 90% confluent. When supplemented with Mn^{2+} the $MnCl_2$ was added at varying levels 1h before $t=0$ of each experiment. When harvested

cells were freed from the plate using trypsin-EDTA buffer and cells were immediately placed on ice, pipetted into 2mm NMR tubes, and gently pelleted.

5. CONCLUSIONS ON ENGINEERING REPORTER GENES

Summary of candidate reporter proteins:

In this thesis, three different strategies for creating genetically encodable reporters for MRI, and other *in vivo* modalities were explored. The Biotag system utilizes the best biological tag available for use in conjunction with chemical agents ligated onto avidin. This method offers the advantage of utilizing the best molecular probes for any modality, but as a reporter, the system is restricted to the vascular system. DMT1 somewhat overcomes this limitation by utilizing Mn, which is much more widely distributed after administration than avidin. The processivity of DMT1 offers a further advantage, where a single DMT1 molecule could transport thousands of Mn ions across a membrane. This seemingly ideal reporter is hampered *in vivo* by an individual cell's retention of Mn. This element of the DMT1 strategy makes any potential application limited by the particular biology of a given tissue. Finally, MntR offers a solution to the problem of Mn retention by binding Mn within the cell, provided ambient Mn is not prohibitively sparse.

These technologies present a significant advancement over prior art. For MRI, the only other reporter with demonstrated *in vivo*, ferritin, does not offer the same levels of contrast or utility even years after initial publication and subsequent development. The technological advancement is perhaps most significant for UBM, which had no reporter genes prior to Biotag. How

these reporters will ultimately prove useful remains to be seen as they are applied to biological questions. In all the systems however, there are clear areas for improvement and expansion of the technology..

5.1. BIOTAG

Summary of *Ts-Biotag* applications:

Having explored the usefulness of the *Ts-Biotag* animal in multiple models of vascular development (**Chapter 3**), and in response to acute injury signaling (**Appendix 1**), some insights become apparent. The *Ts-Biotag* mouse is a reporter of Tie2 expression alone, yet the expression of Tie2 is actually dependent on multiple external signaling pathways. Therefore looking at expression is a convoluted affair. It is difficult, if not impossible to completely isolate single elements of Tie2 regulation. In the case of wound signaling, Tie2 expression is a convoluted result of peroxides from wound signaling or hypoxia, VEGF from macrophages, systemic Ang2 release, and the genetic circuits that respond to these signals. Individual elements can be blocked by genetic manipulation or drugs, and each artificial perturbation will add to the growing model. This is not a new concept, however in the case of the *Ts-Biotag* mouse all of these future experiments can be conducted *in vivo* requiring less artificial models and resulting data more relevant to clinical research. In addition to having a less artificial model of Tie2 expression, the

ability to conduct *in vivo* experiments with relative ease allows the investigator to consider Tie2 as a dynamic system from the outset.

Tie2 made for an interesting case in that its own signaling could influence expression. Ideally the current reporter of Tie2 expression would be complimented by reporters of Tie2 activation and signaling down each of the three known pathways. There are many strategies for signaling reporters many specifically for receptor tyrosine kinases like Tie2 however none of these systems have ever been implemented in any transgenic animals (W. A. Lim 2010).

Reporter gene assays that probe complex functional genetic responses are common using proteins like GFP or Luciferase, but for MRI these lines of investigation are rare, if not unprecedented. From MR and protein engineering beginnings, the Ts-Biotag mouse is the leading technical edge of vascular and neuroimmunological imaging. The dual success here actually presents a dilemma. Developing a new tool for imaging establishes a substantial body of knowledge in terms of label design and *in vivo* implementation. Changing the technology, even to improve upon it, necessarily obsolesces the previous iteration. Conversely, only a few of the potential pitfalls of the current iteration have been uncovered. Is it then better to immediately improve the current technology or to continue pushing the limits of the current iteration before creating next generation biotag technology? Having constructed a functional

tool, immediate application usually takes precedence. It is apparent that there are a plethora of future experiments involving the Ts-Biotag animal, but from a purely tool and methods development perspective there are clear refinements for the biotag system as a technology.

Improving Biotag:

As previously mentioned *in vivo* imaging is a demanding application, therefore it is important to present the same level of analysis and scrutiny that was applied to Tf/TfR binding and led to this next generation technology. Much like Tf/TfR the 12X biotag system has multiple binding sites for both binding partners. The substantial improvement over Tf/TfR is the increase in available binding sites by 6 fold and an increase in binding affinity at each site by 6 orders of magnitude. It is unlikely that avidin's affinity could be further improved through protein engineering methods, or if such efforts would actually improve labeling.

The biggest and most immediate gains are to be found in the number of tags per unit of protein. Though we found a 12xbiotag construct to be sufficient for our transgenic animals, all data suggests that our *Biotag-BirA* system is amenable to even more biotags per protein molecule with likely proportional improvements in labeling. The reason for these improvements is presumably due to having more sites, but this is probably only partially true. There is no data regarding the structural arrangement of the biotag protein

and the biotag sequence itself appears as a poorly ordered loop in the few available structures, making any predictions ill informed. Regardless, steric hindrances would make it impossible for one whole avidin molecule, let alone the natural avidin tetramer, to bind to each biotin on the biotag protein. It is entirely possible that the biotins could be arranged so as to optimize binding. These sorts of optimization studies, while interesting, would require a combination of structural studies using crystallography and pharmacokinetics to measure maximal binding rate and total occupancy per molecule of biotag protein.

With further regards to structure, the interaction of avidin and biotin, while phenomenal, is otherwise biologically inert. This is a somewhat desirable property when looking specifically for labeling, but there was a downside noticed experimentally. Cells labeled with avidinated probes did not noticeably endocytose the injected agents. While we looked at injected animals up to 24h post injection and saw some continued labeling the pattern of signal had partially shifted. **(Figure 3.7E)** It was unclear whether this was due to cells migrating away or if the molecular probes had been cleaved off and were simply diffusing away. While the long term binding in our *Ts-Biotag* animal could and should be examined in the future, this points to one more area of improvement for next generation biosynthetic labels. Binding that leads to internalization of the targeting agent and molecular probe without

immediate entry into the lysosomal pathway would extend label retention. There is no established method of achieving this effect without using something other than the avidin/biotin interaction such as a biologically active receptor and ligand. One possible method to get avidin binding to induce cellular uptake could come from using a mechanosensitive protein as a scaffold. There are a number of highly sensitive mechanosensitive membrane proteins in pro and eukaryotes including TRP channels (Kung et al., 2010; Arnadóttir and Chalfie, 2010), Integrins (Shakibaei et al. 2008), PSX receptors (Kessler et al. 2011), and AT1 receptors (Mederos y Schnitzler et al. 2011). In this strategy the binding of avidin would have to provide enough tension to stimulate the mechanosensitive protein, inducing uptake. This would work best if avidin was conjugated to a more massive macromolecular complex such as a nanoparticle, liposome or large dendrimer, all of which are currently and increasingly being used in targeted imaging.

Other Biotag transgenic systems:

Tie2 made for an interesting choice in a reporter mouse. In effect *Ts-Biotag* signaling is as much a marker of Ang1/Ang2 signaling as the more abstract phenomenon angiogenesis or inflammation. Although many factors that influence *Ts-Biotag* expression and labeling have been individually identified, the actual cause of any incidence of tagging is convoluted due to the very nature of genetics and all biology. Future iterations of the Biotag

system should focus on systems with either equally well defined mechanisms of regulation such as VEGF, or fundamentally less complex promoters such as HIF1- α .

The ability of the Biotag system to report dynamic processes makes another approach equally attractive. Gene regulation is innately complex, but protein signaling is somewhat farther upstream from a regulatory event and potentially less convoluted in its output. Gene regulation, while a part of the dynamic biology of the vasculature, gives an abstracted view of the more immediate actions of signaling events that are largely protein-protein interactions. Imaging protein signaling has proven to be challenging for research, but another regulatory pathway involved in angiogenesis, Notch, provides a means of looking at the direct effect (Struhl & Adachi 1998). In this pathway, the protein, Notch, when activated by a ligand such as Delta, releases a transcription factor by proteolytic cleavage. Recent work has taken advantage of this very simple signaling pathway to generate a synthetic output of Notch signaling (Sprinzak et al. 2010). Similarly, Notch signaling could trigger Biotag labeling, to give a direct readout of both Notch expression and function *in vivo*. Notch has been implicated in cancer and developmental angiogenesis, and imaging Notch expression alone would be worthwhile for continued work with the Biotag system. The ability to give a direct readout of Notch signaling would take such work much further into exploring the

dynamics the vascular system have immediate application in therapeutic research (Lino et al. 2010).

5.2. DMT1

BBB Permeability of Mn:

Focusing on Mn uptake and retention in the cell still does not account for the many issues that occur in administering Mn to a living animal. Unlike in cells, Mn is not evenly distributed and then washed away just before imaging. Administration of Mn via IP injection occurs over hours. In the brain Mn distribution is unique in that the BBB is not particularly permeable to Mn. Instead, the main route of entry is via the blood CSF barrier. Early work in MEMRI shows the passage of Mn through the ventricles outward into the parenchyma of the brain over 12 hours. Given a tissue with poor Mn retention, it is likely that any difference in Mn uptake by DMT1 expression would have long faded before imaging.

In electroporation experiments this was very likely the case. P0 electroporations often yielded expression in the rostral migratory stream (RMS) of the neonates and was less common in the cortex. Visible contrast however, was only apparent in animals with cortical expression. The cells of the RMS are proximal to the CSF of the ventricle and absorb Mn within the first hours of administration (Aoki et al. 2004). Without a long term Mn retention mechanism, these cells are also the first to lose their Mn to

surrounding tissue. In fact it was only in the P0 electroporations that had expression within the cortex itself that expression based contrast was visible. Without the BBB actively restricting Mn uptake the pattern of contrast in P0 animals would have been very different.

Neonatal animals, in general, have an increased permeability to Mn as evidenced by standard MEMRI methods. In the electroporation experiments all animals were imaged at a young age and in the GL261 tumor model the BBB was disrupted by the presence of the tumor. So far the ability of DMT1 to function with an intact adult BBB or BCB has not been tested in this lab. Whether this will prove to be a challenge for future work remains to be seen.

In general, vascularization is a critical factor in Mn distribution and MEMRI. GL261 tumors, which gave bright contrast at an advanced stage, showed no difference compared to control tumors in the first 2 weeks of growth. Even in these early stage tumors there are disruptions to the BBB, implying that Mn restriction was not a major factor. However GL261 tumors are reportedly avascular at early stages. This again precludes Mn from the DMT1 expressing cells preventing noticeable contrast until functional and Mn permeable vasculature is formed.

In all of these cases, contrast is entirely dependent on the rapid dissemination of Mn throughout the animal. Even in nursing neonates, Mn is available only while it lingers in mammary tissue. The kinetics of this are

unknown, but pups will lose Mn enhanced contrast over days similar to adults, indicating they are no longer being exposed to Mn. Dependence on distribution and uptake kinetics could be overcome by a consistent dose of Mn. Recently this strategy has been employed in MEMRI using subdermal osmotic pumps which deliver a low dose of Mn over days or weeks instead of the single pulse delivered by IP injection (Mok et al. 2012).

Overall, the potential for DMT1 has been established, but it is by no means a finished product the way modern fluorescent reporters are today. This work is only justification for potentially years of further development. It is likely that every application will require its own optimization strategy focusing on the above issues. As we learn more about DMT1 through biochemical and structural studies being conducted by other labs we will gain insights in how to optimize or better control its function as an MRI reporter. For example, DMT1 is reversibly trafficked to and from the surface of the cell in the Fe uptake system where it is associated with transferrin receptor. This implies that there is a reversible switching mechanism, either on DMT1 or TfR that can withdraw functional DMT1 from the surface of the cell. Adapting this system to respond to synthetic stimuli would potentially create contrast on the order of minutes acting as an *in vivo* probe of cell and tissue function at a temporal resolution much faster than a genetic mechanism would allow. Engineering a system to

control DMT1 trafficking reliably will be a challenge, but, with adequate structural and biochemical information, a tractable one.

5.3. MntR

Insights from MntR studies:

Subcellular Mn accumulation has drastic implications for MEMRI contrast. If cells have distinct compartments with very different levels of Mn in them and therefore different T_1 s, MEMRI may not provide an accurate representation of which cell types are actually responsible for Mn uptake and MRI contrast. Cells are generally much smaller than an imaging voxel, but this is not always the case. Purkinje cells extend their dendritic arbors well away from the cell bodies and many axons project far across the brain. The Golgi extends far into these structures, taking up more relative volume there than in the cell bodies.

Another implication of this work is that it expands the model of MEMRI contrast in applications such as axonal tract tracing. This technique is based on the tendency of Mn to travel along axons and to pass along synapses at a rate much faster than diffusion would allow (Robia G Pautler 2004). Transport vesicles have been identified as the mechanism of this phenomenon as evidenced by the effects of transport blockers such as colchicine preventing the spread of MEMRI contrast. The growing evidence that Mn is efficiently

sequestered within the Golgi, the source of all transport vesicles further elucidates this model (Carmona et al. 2010).

Alternative targeting:

The successful strategy of targeting MntR to the Golgi was based on a hypothesis that the protein did not have enough affinity for Mn in the cytoplasm. Only after this assumption could the question of localization of Mn be considered. It is true that Mn is a necessary cofactor in glycosylation enzymes (Ramakrishnan et al. 2006) but these are not the only proteins that use Mn as a cofactor. Superoxide dismutase and Arginase II necessarily bind Mn and are located in the mitochondrion as does nuclear DNA polymerase (Wan et al., 1994; Morris et al., 1997; Garcia-Diaz et al., 2007). These organelles have been identified as having higher levels of Mn in them and the majority of metalloproteins that interact with Mn are in one of these three organelles. It is possible that targeting to the mitochondrion or nucleus would give similar results as ^{Cab}MntR^{ER}

There are a few exceptional Mn binding proteins that suggest alternative targeting would not be successful, one being cytoplasmic Arginase I (Morris et al. 1997). Furthermore it is unclear how metalloproteins in the nucleus and mitochondrion acquire the Mn they need to function. If Mn is so tightly controlled as the MntR data would suggest, these proteins would require an extremely high affinity for Mn. Another possibility is that there is a

transient release of Mn into the cytoplasm. Short term release of Mn through Golgi IP3 gated Ca channels, is a possibility, but the permissivity of these channels to Mn has not been established. Short term exposure to Mn is all that would be necessary as all proteins mentioned above have Mn deeply sequestered from solvent and thus could retain their cofactors even while Mn levels are low. This same sequestration also renders them useless as contrast agents since H exchange is essential for exerting a shift in T_1 . Interestingly, in Golgi resident glycosylation enzymes, sequestration does not occur and Mn associations can be quite transient suggesting an available pool of Mn ions (Ramakrishnan et al. 2006).

Future Work:

$^{Cab}MntR^{ER}$ as it is now may function in cells, but that does not guarantee any *in vivo* success. If the *in vivo* work with DMT1 is any indicator (**Chapter 4**), there will be a substantial drop in contrast given the pharmacological constraints of Mn. Combination with DMT1 holds some promise, but the $^{Cab}MntR^{ER}$ fusion construct is too large to easily accommodate a bicistronic DMT1 in a single vector. One solution to both problems might be to reduce the size of $^{Cab}MntR^{ER}$. The entire Cab45 protein may not be necessary for effective targeting to the Golgi. Looking at Cab45 splice variants there are shorter variants missing their C-terminal ends and a cytoplasmic variant that is missing its N-terminus (Lam et al. 2007),

Alternatively, other Golgi resident proteins may provide better targeting and potentially better contrast. Finding a minimal Golgi targeting sequence alone is potentially useful contribution to research.

Given optimal Golgi targeting what selective advantages would Ca MntR^{ER} give over DMT1? Extended retention of Mn has already been mentioned, but there are specific advantages to a Mn chelating protein as opposed to a Mn transporter. In order to exert an effect over T_1 , Mn must have free exchange with H from water. Early experiments show that MntR exposes and coordinates Mn ions in a pH dependent manner, making the protein a rudimentary pH sensor. Shifting the range of MntR pH sensitivity is quite possible using any number of protein engineering methods already in common practice. Given the flexible structure of MntR, the protein can serve as a scaffold for engineering other sensors as well. The major limitation here is the necessary targeting of MntR to the Golgi limiting the applications to what might be worth sensing in Golgi and the rate of detection. Ca for example, is stored and released from the Golgi in inositol 1,4,5 triphosphate (IP₃) gated signaling. This lipid signaling pathway is critical for activating processes in the neural, endocrine systems (Stewart et al. 2007). Proteins like Cab45 already function as sensors of Ca release from within the Golgi (Y. Zhang et al. 2009). A reporter molecule with similar sensitivity would be useful

for probing IP₃ gated Ca signaling *in vivo*. MntR's potential as a sensor scaffold further highlights the importance alternative targeting within the cell.

5.4. A METAANALYSIS OF ENGINEERING REPORTERS

The three technologies presented in this thesis are the current forefront in *in vivo* reporters outside of fluorescence. Biotag has the distinction of being the first reporter demonstrated for use in UBM. Meanwhile, in the field of MRI only ferritin comes close to DMT1 in terms of utility and implementation *in vivo*. In light of the success of these reporter proteins it is important to review them objectively and ask whether they are application ready technologies, or prototypical proofs of concept intended for further development. Clearly, no technology is ever truly complete and refinements are likely to continue even on established reporters, such as GFP. GFP however, can be readily implemented in a wide variety of applications with no further development. By this rubric, the Biotag system and especially the Ts-Biotag mouse qualify as application ready. Already, the Ts-Biotag mouse is being implemented in models of Tie2 expression that are beyond any original conception of its purpose. Most importantly the Ts-Biotag mouse can be used without intimate knowledge of its design. The Biotag system itself is a more specialized technology, but if further transgenic mice are to be made, generating the constructs and animals will not require the expertise of the original authors. The only area where the Biotag is plainly lacking is the poor choice of Myc epitope tag on the Biotag protein. Integration of a more convenient tag such

as HSV or even a GFP would be preferable before broadly sharing the technology.

DMT1, in its current implementation, is much more prototypical than Biotag. Every current example of *in vivo* contrast came with caveats or only under specific empirically derived conditions. The system is lacking additional technology to compensate for Mn release, or even a clear model of this process to provide a theoretical framework for experimental design. While DMT1 as a reporter may not yet be a robust technology it is still a very useful one. Given the endogenous Mn retention of the brain, DMT1 can be immediately applied to this tissue at neonatal stages when the brain is particularly permeable to Mn, and probably into adulthood, with some optimization of Mn administration. This is still a very limited window, considering the ability of MRI to image a whole animal over its entire natural lifespan. Methods to expand DMT1's utility into tissues that are less amenable to MEMRI should be explored.

Finally there is MntR, which, despite being the system under development the longest, is seemingly the least developed *in vivo* reporter. Really, MntR required more conceptually difficult iterations of development than the other two systems. Biotag started as a mammalian ready system that required a targeting step to be compatible with a cell surface protein, multiplication of biotags to improve signal, and finally development of the

transgenic. Each step was fairly intuitive based on existing theory. DMT1 required even less development. In one step, the protein was placed in a viral vector and tested *in vivo*. MntR had to go from a bacterial protein through mammalian optimization and targeting to an unknown organelle using an untested fusion protein.

In fact, each iteration of MntR had its own potential, but also limitations that precluded *in vivo* imaging as originally conceived. In its first iteration, MntR with its DNA binding function removed made an excellent MRI reporter in bacteria. This is not terribly useful for most brain imaging applications, but could be applied to genetically labeling and tracking pathogenic bacteria in meningitis, or using MntR as a reporter in gut flora to look at the functional genetics of bacteria *in vivo* under normal and pathogenic conditions. In its second iteration as a mammalian codon optimized protein, MntR did not function as an *in vivo* MRI reporter, but it worked quite well in fixed tissue. *Ex vivo* imaging in 3D at 50 μ m or higher resolution is a very useful advancement over previous technologies and could fulfill similar roles as optical coherence tomography and NIR imaging. In its third and present iteration ^{Cab45}MnTR^{KDEL} functions *in vivo*, but should still be considered a prototype for a future optimized reporter, especially in light of MntR's potential as a sensor. At any point however, the utility of the previous iterations of MntR could be explored.

As discussed in preceding chapters, each of these technologies was tested in relevant models to identify areas of development, then reiterated with hypothetical improvements. Recognizing when to begin the next iteration of development proved to be a very challenging aspect of the work. The *Ts-Biotag* mouse was generated almost immediately after multi-tagging proved successful. Ultimately this was the right decision as the *Ts-Biotag* animal did in fact label vasculature and has successfully yielded novel data. While there are changes that could be made to the Biotag system the need was not apparent until data from the *Ts-Biotag* animal was analyzed. Creation of a transgenic mouse began for MntR as well, but this happened before the need for Golgi targeting was identified. This was a premature decision in retrospect, but MntR's failure to create contrast *in vivo* was not immediately recognized. Given the current data, DMT1 is probably ready to be implemented in a transgenic or knock-in animal, but the utility of any transgenic is uncertain until the data is collected on any given tissue. This would suggest that an early transgenic of DMT1 should express in a broad range of tissues, allowing for systemic comparisons of Mn enhancement to a WT mouse. Finally, the *in vivo* trials of MntR have barely begun, but will likely follow an arc similar to DMT1. A virus will be used to express the protein in a tumor cell and ultimately healthy tissue. MntR may be expressed in conjunction with DMT1 though no current data shows a compelling reason to do so.

Looking forward, these technologies present a solid platform for reporter gene imaging *in vivo*. As each system becomes more robust as a technology the work nature of the work changes from the reporters themselves to the systems they were meant to probe. Some initial forays were made in this thesis using the Ts-Biotag animals to explore Tie2 expression in wound healing. This made for an excellent example of what noninvasive *in vivo* imaging can do. What made wound healing an ideal model was timeframe in which the processes observed occur. Initial wound signaling happened over the course of hours, but significant changes occurred over days. For MRI, where image acquisition can take up to two hours and the Ts-Biotag mouse where labeling needs at least several hours to fade, this was ideal. For DMT1 or MntR the timeframe of the biological process being explored will be a critical factor when deciding if and how to implement an MRI reporter. It seems unlikely that MRI could effectively image rapid processes such as Ca⁺⁺ release or to track single cells moving through a tissue or organism. Many signaling pathways such as receptor tyrosine kinases, nuclear hormone receptors and even some G-protein coupled receptors exert an effect over minutes or hours and are thus much more amenable to imaging using MRI.

Probing *in vivo* systems has long been considered technically challenging and specialized realm of research, but the benefits of creating new windows into, formerly invisible, biological processes are obvious. New tools like those

described here are becoming increasingly available, making *in vivo* work less specialized and more accessible to a wider group of investigators. The work presented here, or at least some part of it, will eventually become part of the standard kit for molecular imaging and reporter development will focus on applications beyond our current imagining. Already, functional reporters are being used to probe protein signaling along specific pathways while methods such as Ca^{++} imaging report more generic cellular responses. For every method of probing known phenomenon are a host of other inaccessible pathways such as lipid signaling or nebulous processes such as extra cellular matrix dynamics or proteostasis that are currently too complex to confidently address with *in vivo* methods of visualization. These are the true frontiers of *in vivo* imaging. Problems we cannot even conceptualize currently, but will become the next forefront of technical development in time.

6. THOUGHTS ON THE EPISTEMOLOGICAL NATURE OF THIS THESIS:

A personal and existential question that arose early in this thesis project was, “what kind of research is this?” And more recently, “can a thesis be a technology?” Those questions cannot be answered by just by looking the practical methodologies employed. These epistemological questions require a holistic view of the work. Research, as a concept, is vast and often nebulous, but within what is generally recognized as science today there are distinguishable schools of thought.

Hypothesis driven research is recognized as the foundation of modern science. The scientific method is often taken for granted, but organizing thought into such an effective rubric has literally taken all of human history. By systematically building upon observation and experiment, hypothesis based research has generated a wealth of knowledge. Only very recently, with the advent of computation and digital media, has there been enough of an abundance of data to precipitate the field of informatics. The past decade has seen the rise to prominence of a new philosophy in the form of data driven research. Founded in the genomics revolution, this method is based on the initial collection of large data sets with observations drawn from the subsequent analysis. While sometimes controversial, the many fields of

“omics,” and the subsequent systems biology of analyzing massive biological data sets, could only exist with a theoretical foundation painstakingly crafted from centuries of classical curiosity driven research. The methodologies are similar however in that they are both fundamentally reductionist.

Even though hypothesis based experiments and bioinformatics on large data sets were essential, neither of these approaches describes this particular thesis research. The work presented here, began as a specific engineering challenge, namely, biological contrast. Data was generated as a part of the development process, or from a direct trial of a new construct. This makes the work fundamentally different from a reductionist approach. Instead, the nature of the research could be described as application driven. This is distinct from an engineering project because no theoretical framework was in place to guide the work towards a clearly defined goal. Theoretical models were, instead, empirically generated *ad hoc*, as part of the design process.

Much like data driven research a theoretical foundation was absolutely essential to identifying the application and the direction of development to meet that challenge. This type of research has become quite common in fields like materials science and physics, which have a very strong theoretical basis to support applied disciplines. Much of MRI research has been based on fulfilling specific engineering challenges and development of new contrast mechanisms continues in this vein. In biology, application driven research is

less common, but the field is growing rapidly as synthetic biology becomes more established and funding sources continue to prioritize translational research.

These distinctions are important to better understand differences in philosophy that may run counter to otherwise valid reductionist views. For example, there is no central hypothesis or observation in this work. Biological research without either element could be considered thoughtless and rote, but (I would argue) that this is not the case. Here, the product of the work itself is initially hypothetical with a central assumption that biological contrast could actually be constructed from preceding theory and future experimentation.

Another difference is in the questions raised by the work. There is the famous adage that, good research creates more questions than it answers. That is also true in this case. Only here, the fulfillment of the original challenge directly results in technology with new applications in addition to new questions or observations. Now that a bioengineered contrast is real phenomenon, what are the limits of detectability for any specific application? How can these systems be made switchable or controlled by a biological circuit? Are paramagnetic metals the right platform for any given application? These are as much questions as they are hypothetical constructs to be manifested.

7. APPENDIX 1: *IN VIVO* STUDIES OF TIE2 EXPRESSION USING THE *TS-BIOTAG* MOUSE

7.1. INTRODUCTION

The Biotag reporter system offers genetic control of multimodal, *in vivo* labeling in any cell type directly in contact with the circulatory system. We have only just begun to explore this new technology in the first transgenic animal produced using Biotag under the control of a minimal Tie2 promoter, the *Ts-Biotag* mouse. Our initial experiments with the *Ts-Biotag* mouse provided visible new insights into the expression of Tie2 (**Chapter 3**), even though *Tie2-eGFP* mice have been in use for over a decade (Motoike et al. 2000). For example, expression studies in cell culture have shown Tie2 plays a role in larger blood vessels but no *in vivo*, reporter studies have been published (H. Song et al. 2009). Upregulation of Tie2 in large blood vessels was immediately apparent using NIR imaging and remains one of the easiest structures to image (**Figure 3.10**). The ready availability of the *Ts-Biotag* mice and the substantial resources required to them warranted a deeper exploration into models of Tie2 expression. By taking full advantage of *in vivo* and minimally invasive imaging we are likely to insights into the biology of Tie2 that were formerly obscured by the only available imaging modality.

The Receptor Tyrosine Kinase Tie2:

Tie2 is a receptor tyrosine kinase that has several known ligands, the angiopoetins (Ang) 1-4. Context dependent Tie2 signaling along either the ERK1/2 or Akt pathway is involved in formation of new vasculature and in the stabilization and maturation of vessels respectively (Fukuhara et al. 2009). **(Figure 8.1)** Tie2 has also been shown to play a key role in NF-kappaB regulated inflammation and endotoxic shock via direct interaction with ABIN-2 (Hughes et al. 2003). Several reporter mice have been generated using the Tie2 promoter, “bashed” down to its minimal functional elements (Ts), for developmental studies, and more recently cancer angiogenesis (Motoike et al., 2000; Minami et al., 2003). The use of Tie2 reporter mice has been mostly limited to histology, especially in adult models, with limited multi-photon *in vivo* microscopy (Dunphy et al. 2009). There are no targeted agents commercially available to study Tie2 *in vivo* for several reasons. Angiopoetins form complex oligomers which could be disrupted by chemical labeling, and Tie2 is largely associated either with the extracellular matrix (ECM) during vessel formation, or *trans*-associated with other Tie2 receptors in areas of cell-cell contact, limiting the amount of Tie2 accessible from the vasculature (Fukuhara et al. 2009). These factors present challenges to fluorescent reporters or protein targeting, and therefore made Tie2 an excellent choice for our hybrid system.

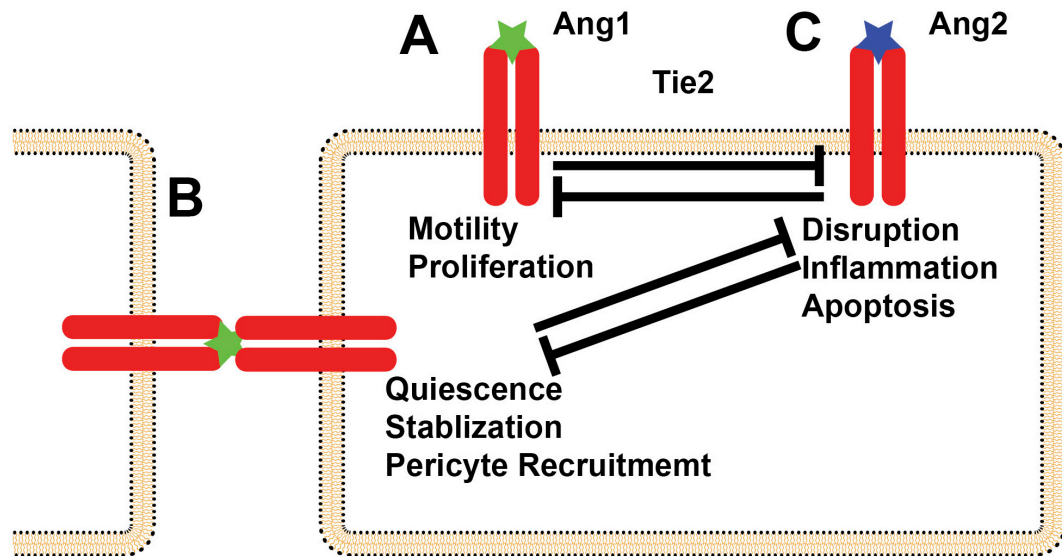


Figure 7.1 Overview of Tie2 Protein Signaling:

Tie2 has 3 known signaling pathways. Ang1 binding Tie2 in *cis* signaling stimulates motility and proliferation (A). Ang1 signaling across Tie2 in *trans* causes quiescence and vascular maturation by recruitment of pericytes and other stabilizing vascular cells (B). Ang2 signaling disrupts cell cell contacts destabilizing vascular cells and at high enough levels can cause apoptosis (C).

Tie2 Expression:

The Tie2 protein and its ligands, the angiopoetins, make for a particularly interesting model of study because, within their already complex signaling pathways, they show feedback regulation of their own expression. (Figure 7.2) This means that looking at expression of Tie2 is, at least partially, looking at Angiopoetin/Tie2 signaling. In the simplest model of angiopoetin based regulation of Tie2, Ang2 blocks expression. In contrast, Ang1 upregulates Tie2 and itself in a self amplifying feedback loop. This self amplification allows for a rapid response to stimuli, necessary in a system prone to acute changes such as injury. In this limited model we expect to see Ang1 and 2 working

against each other to keep Tie2 expression low until a rapid response is needed.

The model of Ang1 and 2 regulated expression of Tie2 gains complexity by at least 2 additional factors. First Tie2 and Ang1 are both upregulated by a hypoxia responsive transcription factor NERF2 (Christensen et al. 2002). This upregulation is completely independent of Ang2 and allows for a dominant response to hypoxia regardless of other regulation. Also, Ang1 will not cause any upregulation if the Tie2 proteins are interacting in *trans* with one another. In cell culture experiments motile cells localize Ang1/Tie2 opposite of the leading edge of motility (Fukuhara et al. 2009). However in confluent cells Tie2/Ang1 localizes at all cell-cell contacts forming a *trans* signaling complex. In this quorum-like condition, any cells that would otherwise be responsive to the proliferative and motility inducing effects of Ang1 signaling are already in close contact. Rather than proliferate, the cells become quiescent and begin to recruit support cells like pericytes and slow muscle (Takata et al. 2011). To add to the complexity, VEGF or even Ang2 can potentially disrupt the Ang1 *trans* complex, changing its mode of signaling.

Ultimately, all of this complex regulation should predict when to expect *Ts-Biotag* expression and labeling. This also suggests that not seeing *Ts-Biotag* labeling can be just as important to a study of the vasculature. For example, the previous data shows that *Ts-Biotag* labeling was detectable only

under conditions associated with angiogenesis, but this has deeper implications when the larger role of Tie2 regulation in biology is considered. The exception to minimal basal levels of Tie2 expression is in the brain. Why this is the case is not well understood, but has implications for the nature of the BBB and its permeability. Here tight junctions, facilitated by pericytes, recruited by Ang1 *trans* signaling, are important, but must be rapidly disrupted during an immune response where white blood cells must pass out of the vasculature (Takata et al. 2011). Understanding the BBB and what causes it to become permeable, is an area of active research and points to a broader field of applications for the Ts-Biotag mouse.

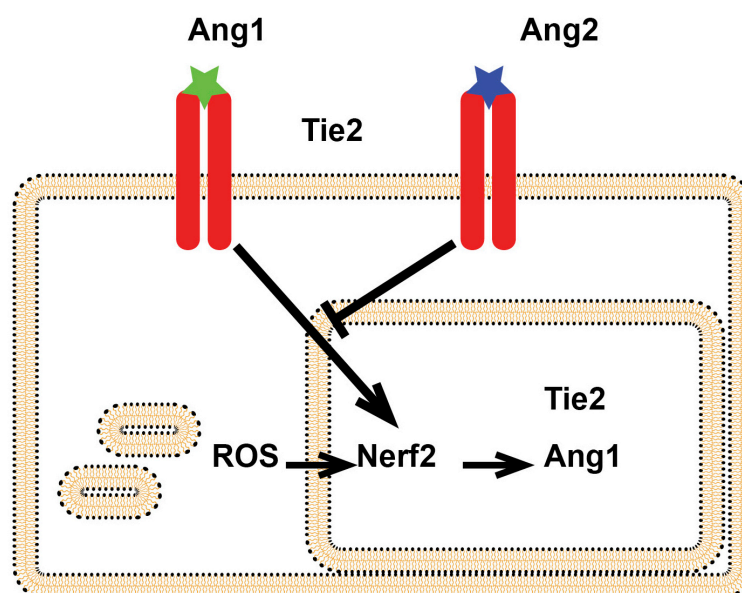


Figure 7.2 Tie2 Expression:

Tie2 expression is mediated by buildup of reactive oxidative species (ROS) from mitochondrion, often a result of hypoxia. This activates the transcription factor Nerf2 to upregulate Ang1 and Tie2. Ang1 signaling also upregulates Tie2 and Ang1 through a non-elucidated pathway.

7.2. RESULTS AND DISCUSSION

Adult expression of Tie2:

We originally chose matrigel as a generic adult model of angiogenesis to demonstrate that labeling occurs during normal vascular development and is not dependent upon pathologies such as a tumor. The distinction is important, since tumors have a wide range of mechanisms for recruiting vasculature. As evidenced in the matrigel model, a VEGF gradient is all that is required for angiogenesis and upregulation of Tie2 in the surrounding endothelial tissue. VEGF signaling is not the actual cause of *Ts-Biotag* labeling however, as it does not directly upregulate Tie2. Instead VEGF leads to disruption of the extra cellular matrix (ECM) and cell-cell contacts therefore activating Ang1 driven upregulation of Tie2. Tie2 expression should only last in the presence of VEGF and indeed, imaging the matrigel two weeks after implantation shows thoroughly vascularized tissue with mature blood vessels and very low levels of *Ts-Biotag* labeling (**Figure 3.11C**). Non-VEGF mediated disruptions of the ECM could also lead to a similar upregulation of Tie2 and hence *Ts-Biotag* labeling. ECM disruptions can be caused by the

action of Matrix-metallo-proteases MMPs and are a hallmark of cancer metastasis and immune cell invasion (Bourboulia & Stetler-Stevenson 2010). This may be difficult to differentiate from VEGF activity, but suggests that *Ts-Biotag* would be detectable even in many tumors (**Figure 7.3**), regardless of what mechanism drives angiogenesis. Conversely, tissues like musculature actively express Ang2 and have very low levels of Tie2 in their vasculature perhaps to counteract frequent hypoxia, yet develop vasculature normally (Minami et al. 2003). It then must be possible for tumors to stimulate angiogenesis with minimal or no Tie2 signaling or expression.

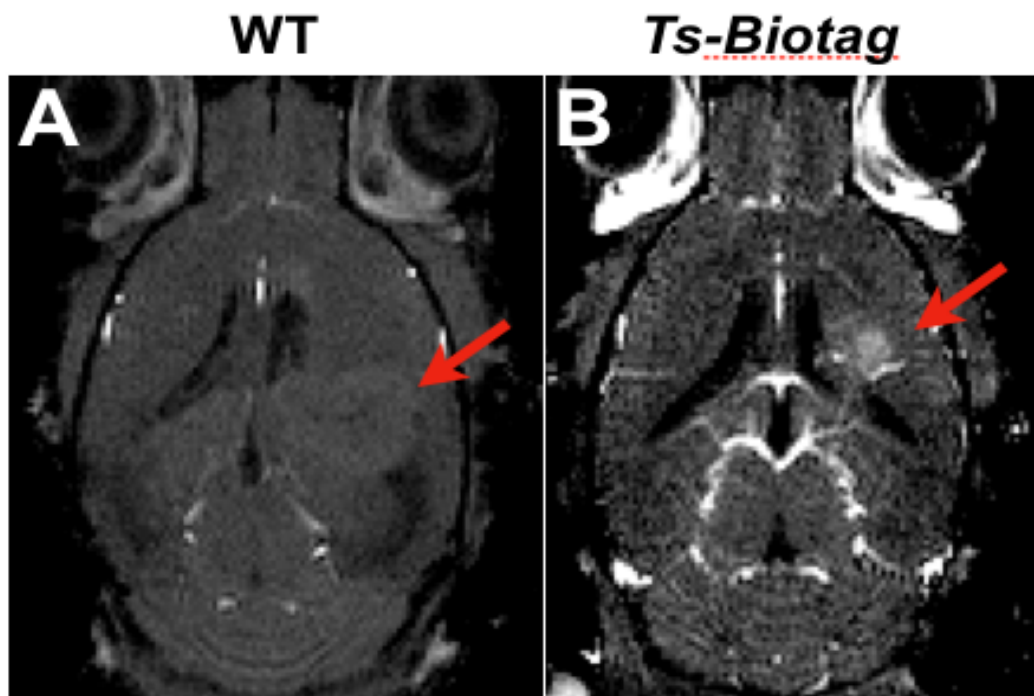


Figure 7.3 Ts-Biotag labeling in tumors

GL261 tumors (red arrows) in WT (A) and *Ts-Biotag* (B) mice injected with Av-DTPA-Gd. There is minimal labeling in the WT animal (A) while labeling is

apparent within and around the *Ts-Biotag* tumor. Vascular labeling is also detectable in large blood vessels distal to the tumor.

Ts-Biotag outside of the vasculature:

The majority of work on Tie2 thus far has focused on expression in vascular endothelial cells (**Chapter 3**). Early experiments also showed *Ts-Biotag* labeling in cells just outside of the vasculature in embryos (**Figure 8.4**). These cells must have some interaction with the vascular endothelium or else they would not be labeled, but they were not vascular endothelial cells. Iba1 staining showed *Ts-Biotag* positive cells to be of the myeloid lineage, most likely macrophages. Similarly Tie2-GFP animals were identified as having GFP+ macrophages during development and during tumor angiogenesis (Pucci et al., 2009; Lewis et al., 2007). This represents a specific class of macrophage, as in adult animals neither unperturbed macrophages nor microglia stain positive for Tie2 nor show activation of any *Ts* linked reporter protein (De Palma & Naldini 2011). Tie2 expressing macrophages (TEMs) appear to be directly involved in angiogenesis developmentally and in tumors. This is not entirely surprising as Tie2 is expressed in erythropoietic cells and there are marrow derived endothelial cells that play an active role in angiogenesis (De Palma et al., 2005; Ribatti, 2009). The mechanism of these macrophages in developmental or tumor angiogenesis is unclear, however there is precedent of myeloid cells as positive and negative regulators angiogenesis. Retinal myeloid cells for

example have been shown to use intercellular signaling to render vascular endothelial cells insensitive to VEGF by inducing the upregulating the inactive VEGF receptor Flt1 via a non canonical Wnt pathway (Stefater III et al. 2011). The mechanisms of TEMs and angiogenesis are just beginning to be described, as researchers have only recently identified Tie2 in macrophages, however macrophages have been previously shown to secrete VEGF in response to H₂O₂ signaling (M. Cho et al. 2001). This finding begged the development of a model system that could show Tie2 expression at the intersection of the vascular and the immune system.

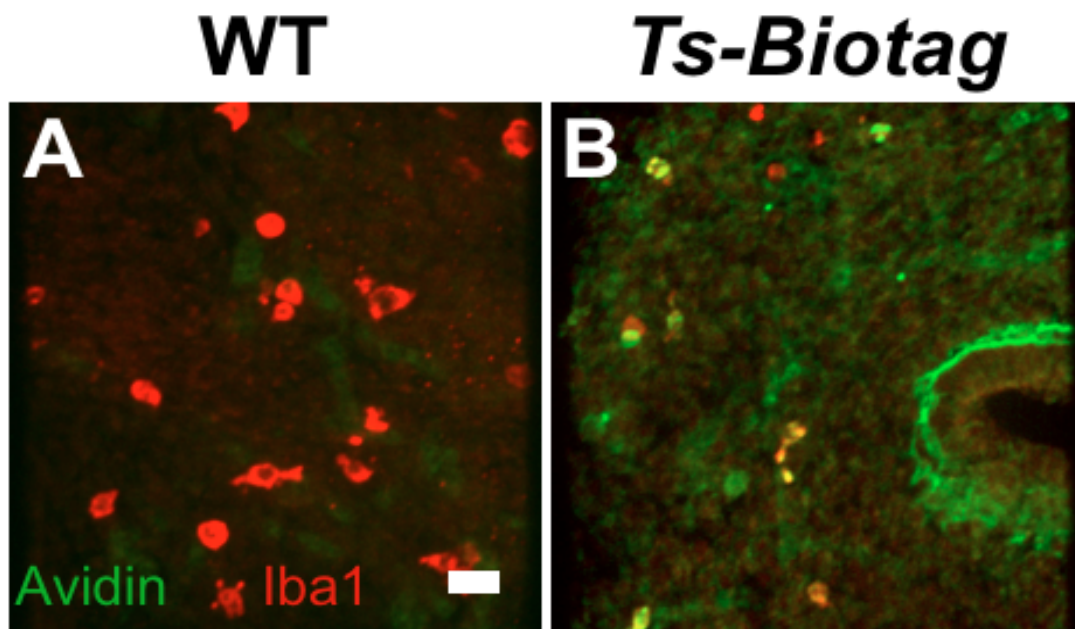


Figure 7.4 Avidin-FITC and Iba1 staining in E11.5 embryos

Using confocal microscopy on sections from E11.5 embryos low levels of Avidin-FITC are detectable (A). Costaining with Iba1 shows no colocalization between the two markers. In Ts-Biotag animals considerably more staining is visible with colocalization of signal with most Iba1+ cells (B)

Ts-Biotag animals in a model of acute injury:

An obvious example of disruption of the ECM is an acute physical injury. These disruptions could shift quiescent *trans* Ang1 signaling to the activating *cis* pathway as cell junctions are cleaved. Physical disruption and Ang1 would not necessarily be the sole factor in this case however. Peroxide signaling plays a key role in wound signaling, both recruiting leukocytes and stimulating VEGF release in macrophages (Niethammer et al., 2009; Cho et al., 2001). In addition to wound signaling, peroxides, from buildup of ROS, are an integral part of hypoxia signaling, a Tie2 transcriptional activator (Majmundar et al., 2010; Christensen et al. 2002) (**Figure 7.2**). These layers of amplifying Tie2 upregulation could lead to a drastic and rapid response to injury.

Returning to the vascular system, angiopoetins have been shown to play a role in vascular remodeling in wound recovery (Eun Kim et al. 2007), specifically improved wound healing and angiogenesis by Ang1 (C.-H. Cho et al. 2006). Considering the critical need for a vascular response in injury and wound healing and the apparent role of Tie2 in macrophages developing models of acute injury using the Ts-Biotag seemed worthwhile to explore.

***Ts-Biotag* mice effectively label the vasculature during response to a peripheral injury:**

In this very simple model of injury, ears were punched, similar to a standard genotyping protocol, after which the mice were injected with SAv-680 and imaged with NIR at defined time points between 0-2 days (**Figure 7.5**; N=3 for each genotype / time point combination). WT mice showed some enhancement of SAv-680 signal around the wound immediately after injury (**Figure 7.5A**), likely due to bleeding, which was close to background levels by day 1 (**Figure 7.5C**) and completely gone by day 2 (**Figure 7.5E**). Activation of the Ts element and labeling in the Ts-Biotag mice was rapid, showing strong labeling immediately after injury (**Figure 7.5B**), which persisted for approximately 2 days (**Figure 7.5D, F**). This labeling was brightest around the wound complementing previous work showing the angiopoetins effects on wound response (Eun Kim et al. 2007). Labeling was also obvious in vessels feeding into the injury site (**Figure 7.5B, D**), similar to the labeling observed in the VEGF-matrigel model. This long range response has not been shown before, demonstrating the ability of the Ts-Biotag mice to reveal new information about the dynamics of vascular gene expression in response to injury. This long range signaling also occurs upstream of the wound, in feeding blood vessels. This would imply that the signaling molecule

that activates Tie2 expression is being transported retrograde along blood vessels, either cell to cell or along the lymphatic system

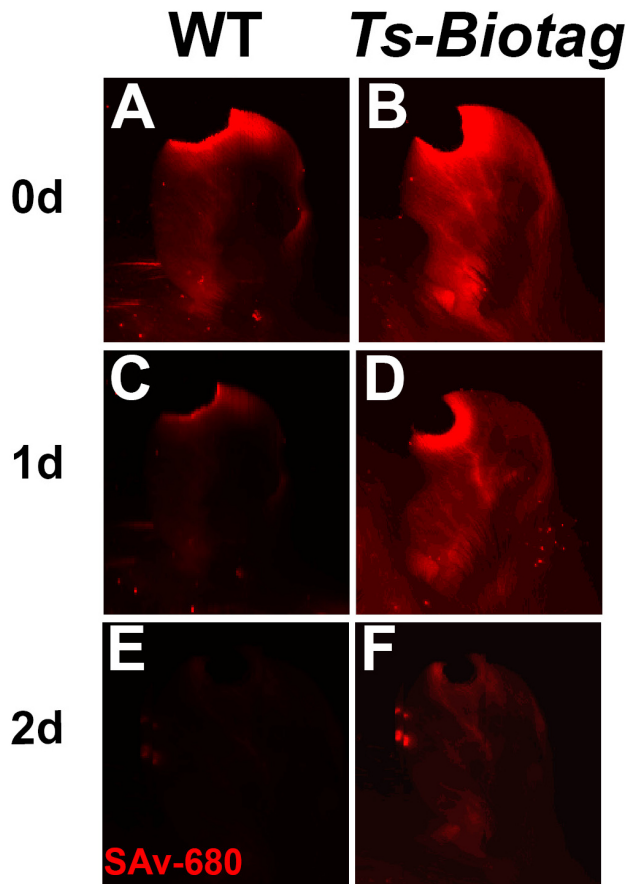


Figure 7.5 NIR scans of ear injury response

Ears of WT and Ts-Biotag mice were punched and imaged with NIR on days 0 (0d), 1 (1d) and 2 (2d) after wounding. Separate groups of mice (N=3 WT; and N=3 Ts-Biotag) were imaged each day, all mice being imaged 30 minutes after tail vein injection of SAv-680. On day 0, some signal was visible in WT mice, possibly due to bleeding (**A**), while Ts-Biotag mice showed much brighter labeling around the injury site and in numerous blood vessels in the ear (**B**). On day 1 there was minimal labeling in WT animals (**C**), while the SAv-680 labeling was still strong in Ts-Biotag mice, both around the injury site and in blood vessels feeding into the wound (**D**). On day 2, there was no labeling in any WT mice (**E**), while SAv-680 labeling was low but still detectable in Ts-Biotag mice (**F**).

The cryo model of neuroinjury:

The cryo-injury model is a simple method of creating a nonspecific lesion in the brain without physically opening the skull. Causing a lesion with a cryoprobe in a WT mouse caused edema, but did retain Av-DTPA-Gd (**Figure 7.6B,A**). Labeling around the area of lesion was visible in Ts-Biotag animals though superficial compared to edema, indicating some cell type within the area of edema was specifically labeling with Av-DTPA-Gd (**Figure 7.6C,D**).

This labeling did not appear to be vascular based purely on the morphology of the area of contrast. While labeling around the lesion area continued to the 48h time point it also broadened to well outside of the area of edema, appearing to label most of the larger blood vessels of the brain. This distal labeling was similar to the ear punch but distinct in that there was a 48h delay between injury and vascular labeling which did not happen in the ear injury.

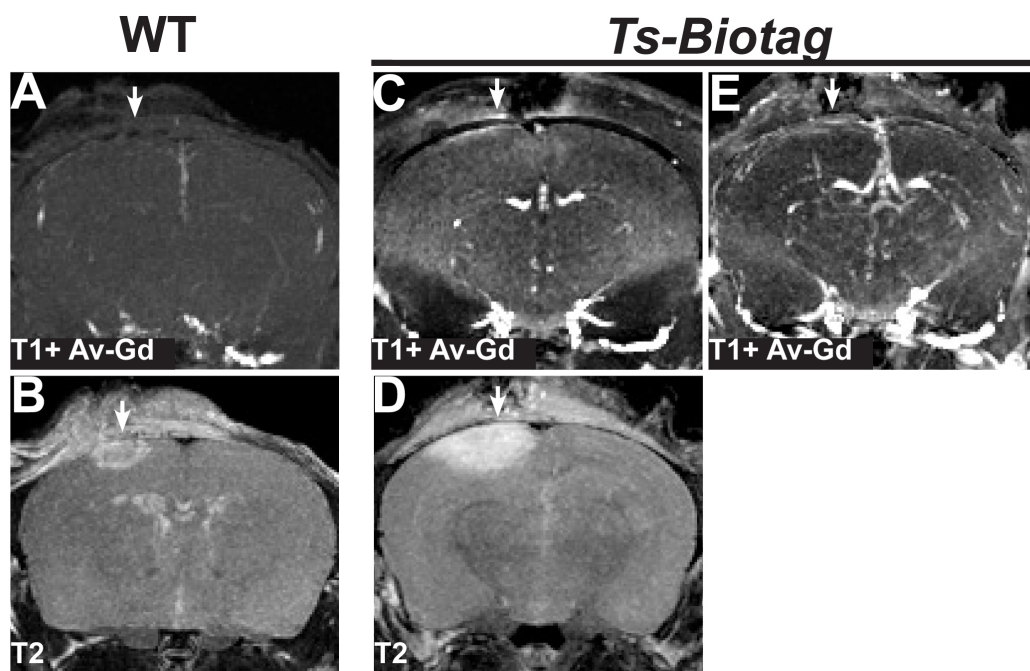


Figure 7.6 MRI of cryo-injury in WT and Ts-Biotag mice

Mice were lesioned through the skull using a -70°C cryoprobe. 24h post lesion animals were injected with Avidin-DTPA-Gd for T_1 weighted imaging. (A, C) WT animals showed no significant labeling in a contrast enhanced T_1 weighted image. (A) T_2 imaging revealed a small lesion around the area of the applied probe. (B, D) (white arrow) In the Ts-Biotag animals a small area of enhancement was visible around the lesioned area. (C) (white arrow) The area of labeling did match with edema around the lesion visible in a T_2 image, (D) (white arrow) but was not morphologically typical of vasculature. 48h post lesion, the labeling changed to a distinctly vascular pattern throughout the brain. (E)

7.3. CONCLUSIONS

These preliminary studies do not provide any mechanistic information about Tie2, but highlight phenomenon worth further study. The 2 day delay between injury and broad upregulation of Tie2 is the best example, though there is a clear line of exploration. In the early stages of brain injury there is an activation of microglia and recruitment of myeloid lineage leukocytes mediated by toll like receptors (TLR) and tumor necrosis factor (TNF- α) (Downes & Crack 2010). Immune cell invasion is only possible via Ang2 signaling, and in Ang2 knockout animals, immune cells cannot leave the vasculature (Fiedler et al. 2006). Based on these data Ang2 and Tie2 have been implicated as key elements of local and systemic inflammation (Li et al. 2012). Ang2 signaling is most likely mechanism of reduced Tie2 expression, and could account for the delay of Tie2 expression seen experimentally in this model of neuroinjury.

This work only touches the surface of the largely unexplored dynamics of Tie2 and Ang1/2 signaling. This tantalizing glimpse of Tie2 expression and its dynamic response is due largely to the *in vivo* imaging capability of the Ts-Biotag animal. Simply having the option of *in vivo* imaging allows the investigator to think freely in terms of dynamic *in vivo* behavior. The current body of work on Tie2 is severely lacking these insights, coming mainly from cell culture and fixed sample immunohistochemistry. Further experimentation

must necessarily use such techniques, however they can now be complemented with dynamic monitoring of at least one aspect of this complex signaling system.

8. APPENDIX 2: ANALYSIS OF Mn UPTAKE AND EXCRETION BY T₁ RELAXOMETRY

8.1. INTRODUCTION

Development of an Mn based reporter required a deeper understanding of Mn in cells, particularly in light of the transient nature of the Mn induced changes to T₁ in cells (**Chapter 4**). A method was developed to measure T₁ quickly in cells, but also serves as an analog for Mn (**Chapter 4.5**). This is significant because, formerly, Mn could only be measured accurately using radioactive tracers (M. D. Garrick et al. 2006). T₁ mapping and analysis of R₁ serves as a quantitative assay for Mn retention in cells and allows us to create models of cellular Mn dynamics. A rapid and inexpensive means to measure relative Mn levels in cells would be useful for further studies of Mn as a contrast agent, in its role as a toxin (J. A. Roth & M. D. Garrick 2003), or even as a therapeutic agent for bacterial pathogens (Mukhopadhyay & Linstedt 2012)

8.2. RESULTS AND DISCUSSION

R₁ is an analog measurement of the first order kinetic rate:

The relaxation rate, or R₁, is a convenient unit for analyzing contrast agents due to a linear relationship between R₁ and concentration of an agent. Measuring cells is different from a measure of R₁ in a pure solution of contrast

agent in water because the cellular environment has second order effects on Mn and R_1 . In practice R_1 retains linear dependence upon Mn concentration, [Mn], within cells, yet R_1 values never matched that of an Mn solution of equivalent concentration (**Figure 3.2**). Cells are not highly permeable to Mn and DMT1 is capable of taking up metal ions against a gradient. The amount of Mn in the cells, and any correlative measurement thereof has deeper connotations.

The cell takes up Mn at an unknown rate (K_{up}) but also excretes Mn (K_{ex}). Transfer across a membrane into a finite space follows Michelis-Menton first order kinetics wherein rate of transfer is dependent on both K and relative Mn concentration or:

$$\frac{-d[Mn]}{dt} = K[Mn]$$

Mn accumulation in HEK cells and in tissue follow first order kinetics, approaching a maximum after 20m of exposure (Garrick et al., 2006; Bai et al., 2008). This means that after an hour of incubation, Mn is flowing in and out of the cells at equilibrium. Regardless of the difference between K_{up} and K_{ex} , a point of saturation will be reached where the concentration gradient [Mn] will allow excretion to match uptake. An R_1 measurement is then proportional and analogous to the steady state of K and [Mn].

$$R_1 \propto |K_{up}[Mn]| = |K_{ex}[Mn]|$$

For most experimental purposes relative R_1 s are compared within the same cell type allowing us to ignore K along with cellular influences on R_1

Understanding that the rate constants K_{up} and K_{ex} are inherent in any R_1 measurement gives an insight into cellular Mn biology.

R_1 measurements assay cell type dependent Mn retention:

A clear area for further research in Mn biology using R_1 analysis is the mechanism of Mn retention in cells. HEK, B16 and GL261 cells all had distinct Mn retention profiles as determined by R_1 measurements. (**Figure 8.1**) Looking at the 3 kinetic profiles, B16 cells have the poorest Mn retention. Losing all supplemented Mn in a matter of hours. HEK cells are only slightly better, but consistently supplemented cells do retain some R_1 improvements up to 24h after return to unsupplemented media. Both cell types show a rapid drop in R_1 that follows a first order kinetic curve. This was contrasted by the GL261 cells, which had a slower fall in R_1 which followed a rate limited, or logistic curve. In terms of contrast, the loss of R_1 improvement over time is well offset by the respective R_1 drop in control cells. These kinetic differences were readily apparent *in vivo* comparing B16 and GL261 tumors (**Figures 3.3, 4.4**). The B16-DMT1 strain had a clearly superior R_1 improvement in culture, yet the average *in vivo* contrast was a fraction of this value (**Figure 3.3A,C**). Meanwhile GL261 cells demonstrated *in vivo* contrast much closer to their maximum potential as measured in cells (**Figure 3.4A,C**). These differences are also readily apparent in MEMRI. Some tissues retain Mn for several days while others lose their Mn based contrast in a matter of hours.

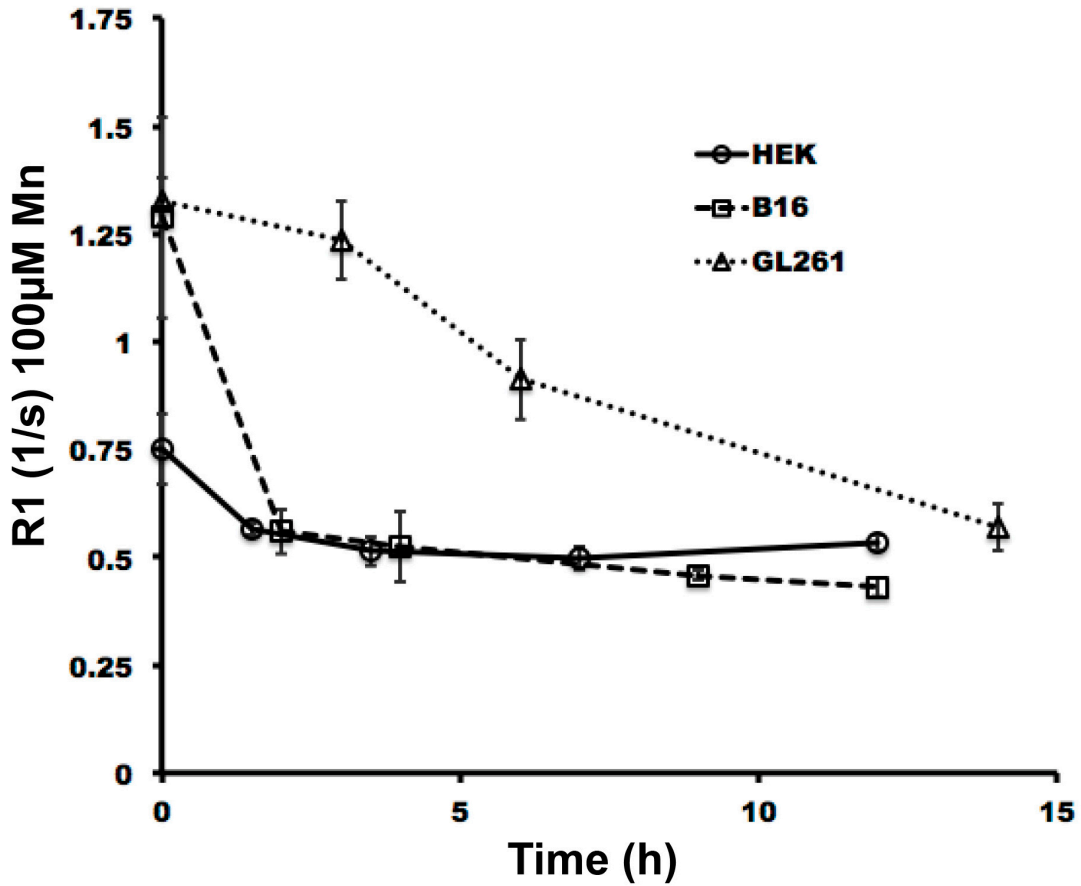


Figure 8.1 Retention of R_1 as an analog for Mn in multiple cell types.

3 cell types were supplemented for 1h with Mn then washed with fresh media. R_1 was measured over time. HEK cells (Solid line) quickly lose R_1 after removal of Mn from the media. B16 cell behave similarly despite having much higher initial R_1 gains. Both cell types follow first order kinetics for transfer across a membrane. GL261 cells slowly reduce in R_1 after supplementation and follows a logistic rather than first order trajectory.

Distinct timecourse R_1 profiles reflect different mechanisms of Mn excretion:

The curve followed by B16 and HEK cells in timecourse studies are very similar to studies of Mn uptake. The first order kinetic curve is indicative of a single membrane with a mechanism of transfer with at rate K . This suggests that both cell types have some mechanism for release of Mn across the plasma membrane, either by a channel or transporter.

The GL261 cells follow a very different profile. Logistic curves are common in self-limiting biological systems such as tumor growth or population dynamics. In these systems they account for the rate limiting step. It is impossible to say what the mechanism of Mn release from GL261 cells is base solely on these measurements, but the curve indicates something more complex than passage across a single membrane. Based on the studies with MntR (**Chapter 5**), it seems possible that excretion could be mediated via the golgi either via the secretory pathway or by a slow release into the cytoplasm followed by transfer across the plasma membrane.

R_1 Relaxivity measurements show a nonlinear relationship between DMT1 expression and Mn uptake:

In development of DMT1, multiple lines of HEK-DMT1 overexpressing and knockdown cells were produced with varying levels of DMT1 that could be compared quantitatively (**Figure 3.2A**). Naturally higher relatives levels of

DMT1 produced more uptake of Mn, in a manner that was also concentration dependent (**Figure 3.2C**). Plotting the R_1 of these cell lines against the supplementation conditions and taking the slope gives an effective R_1 enhancement per unit of extracellular Mn $[Mn_{ex}]$, or the cellular relaxivity, a value independent of $[Mn]$. This makes cellular relaxivity proportional to the uptake or excretion rate alone.

$$R = \frac{R_1}{[Mn_{ex}]} \propto K$$

Because either value of K is different for every cell type, it is only valid to compare otherwise identical cells and is approximate considering that low levels of DMT1 expression are not particularly linear. Comparing the relaxivities of each HEK cell line against their relative expression levels, $[DMT1]$, provides insights into the function and regulation of the DMT1 protein. Naturally, higher levels of DMT1 improve relaxivity, but plotting relaxivity against $[DMT1]$ in HEK cells does not yield a linear increase per unit of DMT1. Instead the logistic curve, indicates some regulatory factor is present.

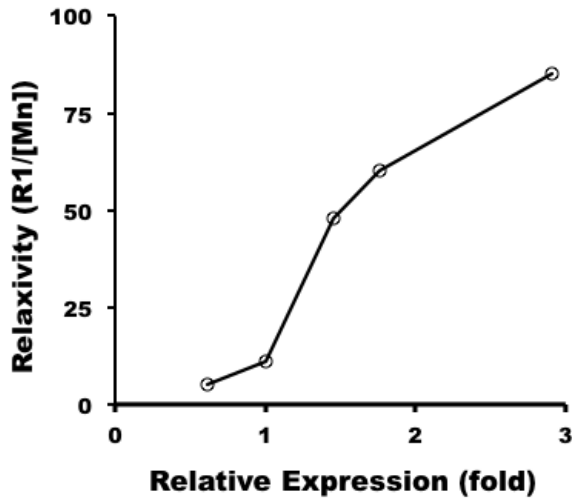


Figure 8.2 Plot of relaxivity vs relative DMT1 expression

Varying amounts of DMT1 do not yield a linear increase in R_1 per unit of Mn. Expression was measured in naïve HEK293 cells (1 fold), in an shRNA knockdown line and 3 overexpressing cell lines.

R_1 Relaxivity is an analog for the Mn uptake rate by DMT1:

Looking deeper into logistic curves, these complex systems are described by the following formula:

$$\frac{dP}{dt} = rP \left(1 - \frac{P}{K} \right)$$

In this equation, P is the population or value subject to limitation, t is time and r is rate of change in P . K is a rate limiting factor also called the carrying capacity. In a population or tumor model K would represent the rate of loss of resources that feed growth. The slope of the logistic curve can

describe the Mn uptake system in terms of relaxivity, per unit of protein, [DMT1].

$$\frac{dK_{up}}{d[DMT1]} = K_{reg}K_{up} \left(1 - \frac{K_{up}}{K_{lim}}\right)$$

In this model, the element subject to limitation is the rate of Mn uptake, K_{up} , r represents the maximum rate of regulation on the uptake rate, K_{reg} . While K is defined as the limiter of DMT1, K_{lim} , The values of K_{reg} and K_{lim} are not obvious preventing this model from being applied quantitatively. The model does however help to isolate the mechanisms of Mn uptake regulation distinct from the [Mn] kinetics.

Endogenously, DMT1 expression is regulated by Fe responsive elements (IREs) however in this system expression is under an artificial promoter that is not subject to transcriptional or post transcriptional regulation. Furthermore, experimentally we are measuring protein levels of DMT1 leaving pretranslational regulation out entirely. One possibility is that the DMT1 protein itself is subject to regulation. In this model, DMT1 would only work at optimal efficiency ($K_{avg} = K_{max}$) alone or when positively regulated by a binding partner. At high levels of expression, a negative regulatory factor, or lack of a positive regulator would reduce efficiency ($K_{avg} < K_{max}$) either by allosteric regulation or by removing the DMT1 from the plasma membrane entirely. The variable C terminus of DMT1 supports the allosteric model. Within this region there are known and probably regulatory mechanisms to DMT1's function and

distribution to the plasma membrane. This is further supported by comparative studies. MnTH is a SLC2A transporter in E.coli. Phylogenic analysis indicates that this protein not a prokaryotic precursor, but actually descended from mammalian DMT1 via horizontal gene transfer. Interestingly, this version of DMT1 lacks its entire C terminus and 12th transmembrane helix, further suggesting that this domain of the protein is not involved in Mn transport and likely serves a purpose not relevant to bacteria such as regulation by mammalian factors.

If allosteric regulation the case, the specific regulatory regions on DMT1 could be identified and deleted, improving the rate of relaxivity change per unit of DMT1 expressed by increasing K_{avg} . The allosteric regulation model suggests a high K_{reg} . The rate of change in K_{up} would be subject to the kinetics of protein-protein or protein-small molecule interactions. K_{lim} would then describe the dynamic range of control on DMT1, with a high K_{lim} suggesting that DMT1 transport could be completely shut off.

An alternative model is that DMT1, and hence K_{up} , is not regulated at all. Instead the excretion rate is being regulated shifting the equilibrium of the initial R_1 measurements changing relaxivity. There is very little evidence to support this model, it can be tested experimentally by manipulating expression of the ATP2C2 pump, or slowing down the secretory pathway along the Golgi.

8.3. CONCLUSION

These R_1 analyses give us some intriguing insights into the dynamic regulators of Mn uptake and excretion, and provide a framework for experimentation. Measuring R_1 in cells expressing DMT1 mutants, or other proteins that effect transport, makes for an efficient means to study Mn transport without using mass spectroscopy or radioactive Mn^{54} . These methods can be extended to ask further questions about secretion, however. Just as MEMRI can be used to examine rates of axonal transport in neurons (Robia G Pautler 2004), measuring Mn release could also be used to assay the rate of the secretory pathway in some cell types. Drugs or gene expression that effect secretion rate via the Golgi can be would effect the rate of Mn excretion and hence effecting the profile of R_1 measurements over time. *In vitro* studies of cellular relaxometry may be of limited utility, but they provide a starting point for more sophisticated *in vivo* studies. These same methods can be applied to a living mouse in conjunction with MEMRI to assay secretion rates in neuronal or exocrine tissue. Our improved understanding of the biology behind MEMRI allows us to look ever deeper into other kinds of biology, *in vivo* and noninvasively.

9. BIBLIOGRAPHY

- Agarwal, A., Saraf, S., Asthana, A., Gupta, U., Gajbhiye, V., and Jain, N.K. (2008). Ligand based dendritic systems for tumor targeting. *Int J Pharm* 350, 3–13.
- Aisen, P. (2004). Transferrin receptor 1. *The International Journal of Biochemistry & Cell Biology* 36, 2137–2143.
- Akhtar, N., Dickerson, E.B., and Auerbach, R. (2002). The sponge/Matrigel angiogenesis assay. *Angiogenesis* 5, 75–80.
- Aoki, I., Wu, Y.-J.L., Silva, A.C., Lynch, R.M., and Koretsky, A.P. (2004). In vivo detection of neuroarchitecture in the rodent brain using manganese-enhanced MRI. *NeuroImage* 22, 1046–1059.
- Arnadóttir, J., and Chalfie, M. (2010). Eukaryotic mechanosensitive channels. *Annu Rev Biophys* 39, 111–137.
- Artemov, D. (2003). Molecular magnetic resonance imaging with targeted contrast agents. *J. Cell. Biochem* 90, 518–524.
- Asahara, H., Nameki, N., and Hasegawa, T. (1998). In vitro selection of RNAs aminoacylated by Escherichia coli leucyl-tRNA synthetase. *J. Mol. Biol* 283, 605–618.
- Aschner, M., Vrana, K.E., and Zheng, W. (1999). Manganese uptake and distribution in the central nervous system (CNS). *NeuroToxicology* 20, 173–180.
- Bagautdinov, B., Matsuura, Y., Bagautdinova, S., and Kunishima, N. (2008). Protein Biotinylation Visualized by a Complex Structure of Biotin Protein Ligase with a Substrate. *Journal of Biological Chemistry* 283, 14739–14750.
- Bai, S.P., Lu, L., Luo, X.G., and Liu, B. (2008). Kinetics of Manganese Absorption in Ligated Small Intestinal Segments of Broilers. *Poult Sci* 87, 2596–2604.
- Beckett, D., Kovaleva, E., and Schatz, P.J. (1999). A minimal peptide substrate in biotin holoenzyme synthetase-catalyzed biotinylation. *Protein Sci* 8, 921–929.

- Berrios-Otero, C.A., Nieman, B.J., Parasoglou, P., and Turnbull, D.H. (2011). In utero phenotyping of mouse embryonic vasculature with MRI. *Magn Reson Med*.
- Berrios-Otero, C.A., Wadghiri, Y.Z., Nieman, B.J., Joyner, A.L., and Turnbull, D.H. (2009). Three-dimensional micro-MRI analysis of cerebral artery development in mouse embryos. *Magn Reson Med* *62*, 1431–1439.
- Bloch, F. (1953). *The principle of nuclear induction* (Kungl. boktryckeriet P.A. Norstedt & söner).
- Bock, N.A., Paiva, F.F., and Silva, A.C. (2008). Fractionated manganese-enhanced MRI. *NMR Biomed* *21*, 473–478.
- Bourboulia, D., and Stetler-Stevenson, W.G. (2010). Matrix metalloproteinases (MMPs) and tissue inhibitors of metalloproteinases (TIMPs): Positive and negative regulators in tumor cell adhesion. *Semin. Cancer Biol* *20*, 161–168.
- Boutin, C., Diestel, S., Desoeuvre, A., Tiveron, M.-C., and Cremer, H. (2008). Efficient in vivo electroporation of the postnatal rodent forebrain. *PLoS ONE* *3*, e1883.
- Bulte, J.W.M., and Kraitchman, D.L. (2004). Iron oxide MR contrast agents for molecular and cellular imaging. *NMR in Biomedicine* *17*, 484–499.
- Carmona, A., Devès, G., Roudeau, S., Cloetens, P., Bohic, S., and Ortega, R. (2010). Manganese Accumulates within Golgi Apparatus in Dopaminergic Cells as Revealed by Synchrotron X-ray Fluorescence Nanoimaging. *ACS Chemical Neuroscience* *1*, 194–203.
- Cha, S., Johnson, G., Wadghiri, Y.Z., Jin, O., Babb, J., Zagzag, D., and Turnbull, D.H. (2003). Dynamic, contrast-enhanced perfusion MRI in mouse gliomas: Correlation with histopathology. *Magn. Reson. Med.* *49*, 848–855.
- Chae, J.K., Kim, I., Lim, S.T., Chung, M.J., Kim, W.H., Kim, H.G., Ko, J.K., and Koh, G.Y. (2000). Coadministration of angiopoietin-1 and vascular endothelial growth factor enhances collateral vascularization. *Arterioscler. Thromb. Vasc. Biol* *20*, 2573–2578.
- Chalfie, M., Tu, Y., Euskirchen, G., Ward, W.W., and Prasher, D.C. (1994). Green fluorescent protein as a marker for gene expression. *Science* *263*, 802–805.

- Chasteen, N.D., and Harrison, P.M. (1999). Mineralization in ferritin: an efficient means of iron storage. *J. Struct. Biol* 126, 182–194.
- Cheng, Y., Zak, O., Aisen, P., Harrison, S.C., and Walz, T. (2004). Structure of the Human Transferrin Receptor-Transferrin Complex. *Cell* 116, 565–576.
- Cho, C.-H., Sung, H.-K., Kim, K.-T., Cheon, H.G., Oh, G.T., Hong, H.J., Yoo, O.-J., and Koh, G.Y. (2006). COMP-angiopoietin-1 promotes wound healing through enhanced angiogenesis, lymphangiogenesis, and blood flow in a diabetic mouse model. *Proc Natl Acad Sci U S A* 103, 4946–4951.
- Cho, M., Hunt, T.K., and Hussain, M.Z. (2001). Hydrogen peroxide stimulates macrophage vascular endothelial growth factor release. *American Journal of Physiology - Heart and Circulatory Physiology* 280, H2357 - H2363.
- Christensen, R.A., Fujikawa, K., Madore, R., Oettgen, P., and Varticovski, L. (2002). NERF2, a member of the Ets family of transcription factors, is increased in response to hypoxia and angiopoietin-1: A potential mechanism for Tie2 regulation during hypoxia. *J. Cell. Biochem.* 85, 505–515.
- Cohen, B., Ziv, K., Plaks, V., Israely, T., Kalchenko, V., Harmelin, A., Benjamin, L.E., and Neeman, M. (2007). MRI detection of transcriptional regulation of gene expression in transgenic mice. *Nat Med* 13, 498–503.
- Corsi, B., Cozzi, A., Arosio, P., Drysdale, J., Santambrogio, P., Campanella, A., Biasotto, G., Albertini, A., and Levi, S. (2002). Human mitochondrial ferritin expressed in HeLa cells incorporates iron and affects cellular iron metabolism. *J. Biol. Chem* 277, 22430–22437.
- Crossgrove, J.S., and Yokel, R.A. (2004). Manganese Distribution Across the Blood-Brain Barrier III: The Divalent Metal Transporter-1 is not the Major Mechanism Mediating Brain Manganese Uptake. *NeuroToxicology* 25, 451–460.
- Crossgrove, J.S., and Yokel, R.A. (2005). Manganese distribution across the blood-brain barrier: IV. Evidence for brain influx through store-operated calcium channels. *NeuroToxicology* 26, 297–307.

- Deans, A.E., Wadghiri, Y.Z., Bernas, L.M., Yu, X., Rutt, B.K., and Turnbull, D.H. (2006). Cellular MRI contrast via coexpression of transferrin receptor and ferritin. *Magn. Reson. Med.* *56*, 51–59.
- Deans, A.E., Wadghiri, Y.Z., Berrios-Otero, C.A., and Turnbull, D.H. (2008). Mn enhancement and respiratory gating for in utero MRI of the embryonic mouse central nervous system. *Magn Reson Med* *59*, 1320–1328.
- Devasahayam, G., Burke, D.J., and Sturgill, T.W. (2007). Golgi manganese transport is required for rapamycin signaling in *Saccharomyces cerevisiae*. *Genetics* *177*, 231–238.
- Diamandis, E.P., and Christopoulos, T.K. (1991). The biotin-(strept)avidin system: principles and applications in biotechnology. *Clin. Chem* *37*, 625–636.
- Dorr, A.E., Lerch, J.P., Spring, S., Kabani, N., and Henkelman, R.M. (2008). High resolution three-dimensional brain atlas using an average magnetic resonance image of 40 adult C57Bl/6J mice. *Neuroimage* *42*, 60–69.
- Downes, C.E., and Crack, P.J. (2010). Neural injury following stroke: are Toll-like receptors the link between the immune system and the CNS? *British Journal of Pharmacology* no-no.
- Dunphy, M.P.S., Entenberg, D., Toledo-Crow, R., and Larson, S.M. (2009). In vivo microcartography and subcellular imaging of tumor angiogenesis: a novel platform for translational angiogenesis research. *Microvasc. Res* *78*, 51–56.
- Ellegala, D.B., Leong-Poi, H., Carpenter, J.E., Klivanov, A.L., Kaul, S., Shaffrey, M.E., Sklenar, J., and Lindner, J.R. (2003). Imaging tumor angiogenesis with contrast ultrasound and microbubbles targeted to alpha(v)beta3. *Circulation* *108*, 336–341.
- Eun Kim, K., Cho, C.-H., Kim, H.-Z., Baluk, P., McDonald, D.M., and Young Koh, G. (2007). In Vivo Actions of Angiopoietins on Quiescent and Remodeling Blood and Lymphatic Vessels in Mouse Airways and Skin. *Arterioscler Thromb Vasc Biol* *27*, 564–570.

- Fernández-Suárez, M., Chen, T.S., and Ting, A.Y. (2008). Protein-protein interaction detection in vitro and in cells by proximity biotinylation. *J. Am. Chem. Soc* *130*, 9251–9253.
- Ferrara, N., and Kerbel, R.S. (2005). Angiogenesis as a therapeutic target. *Nature* *438*, 967–974.
- Fiedler, U., Reiss, Y., Scharpfenecker, M., Grunow, V., Koidl, S., Thurston, G., Gale, N.W., Witzenrath, M., Rosseau, S., Suttorp, N., et al. (2006). Angiopoietin-2 sensitizes endothelial cells to TNF-[alpha] and has a crucial role in the induction of inflammation. *Nat Med* *12*, 235–239.
- Fox, M., and Rabi, I.I. (1935). On the nuclear moments of lithium, potassium and sodium (Lancaster press inc.).
- Fraser, S.T., Hadjantonakis, A.-K., Sahr, K.E., Willey, S., Kelly, O.G., Jones, E.A.V., Dickinson, M.E., and Baron, M.H. (2005). Using a histone yellow fluorescent protein fusion for tagging and tracking endothelial cells in ES cells and mice. *Genesis* *42*, 162–171.
- Fukuhara, S., Sako, K., Noda, K., Nagao, K., Miura, K., and Mochizuki, N. (2009). Tie2 is tied at the cell-cell contacts and to extracellular matrix by Angiopoietin-1. *Exp Mol Med* *41*, 133–139.
- Gaiano, N., Kohtz, J.D., Turnbull, D.H., and Fishell, G. (1999). A method for rapid gain-of-function studies in the mouse embryonic nervous system. *Nat Neurosci* *2*, 812–819.
- Gamble, J.R., Drew, J., Trezise, L., Underwood, A., Parsons, M., Kasminkas, L., Rudge, J., Yancopoulos, G., and Vadas, M.A. (2000). Angiopoietin-1 Is an Antipermeability and Anti-Inflammatory Agent In Vitro and Targets Cell Junctions. *Circ Res* *87*, 603–607.
- Garcia-Diaz, M., Bebenek, K., Krahn, J.M., Pedersen, L.C., and Kunkel, T.A. (2007). Role of the catalytic metal during polymerization by DNA polymerase lambda. *DNA Repair (Amst.)* *6*, 1333–1340.
- Garrick, M.D., Kuo, H.-C., Vargas, F., Singleton, S., Zhao, L., Smith, J.J., Paradkar, P., Roth, J.A., and Garrick, L.M. (2006). Comparison of mammalian cell lines expressing distinct isoforms of divalent metal transporter 1 in a tetracycline-regulated fashion. *Biochem. J.* *398*, 539.

- Genove, G., DeMarco, U., Xu, H., Goins, W.F., and Ahrens, E.T. (2005). A new transgene reporter for in vivo magnetic resonance imaging. *Nat Med* *11*, 450–454.
- Gervais, L., Claret, S., Januschke, J., Roth, S., and Guichet, A. (2008). PIP5K-dependent production of PIP2 sustains microtubule organization to establish polarized transport in the *Drosophila* oocyte. *Development* *135*, 3829–3838.
- Gilad, A.A., McMahon, M.T., Walczak, P., Winnard, P.T., Raman, V., van Laarhoven, H.W.M., Skoglund, C.M., Bulte, J.W.M., and van Zijl, P.C.M. (2007a). Artificial reporter gene providing MRI contrast based on proton exchange. *Nat Biotech* *25*, 217–219.
- Gilad, A.A., Winnard, P.T., Jr, van Zijl, P.C.M., and Bulte, J.W.M. (2007b). Developing MR reporter genes: promises and pitfalls. *NMR Biomed* *20*, 275–290.
- Glasfeld, A., Guedon, E., Helmann, J.D., and Brennan, R.G. (2003). Structure of the manganese-bound manganese transport regulator of *Bacillus subtilis*. *Nat. Struct. Biol* *10*, 652–657.
- Goldhawk, D.E., Lemaire, C., McCreary, C.R., McGirr, R., Dhanvantari, S., Thompson, R.T., Figueredo, R., Koropatnick, J., Foster, P., and Prato, F.S. (2009). Magnetic resonance imaging of cells overexpressing MagA, an endogenous contrast agent for live cell imaging. *Mol Imaging* *8*, 129–139.
- Golynskiy, M.V., Davis, T.C., Helmann, J.D., and Cohen, S.M. (2005). Metal-induced structural organization and stabilization of the metalloregulatory protein MntR. *Biochemistry* *44*, 3380–3389.
- Guan, Y., Hickey, M.J., Borgstahl, G.E., Hallewell, R.A., Lepock, J.R., O'Connor, D., Hsieh, Y., Nick, H.S., Silverman, D.N., and Tainer, J.A. (1998). Crystal structure of Y34F mutant human mitochondrial manganese superoxide dismutase and the functional role of tyrosine 34. *Biochemistry* *37*, 4722–4730.
- Haacke, E. (1999). *Magnetic resonance imaging: physical principles and sequence design* (New York: J. Wiley & Sons).
- Hielscher, A.H. (2005). Optical tomographic imaging of small animals. *Curr. Opin. Biotechnol* *16*, 79–88.

- Hilderbrand, S.A., and Weissleder, R. (2010). Near-infrared fluorescence: application to in vivo molecular imaging. *Curr Opin Chem Biol* 14, 71–79.
- Hughes, D.P., Marron, M.B., and Brindle, N.P.J. (2003). The antiinflammatory endothelial tyrosine kinase Tie2 interacts with a novel nuclear factor-kappaB inhibitor ABIN-2. *Circ. Res* 92, 630–636.
- Ilies, M., Di Costanzo, L., North, M.L., Scott, J.A., and Christianson, D.W. (2010). 2-aminoimidazole amino acids as inhibitors of the binuclear manganese metalloenzyme human arginase I. *J. Med. Chem* 53, 4266–4276.
- Iordanova, B., Robison, C.S., and Ahrens, E.T. (2010a). Design and characterization of a chimeric ferritin with enhanced iron loading and transverse NMR relaxation rate. *J. Biol. Inorg. Chem* 15, 957–965.
- Iordanova, B., Robison, C.S., and Ahrens, E.T. (2010b). Design and characterization of a chimeric ferritin with enhanced iron loading and transverse NMR relaxation rate. *J Biol Inorg Chem* 15, 957–965.
- Irie, S., and Tavassoli, M. (1987). Transferrin-mediated cellular iron uptake. *Am. J. Med. Sci* 293, 103–111.
- Johnson, E., Cascio, D., Sawaya, M.R., Gingery, M., and Schröder, I. (2005). Crystal structures of a tetrahedral open pore ferritin from the hyperthermophilic archaeon *Archaeoglobus fulgidus*. *Structure* 13, 637–648.
- Kessler, S., Clauss, W.G., and Fronius, M. (2011). Laminar shear stress modulates the activity of heterologously expressed P2X(4) receptors. *Biochim. Biophys. Acta* 1808, 2488–2495.
- Kliegman, J.I., Griner, S.L., Helmann, J.D., Brennan, R.G., and Glasfeld, A. (2006). Structural basis for the metal-selective activation of the manganese transport regulator of *Bacillus subtilis*. *Biochemistry* 45, 3493–3505.
- Krajewski, W.W., Collins, R., Holmberg-Schiavone, L., Jones, T.A., Karlberg, T., and Mowbray, S.L. (2008). Crystal structures of mammalian glutamine synthetases illustrate substrate-induced conformational changes and provide opportunities for drug and herbicide design. *J. Mol. Biol* 375, 217–228.

- Krause, W. (2002). *Contrast Agents I: Magnetic Resonance Imaging* (Berlin: Springer).
- Kung, C., Martinac, B., and Sukharev, S. (2010). Mechanosensitive channels in microbes. *Annu. Rev. Microbiol* *64*, 313–329.
- Laitinen, O.H., Nordlund, H.R., Hytönen, V.P., and Kulomaa, M.S. (2007). Brave new (strept)avidins in biotechnology. *Trends Biotechnol* *25*, 269–277.
- Lam, P.P.L., Hyvärinen, K., Kauppi, M., Cosen-Binker, L., Laitinen, S., Keränen, S., Gaisano, H.Y., and Olkkonen, V.M. (2007). A cytosolic splice variant of Cab45 interacts with Munc18b and impacts on amylase secretion by pancreatic acini. *Mol. Biol. Cell* *18*, 2473–2480.
- Lam-Yuk-Tseung, S., and Gros, P. (2006). Distinct targeting and recycling properties of two isoforms of the iron transporter DMT1 (NRAMP2, Slc11A2). *Biochemistry* *45*, 2294–2301.
- Larina, I.V., Shen, W., Kelly, O.G., Hadjantonakis, A.-K., Baron, M.H., and Dickinson, M.E. (2009). A membrane associated mCherry fluorescent reporter line for studying vascular remodeling and cardiac function during murine embryonic development. *Anat Rec (Hoboken)* *292*, 333–341.
- Lauterbur, P.C. (1973). Image Formation by Induced Local Interactions: Examples Employing Nuclear Magnetic Resonance. *Nature* *242*, 190–191.
- De León-Rodríguez, L.M., Lubag, A., Udugamasooriya, D.G., Proneth, B., Brekken, R.A., Sun, X., Kodadek, T., and Dean Sherry, A. (2010). MRI detection of VEGFR2 in vivo using a low molecular weight peptoid-(Gd)8-dendron for targeting. *J. Am. Chem. Soc* *132*, 12829–12831.
- Lewis, C.E., De Palma, M., and Naldini, L. (2007). Tie2-expressing monocytes and tumor angiogenesis: regulation by hypoxia and angiopoietin-2. *Cancer Res* *67*, 8429–8432.
- Li, X., Zheng, Z., Mao, Y., and Ma, X. (2012). Unfractionated heparin promotes LPS-induced endothelial barrier dysfunction: A preliminary study on the roles of angiopoietin/Tie2 axis. *Thrombosis Research*.
- Lim, W.A. (2010). Designing customized cell signalling circuits. *Nat. Rev. Mol. Cell Biol* *11*, 393–403.

- Lin, Y.J., and Koretsky, A.P. (1997). Manganese ion enhances T1-weighted MRI during brain activation: an approach to direct imaging of brain function. *Magn Reson Med* 38, 378–388.
- Lino, M., Merlo, A., and Boulay, J.-L. (2010). Notch signaling in glioblastoma: a developmental drug target? *BMC Medicine* 8, 72.
- Liu, A., Joyner, A.L., and Turnbull, D.H. (1998). Alteration of limb and brain patterning in early mouse embryos by ultrasound-guided injection of Shh-expressing cells. *Mech. Dev* 75, 107–115.
- Llopis, J., McCaffery, J.M., Miyawaki, A., Farquhar, M.G., and Tsien, R.Y. (1998). Measurement of cytosolic, mitochondrial, and Golgi pH in single living cells with green fluorescent proteins. *Proc. Natl. Acad. Sci. U.S.A.* 95, 6803–6808.
- Louie, A.Y., Huber, M.M., Ahrens, E.T., Rothbacher, U., Moats, R., Jacobs, R.E., Fraser, S.E., and Meade, T.J. (2000). In vivo visualization of gene expression using magnetic resonance imaging. *Nat Biotech* 18, 321–325.
- Majmundar, A.J., Wong, W.J., and Simon, M.C. (2010). Hypoxia-Inducible Factors and the Response to Hypoxic Stress. *Molecular Cell* 40, 294–309.
- Mao, J., McKean, D.M., Warriar, S., Corbin, J.G., Niswander, L., and Zohn, I.E. (2010). The iron exporter ferroportin 1 is essential for development of the mouse embryo, forebrain patterning and neural tube closure. *Development* 137, 3079–3088.
- Massaad, C.A., and Pautler, R.G. (2011). Manganese-enhanced magnetic resonance imaging (MEMRI). *Methods Mol. Biol* 711, 145–174.
- McCarthy, J.R., and Weissleder, R. (2008). Multifunctional magnetic nanoparticles for targeted imaging and therapy. *Adv. Drug Deliv. Rev* 60, 1241–1251.
- Mederos y Schnitzler, M., Storch, U., and Gudermann, T. (2011). AT1 receptors as mechanosensors. *Curr Opin Pharmacol* 11, 112–116.
- Minami, T., Kuivenhoven, J.A., Evans, V., Kodama, T., Rosenberg, R.D., and Aird, W.C. (2003). Ets motifs are necessary for endothelial cell-specific expression of a 723-bp Tie-2 promoter/enhancer in Hprt targeted transgenic mice. *Arterioscler. Thromb. Vasc. Biol* 23, 2041–2047.

- Mok, S.I., Munasinghe, J.P., and Young, W.S. (2012). Infusion-based manganese-enhanced MRI: a new imaging technique to visualize the mouse brain. *Brain Struct Funct* *217*, 107–114.
- Moore, A., Basilion, J.P., Chiocca, E.A., and Weissleder, R. (1998). Measuring transferrin receptor gene expression by NMR imaging. *Biochim. Biophys. Acta* *1402*, 239–249.
- Moos, T., and Morgan, E.H. (2000). Transferrin and transferrin receptor function in brain barrier systems. *Cell. Mol. Neurobiol* *20*, 77–95.
- Morello, M., Canini, A., Mattioli, P., Sorge, R.P., Alimonti, A., Bocca, B., Forte, G., Martorana, A., Bernardi, G., and Sancesario, G. (2008). Sub-cellular localization of manganese in the basal ganglia of normal and manganese-treated rats: An electron spectroscopy imaging and electron energy-loss spectroscopy study. *NeuroToxicology* *29*, 60–72.
- Morris, S.M., Jr, Bhamidipati, D., and Kepka-Lenhart, D. (1997). Human type II arginase: sequence analysis and tissue-specific expression. *Gene* *193*, 157–161.
- Motoike, T., Loughna, S., Perens, E., Roman, B.L., Liao, W., Chau, T.C., Richardson, C.D., Kawate, T., Kuno, J., Weinstein, B.M., et al. (2000). Universal GFP reporter for the study of vascular development. *Genesis* *28*, 75–81.
- Mukhopadhyay, S., and Linstedt, A.D. (2012). Manganese blocks intracellular trafficking of Shiga toxin and protects against Shiga toxicosis. *Science* *335*, 332–335.
- Murshid, A., and Presley, J.F. (2004). ER-to-Golgi transport and cytoskeletal interactions in animal cells. *Cell. Mol. Life Sci.* *61*, 133–145.
- Nakamura, C., Kikuchi, T., Burgess, J.G., and Matsunaga, T. (1995). Iron-regulated expression and membrane localization of the magA protein in *Magnetospirillum* sp. strain AMB-1. *J. Biochem* *118*, 23–27.
- Narita, K., Kawasaki, F., and Kita, H. (1990). Mn and Mg influxes through Ca channels of motor nerve terminals are prevented by verapamil in frogs. *Brain Research* *510*, 289–295.
- Nieman, B.J., Bishop, J., Dazai, J., Bock, N.A., Lerch, J.P., Feintuch, A., Chen, X.J., Sled, J.G., and Henkelman, R.M. (2007). MR technology for biological studies in mice. *NMR Biomed* *20*, 291–303.

- Nieman, B.J., Szulc, K.U., and Turnbull, D.H. (2009). Three-dimensional, in vivo MRI with self-gating and image coregistration in the mouse. *Magn Reson Med* *61*, 1148–1157.
- Niethammer, P., Grabher, C., Look, A.T., and Mitchison, T.J. (2009). A tissue-scale gradient of hydrogen peroxide mediates rapid wound detection in zebrafish. *Nature* *459*, 996–999.
- Nishimura, D.G. (1996). *Principles of magnetic resonance imaging* (Stanford University).
- De Palma, M., and Naldini, L. (2011). Angiopoietin-2 TIEs Up Macrophages in Tumor Angiogenesis. *Clin Cancer Res*.
- De Palma, M., Venneri, M.A., Galli, R., Sergi Sergi, L., Politi, L.S., Sampaolesi, M., and Naldini, L. (2005). Tie2 identifies a hematopoietic lineage of proangiogenic monocytes required for tumor vessel formation and a mesenchymal population of pericyte progenitors. *Cancer Cell* *8*, 211–226.
- Paproski, R.J., Forbrich, A.E., Wachowicz, K., Hitt, M.M., and Zemp, R.J. (2011). Tyrosinase as a dual reporter gene for both photoacoustic and magnetic resonance imaging. *Biomed Opt Express* *2*, 771–780.
- Patzer, S.I., and Hantke, K. (2001). Dual repression by Fe(2+)-Fur and Mn(2+)-MntR of the *mntH* gene, encoding an NRAMP-like Mn(2+) transporter in *Escherichia coli*. *J. Bacteriol* *183*, 4806–4813.
- Pautler, R.G. (2004). In vivo, trans-synaptic tract-tracing utilizing manganese-enhanced magnetic resonance imaging (MEMRI). *NMR Biomed* *17*, 595–601.
- Pautler, R.G. (2006). Biological applications of manganese-enhanced magnetic resonance imaging. *Methods Mol. Med.* *124*, 365–386.
- Pautler, R.G., Silva, A.C., and Koretsky, A.P. (1998). In vivo neuronal tract tracing using manganese-enhanced magnetic resonance imaging. *Magn Reson Med* *40*, 740–748.
- Phoon, C.K.L. (2006). Imaging tools for the developmental biologist: ultrasound biomicroscopy of mouse embryonic development. *Pediatr. Res* *60*, 14–21.

- Phoon, C.K.L., and Turnbull, D.H. (2003). Ultrasound biomicroscopy-Doppler in mouse cardiovascular development. *Physiol. Genomics* 14, 3–15.
- Picard, V., Govoni, G., Jabado, N., and Gros, P. (2000). Nramp 2 (DCT1/DMT1) expressed at the plasma membrane transports iron and other divalent cations into a calcein-accessible cytoplasmic pool. *J. Biol. Chem* 275, 35738–35745.
- Prescher, J.A., and Contag, C.H. (2010). Guided by the light: visualizing biomolecular processes in living animals with bioluminescence. *Curr Opin Chem Biol* 14, 80–89.
- Pucci, F., Venneri, M.A., Biziato, D., Nonis, A., Moi, D., Sica, A., Di Serio, C., Naldini, L., and De Palma, M. (2009). A distinguishing gene signature shared by tumor-infiltrating Tie2-expressing monocytes, blood “resident” monocytes, and embryonic macrophages suggests common functions and developmental relationships. *Blood* 114, 901–914.
- Purcell, E.M. (1985). *Electricity and magnetism* (McGraw-Hill).
- Ramakrishnan, B., Ramasamy, V., and Qasba, P.K. (2006). Structural snapshots of beta-1,4-galactosyltransferase-I along the kinetic pathway. *J. Mol. Biol* 357, 1619–1633.
- Ribatti, D. (2009). The paracrine role of Tie-2-expressing monocytes in tumor angiogenesis. *Stem Cells Dev* 18, 703–706.
- Richer, E., Courville, P., Bergevin, I., and Cellier, M.F.M. (2003). Horizontal gene transfer of “prototype” Nramp in bacteria. *J. Mol. Evol* 57, 363–376.
- Rivinoja, A., Hassinen, A., Kokkonen, N., Kauppila, A., and Kellokumpu, S. (2009). Elevated Golgi pH impairs terminal N-glycosylation by inducing mislocalization of Golgi glycosyltransferases. *J. Cell. Physiol.* 220, 144–154.
- de Roos, A., Doornbos, J., Baleriaux, D., Bloem, H.L., and Falke, T.H. (1988). Clinical applications of gadolinium-DTPA in MRI. *Magn Reson Annu* 113–145.
- Roth, J.A., and Garrick, M.D. (2003). Iron interactions and other biological reactions mediating the physiological and toxic actions of manganese. *Biochemical Pharmacology* 66, 1–13.

- Rowland, D.J., and Cherry, S.R. (2008). Small-animal preclinical nuclear medicine instrumentation and methodology. *Semin Nucl Med* 38, 209–222.
- Rüegg, C., and Alghisi, G.C. (2010). Vascular integrins: therapeutic and imaging targets of tumor angiogenesis. *Recent Results Cancer Res* 180, 83–101.
- Saito, T. (2010). Embryonic in vivo electroporation in the mouse. *Meth. Enzymol* 477, 37–50.
- Schlaeger, T.M., Bartunkova, S., Lawitts, J.A., Teichmann, G., Risau, W., Deutsch, U., and Sato, T.N. (1997). Uniform vascular-endothelial-cell-specific gene expression in both embryonic and adult transgenic mice. *Proc. Natl. Acad. Sci. U.S.A* 94, 3058–3063.
- Sepúlveda, M.R., Vanoevelen, J., Raeymaekers, L., Mata, A.M., and Wuytack, F. (2009). Silencing the SPCA1 (secretory pathway Ca²⁺-ATPase isoform 1) impairs Ca²⁺ homeostasis in the Golgi and disturbs neural polarity. *J. Neurosci* 29, 12174–12182.
- Shakibaei, M., Csaki, C., and Mobasheri, A. (2008). Diverse roles of integrin receptors in articular cartilage. *Adv Anat Embryol Cell Biol* 197, 1–60.
- Shimoda, H. (2009). Immunohistochemical demonstration of Angiopoietin-2 in lymphatic vascular development. *Histochem. Cell Biol* 131, 231–238.
- Silva, A.C., Lee, J.H., Aoki, I., and Koretsky, A.P. (2004). Manganese-enhanced magnetic resonance imaging (MEMRI): methodological and practical considerations. *NMR Biomed* 17, 532–543.
- Song, H., Suehiro, J., Kanki, Y., Kawai, Y., Inoue, K., Daida, H., Yano, K., Ohhashi, T., Oettgen, P., Aird, W.C., et al. (2009). Critical role for GATA3 in mediating Tie2 expression and function in large vessel endothelial cells. *J. Biol. Chem.* 284, 29109–29124.
- Sprinzak, D., Lakhanpal, A., LeBon, L., Santat, L.A., Fontes, M.E., Anderson, G.A., Garcia-Ojalvo, J., and Elowitz, M.B. (2010). Cis-interactions between Notch and Delta generate mutually exclusive signalling states. *Nature* 465, 86–90.
- Stefater III, J.A., Lewkowich, I., Rao, S., Mariggi, G., Carpenter, A.C., Burr, A.R., Fan, J., Ajima, R., Molkenstin, J.D., Williams, B.O., et al. (2011).

Regulation of angiogenesis by a non-canonical Wnt-Flt1 pathway in myeloid cells. *Nature* 474, 511–515.

- Stewart, A.J., Morgan, K., Farquharson, C., and Millar, R.P. (2007). Phospholipase C-eta enzymes as putative protein kinase C and Ca²⁺ signalling components in neuronal and neuroendocrine tissues. *Neuroendocrinology* 86, 243–248.
- Stollman, T.H., Ruers, T.J.M., Oyen, W.J.G., and Boerman, O.C. (2009). New targeted probes for radioimaging of angiogenesis. *Methods* 48, 188–192.
- Strauch, R.C., Mastarone, D.J., Sukerkar, P.A., Song, Y., Ipsaro, J.J., and Meade, T.J. (2011). Reporter Protein-Targeted Probes for Magnetic Resonance Imaging. *Journal of the American Chemical Society*.
- Struhl, G., and Adachi, A. (1998). Nuclear access and action of notch in vivo. *Cell* 93, 649–660.
- Takalkar, A.M., Klibanov, A.L., Rychak, J.J., Lindner, J.R., and Ley, K. (2004). Binding and detachment dynamics of microbubbles targeted to P-selectin under controlled shear flow. *J Control Release* 96, 473–482.
- Takata, F., Dohgu, S., Matsumoto, J., Takahashi, H., Machida, T., Wakigawa, T., Harada, E., Miyaji, H., Koga, M., Nishioku, T., et al. (2011). Brain pericytes among cells constituting the blood-brain barrier are highly sensitive to tumor necrosis factor-alpha, releasing matrix metalloproteinase-9 and migrating in vitro. *J Neuroinflammation* 8, 106.
- Tannous, B.A., Grimm, J., Perry, K.F., Chen, J.W., Weissleder, R., and Breakefield, X.O. (2006). Metabolic biotinylation of cell surface receptors for in vivo imaging. *Nat. Methods* 3, 391–396.
- Troadec, M.-B., Ward, D.M., Lo, E., Kaplan, J., and De Domenico, I. (2010). Induction of FPN1 transcription by MTF-1 reveals a role for ferroportin in transition metal efflux. *Blood* 116, 4657–4664.
- Tsien, R.Y. (1998). THE GREEN FLUORESCENT PROTEIN. *Annu. Rev. Biochem.* 67, 509–544.
- Turnbull, D.H., and Mori, S. (2007). MRI in mouse developmental biology. *NMR Biomed* 20, 265–274.

- Vyas, N.K., Nickitenko, A., Rastogi, V.K., Shah, S.S., and Quioco, F.A. (2010). Structural insights into the dual activities of the nerve agent degrading organophosphate anhydrolase/prolidase. *Biochemistry* *49*, 547–559.
- Wadghiri, Y.Z., Blind, J.A., Duan, X., Moreno, C., Yu, X., Joyner, A.L., and Turnbull, D.H. (2004). Manganese-enhanced magnetic resonance imaging (MEMRI) of mouse brain development. *NMR Biomed.* *17*, 613–619.
- Wan, X.S., Devalaraja, M.N., and St Clair, D.K. (1994). Molecular structure and organization of the human manganese superoxide dismutase gene. *DNA Cell Biol* *13*, 1127–1136.
- Wängler, C., Moldenhauer, G., Saffrich, R., Knapp, E.-M., Beijer, B., Schnölzer, M., Wängler, B., Eisenhut, M., Haberkorn, U., and Mier, W. (2008). PAMAM structure-based multifunctional fluorescent conjugates for improved fluorescent labelling of biomacromolecules. *Chemistry* *14*, 8116–8130.
- Waters, L.S., Sandoval, M., and Storz, G. (2011). The *Escherichia coli* MntR mini regulon includes genes encoding a small protein and an efflux pump required for manganese homeostasis. *J Bacteriol.*
- Weissleder, R., Simonova, M., Bogdanova, A., Bredow, S., Enochs, W.S., and Bogdanov, A. (1997). MR imaging and scintigraphy of gene expression through melanin induction. *Radiology* *204*, 425–429.
- Westmeyer, G.G., Durocher, Y., and Jasanoff, A. (2010). A secreted enzyme reporter system for MRI. *Angew. Chem. Int. Ed. Engl* *49*, 3909–3911.
- Willmann, J.K., Paulmurugan, R., Chen, K., Gheysens, O., Rodriguez-Porcel, M., Lutz, A.M., Chen, I.Y., Chen, X., and Gambhir, S.S. (2008). US imaging of tumor angiogenesis with microbubbles targeted to vascular endothelial growth factor receptor type 2 in mice. *Radiology* *246*, 508–518.
- Winter, P.M., Caruthers, S.D., Kassner, A., Harris, T.D., Chinen, L.K., Allen, J.S., Lacy, E.K., Zhang, H., Robertson, J.D., Wickline, S.A., et al. (2003). Molecular imaging of angiogenesis in nascent Vx-2 rabbit tumors using a novel alpha(nu)beta3-targeted nanoparticle and 1.5 tesla magnetic resonance imaging. *Cancer Res* *63*, 5838–5843.

- Wu, L.J., Leenders, A.G.M., Cooperman, S., Meyron-Holtz, E., Smith, S., Land, W., Tsai, R.Y.L., Berger, U.V., Sheng, Z.-H., and Rouault, T.A. (2004). Expression of the iron transporter ferroportin in synaptic vesicles and the blood-brain barrier. *Brain Res* 1001, 108–117.
- Xiang, M., Mohamalawari, D., and Rao, R. (2005). A Novel Isoform of the Secretory Pathway Ca^{2+} , Mn^{2+} -ATPase, hSPCA2, Has Unusual Properties and Is Expressed in the Brain. *Journal of Biological Chemistry* 280, 11608–11614.
- Yokel, R.A., Crossgrove, J.S., and Bukaveckas, B.L. (2003). Manganese Distribution Across the Blood-Brain Barrier: II. Manganese Efflux From the Brain Does not Appear to be Carrier Mediated. *NeuroToxicology* 24, 15–22.
- Yoshino, T., Maeda, Y., and Matsunag, T. (2010). Bioengineering of bacterial magnetic particles and their applications in biotechnology. *Recent Pat Biotechnol* 4, 214–225.
- Yu, X., Wadghiri, Y.Z., Sanes, D.H., and Turnbull, D.H. (2005). In vivo auditory brain mapping in mice with Mn-enhanced MRI. *Nat. Neurosci* 8, 961–968.
- Zhang, Y., Kang, Y.-H., Chang, N., Lam, P.P.L., Liu, Y., Olkkonen, V.M., and Gaisano, H.Y. (2009). Cab45b, a Munc18b-interacting partner, regulates exocytosis in pancreatic beta-cells. *J. Biol. Chem* 284, 20840–20847.
- Zheng, W., Aschner, M., and Gherzi-Egea, J.-F. (2003). Brain barrier systems: a new frontier in metal neurotoxicological research. *Toxicol. Appl. Pharmacol* 192, 1–11.
- Ziv, K., Meir, G., Harmelin, A., Shimoni, E., Klein, E., and Neeman, M. (2010). Ferritin as a reporter gene for MRI: chronic liver over expression of h-ferritin during dietary iron supplementation and aging. *NMR Biomed.* 23, 523–531.
- Agarwal, A. et al., 2008. Ligand based dendritic systems for tumor targeting. *International Journal of Pharmaceutics*, 350(1-2), pp.3–13.
- Aisen, P., 2004. Transferrin receptor 1. *The International Journal of Biochemistry & Cell Biology*, 36(11), pp.2137–2143.

- Akhtar, N., Dickerson, E.B. & Auerbach, R., 2002. The sponge/Matrigel angiogenesis assay. *Angiogenesis*, 5(1-2), pp.75–80.
- Aoki, I. et al., 2004. In vivo detection of neuroarchitecture in the rodent brain using manganese-enhanced MRI. *NeuroImage*, 22(3), pp.1046–1059.
- Arnadóttir, J. & Chalfie, Martin, 2010. Eukaryotic mechanosensitive channels. *Annual Review of Biophysics*, 39, pp.111–137.
- Artemov, D., 2003. Molecular magnetic resonance imaging with targeted contrast agents. *Journal of Cellular Biochemistry*, 90(3), pp.518–524.
- Asahara, H., Nameki, N. & Hasegawa, T., 1998. In vitro selection of RNAs aminoacylated by Escherichia coli leucyl-tRNA synthetase. *Journal of Molecular Biology*, 283(3), pp.605–618.
- Aschner, M., Vrana, K.E. & Zheng, W., 1999. Manganese uptake and distribution in the central nervous system (CNS). *NeuroToxicology*, 20(2-3), pp.173–180.
- Bagautdinov, B. et al., 2008. Protein Biotinylation Visualized by a Complex Structure of Biotin Protein Ligase with a Substrate. *Journal of Biological Chemistry*, 283(21), pp.14739 –14750.
- Bai, S.P. et al., 2008. Kinetics of Manganese Absorption in Ligated Small Intestinal Segments of Broilers. *Poult Sci*, 87(12), pp.2596–2604.
- Beckett, D., Kovaleva, E. & Schatz, P.J., 1999. A minimal peptide substrate in biotin holoenzyme synthetase-catalyzed biotinylation. *Protein Science: A Publication of the Protein Society*, 8(4), pp.921–929.
- Berrios-Otero, Cesar A et al., 2011. In utero phenotyping of mouse embryonic vasculature with MRI. *Magnetic Resonance in Medicine*. Available at: <http://www.ncbi.nlm.nih.gov/pubmed/21590728> [Accessed September 13, 2011].
- Berrios-Otero, Cesar A et al., 2009. Three-dimensional micro-MRI analysis of cerebral artery development in mouse embryos. *Magnetic Resonance in Medicine*, 62(6), pp.1431–1439.
- Bloch, F., 1953. *The principle of nuclear induction*, Kungl. boktryckeriet P.A. Norstedt & söner.

- Bock, N.A., Paiva, F.F. & Silva, Afonso C, 2008. Fractionated manganese-enhanced MRI. *NMR in Biomedicine*, 21(5), pp.473–478.
- Bourboulia, D. & Stetler-Stevenson, W.G., 2010. Matrix metalloproteinases (MMPs) and tissue inhibitors of metalloproteinases (TIMPs): Positive and negative regulators in tumor cell adhesion. *Seminars in Cancer Biology*, 20(3), pp.161–168.
- Boutin, C. et al., 2008. Efficient in vivo electroporation of the postnatal rodent forebrain. *PloS One*, 3(4), p.e1883.
- Bulte, J.W.M. & Kraitchman, D.L., 2004. Iron oxide MR contrast agents for molecular and cellular imaging. *NMR in Biomedicine*, 17(7), pp.484–499.
- Carmona, A. et al., 2010. Manganese Accumulates within Golgi Apparatus in Dopaminergic Cells as Revealed by Synchrotron X-ray Fluorescence Nanoimaging. *ACS Chemical Neuroscience*, 1(3), pp.194–203.
- Cha, S. et al., 2003. Dynamic, contrast-enhanced perfusion MRI in mouse gliomas: Correlation with histopathology. *Magnetic Resonance in Medicine*, 49(5), pp.848–855.
- Chae, J.K. et al., 2000. Coadministration of angiopoietin-1 and vascular endothelial growth factor enhances collateral vascularization. *Arteriosclerosis, Thrombosis, and Vascular Biology*, 20(12), pp.2573–2578.
- Chalfie, M et al., 1994. Green fluorescent protein as a marker for gene expression. *Science (New York, N.Y.)*, 263(5148), pp.802–805.
- Chasteen, N.D. & Harrison, P.M., 1999. Mineralization in ferritin: an efficient means of iron storage. *Journal of Structural Biology*, 126(3), pp.182–194.
- Cheng, Y. et al., 2004. Structure of the Human Transferrin Receptor-Transferrin Complex. *Cell*, 116(4), pp.565–576.
- Cho, C.-H. et al., 2006. COMP-angiopoietin-1 promotes wound healing through enhanced angiogenesis, lymphangiogenesis, and blood flow in a diabetic mouse model. *Proceedings of the National Academy of Sciences of the United States of America*, 103(13), pp.4946–4951.

- Cho, M., Hunt, T.K. & Hussain, M.Z., 2001. Hydrogen peroxide stimulates macrophage vascular endothelial growth factor release. *American Journal of Physiology - Heart and Circulatory Physiology*, 280(5), pp.H2357 –H2363.
- Christensen, R.A. et al., 2002. NERF2, a member of the Ets family of transcription factors, is increased in response to hypoxia and angiotensin-1: A potential mechanism for Tie2 regulation during hypoxia. *Journal of Cellular Biochemistry*, 85(3), pp.505–515.
- Cohen, B. et al., 2007. MRI detection of transcriptional regulation of gene expression in transgenic mice. *Nat Med*, 13(4), pp.498–503.
- Corneillie, T.M., Fisher, A.J. & Meares, C.F., 2003. Crystal structures of two complexes of the rare-earth-DOTA-binding antibody 2D12.5: ligand generality from a chiral system. *Journal of the American Chemical Society*, 125(49), pp.15039–15048.
- Corsi, B. et al., 2002. Human mitochondrial ferritin expressed in HeLa cells incorporates iron and affects cellular iron metabolism. *The Journal of Biological Chemistry*, 277(25), pp.22430–22437.
- Crossgrove, J.S. & Yokel, R.A., 2004. Manganese Distribution Across the Blood-Brain Barrier III: The Divalent Metal Transporter-1 is not the Major Mechanism Mediating Brain Manganese Uptake. *NeuroToxicology*, 25(3), pp.451–460.
- Crossgrove, J.S. & Yokel, R.A., 2005. Manganese distribution across the blood-brain barrier: IV. Evidence for brain influx through store-operated calcium channels. *NeuroToxicology*, 26(3), pp.297–307.
- Deans, A.E. et al., 2006. Cellular MRI contrast via coexpression of transferrin receptor and ferritin. *Magnetic Resonance in Medicine*, 56(1), pp.51–59.
- Deans, A.E. et al., 2008. Mn enhancement and respiratory gating for in utero MRI of the embryonic mouse central nervous system. *Magnetic Resonance in Medicine*, 59(6), pp.1320–1328.
- Devasahayam, G., Burke, D.J. & Sturgill, T.W., 2007. Golgi manganese transport is required for rapamycin signaling in *Saccharomyces cerevisiae*. *Genetics*, 177(1), pp.231–238.

- Diamandis, E.P. & Christopoulos, T.K., 1991. The biotin-(strept)avidin system: principles and applications in biotechnology. *Clinical Chemistry*, 37(5), pp.625–636.
- Dorr, A.E. et al., 2008. High resolution three-dimensional brain atlas using an average magnetic resonance image of 40 adult C57Bl/6J mice. *NeuroImage*, 42(1), pp.60–69.
- Downes, C.E. & Crack, P.J., 2010. Neural injury following stroke: are Toll-like receptors the link between the immune system and the CNS? *British Journal of Pharmacology*, p.no–no.
- Dunphy, M.P.S. et al., 2009. In vivo microcartography and subcellular imaging of tumor angiogenesis: a novel platform for translational angiogenesis research. *Microvascular Research*, 78(1), pp.51–56.
- Ellegala, D.B. et al., 2003. Imaging tumor angiogenesis with contrast ultrasound and microbubbles targeted to alpha(v)beta3. *Circulation*, 108(3), pp.336–341.
- Eun Kim, K. et al., 2007. In Vivo Actions of Angiopoietins on Quiescent and Remodeling Blood and Lymphatic Vessels in Mouse Airways and Skin. *Arterioscler Thromb Vasc Biol*, 27(3), pp.564–570.
- Fernández-Suárez, M., Chen, T.S. & Ting, A.Y., 2008. Protein-protein interaction detection in vitro and in cells by proximity biotinylation. *Journal of the American Chemical Society*, 130(29), pp.9251–9253.
- Ferrara, N. & Kerbel, R.S., 2005. Angiogenesis as a therapeutic target. *Nature*, 438(7070), pp.967–974.
- Fiedler, U. et al., 2006. Angiopoietin-2 sensitizes endothelial cells to TNF-[alpha] and has a crucial role in the induction of inflammation. *Nat Med*, 12(2), pp.235–239.
- Fox, M. & Rabi, I.I., 1935. *On the nuclear moments of lithium, potassium and sodium*, Lancaster press inc.
- Fraser, S.T. et al., 2005. Using a histone yellow fluorescent protein fusion for tagging and tracking endothelial cells in ES cells and mice. *Genesis (New York, N.Y.: 2000)*, 42(3), pp.162–171.

- Fukuhara, S. et al., 2009. Tie2 is tied at the cell-cell contacts and to extracellular matrix by Angiopoietin-1. *Experimental & Molecular Medicine*, 41(3), pp.133–139.
- Gaiano, N. et al., 1999. A method for rapid gain-of-function studies in the mouse embryonic nervous system. *Nat Neurosci*, 2(9), pp.812–819.
- Gamble, J.R. et al., 2000. Angiopoietin-1 Is an Antipermeability and Anti-Inflammatory Agent In Vitro and Targets Cell Junctions. *Circ Res*, 87(7), pp.603–607.
- Garcia-Diaz, M. et al., 2007. Role of the catalytic metal during polymerization by DNA polymerase lambda. *DNA Repair*, 6(9), pp.1333–1340.
- Garrick, M.D. et al., 2006. Comparison of mammalian cell lines expressing distinct isoforms of divalent metal transporter 1 in a tetracycline-regulated fashion. *Biochemical Journal*, 398(3), p.539.
- Genove, G. et al., 2005. A new transgene reporter for in vivo magnetic resonance imaging. *Nat Med*, 11(43), pp.450–454.
- Gervais, L. et al., 2008. PIP5K-dependent production of PIP2 sustains microtubule organization to establish polarized transport in the *Drosophila* oocyte. *Development (Cambridge, England)*, 135(23), pp.3829–3838.
- Gilad, A.A., McMahon, M.T., et al., 2007. Artificial reporter gene providing MRI contrast based on proton exchange. *Nat Biotech*, 25(2), pp.217–219.
- Gilad, A.A., Winnard, P.T., Jr, et al., 2007. Developing MR reporter genes: promises and pitfalls. *NMR in Biomedicine*, 20(3), pp.275–290.
- Glasfeld, A. et al., 2003. Structure of the manganese-bound manganese transport regulator of *Bacillus subtilis*. *Nature Structural Biology*, 10(8), pp.652–657.
- Goldhawk, D.E. et al., 2009. Magnetic resonance imaging of cells overexpressing MagA, an endogenous contrast agent for live cell imaging. *Molecular Imaging*, 8(3), pp.129–139.
- Golynskiy, M.V. et al., 2005. Metal-induced structural organization and stabilization of the metalloregulatory protein MntR. *Biochemistry*, 44(9), pp.3380–3389.

- Guan, Y. et al., 1998. Crystal structure of Y34F mutant human mitochondrial manganese superoxide dismutase and the functional role of tyrosine 34. *Biochemistry*, 37(14), pp.4722–4730.
- Haacke, E., 1999. *Magnetic resonance imaging: physical principles and sequence design*, New York: J. Wiley & Sons.
- Hielscher, A.H., 2005. Optical tomographic imaging of small animals. *Current Opinion in Biotechnology*, 16(1), pp.79–88.
- Hilderbrand, S.A. & Weissleder, Ralph, 2010. Near-infrared fluorescence: application to in vivo molecular imaging. *Current Opinion in Chemical Biology*, 14(1), pp.71–79.
- Hughes, D.P., Marron, M.B. & Brindle, N.P.J., 2003. The antiinflammatory endothelial tyrosine kinase Tie2 interacts with a novel nuclear factor-kappaB inhibitor ABIN-2. *Circulation Research*, 92(6), pp.630–636.
- Ilies, M. et al., 2010. 2-aminoimidazole amino acids as inhibitors of the binuclear manganese metalloenzyme human arginase I. *Journal of Medicinal Chemistry*, 53(10), pp.4266–4276.
- Iordanova, B., Robison, C.S. & Ahrens, E.T., 2010a. Design and characterization of a chimeric ferritin with enhanced iron loading and transverse NMR relaxation rate. *Journal of Biological Inorganic Chemistry: JBIC: A Publication of the Society of Biological Inorganic Chemistry*, 15(6), pp.957–965.
- Iordanova, B., Robison, C.S. & Ahrens, E.T., 2010b. Design and characterization of a chimeric ferritin with enhanced iron loading and transverse NMR relaxation rate. *JBIC Journal of Biological Inorganic Chemistry*, 15(6), pp.957–965.
- Irie, S. & Tavassoli, M., 1987. Transferrin-mediated cellular iron uptake. *The American Journal of the Medical Sciences*, 293(2), pp.103–111.
- Johnson, E. et al., 2005. Crystal structures of a tetrahedral open pore ferritin from the hyperthermophilic archaeon *Archaeoglobus fulgidus*. *Structure (London, England: 1993)*, 13(4), pp.637–648.
- Kessler, S., Clauss, W.G. & Fronius, M., 2011. Lamina shear stress modulates the activity of heterologously expressed P2X(4) receptors. *Biochimica Et Biophysica Acta*, 1808(10), pp.2488–2495.

- Kliegman, J.I. et al., 2006. Structural basis for the metal-selective activation of the manganese transport regulator of *Bacillus subtilis*. *Biochemistry*, 45(11), pp.3493–3505.
- Krajewski, W.W. et al., 2008. Crystal structures of mammalian glutamine synthetases illustrate substrate-induced conformational changes and provide opportunities for drug and herbicide design. *Journal of Molecular Biology*, 375(1), pp.217–228.
- Krause, W., 2002. *Contrast Agents I: Magnetic Resonance Imaging*, Berlin: Springer.
- Kung, C., Martinac, B. & Sukharev, S., 2010. Mechanosensitive channels in microbes. *Annual Review of Microbiology*, 64, pp.313–329.
- Laitinen, O.H. et al., 2007. Brave new (strept)avidins in biotechnology. *Trends in Biotechnology*, 25(6), pp.269–277.
- Lam, P.P.L. et al., 2007. A cytosolic splice variant of Cab45 interacts with Munc18b and impacts on amylase secretion by pancreatic acini. *Molecular Biology of the Cell*, 18(7), pp.2473–2480.
- Lam-Yuk-Tseung, S. & Gros, Philippe, 2006. Distinct targeting and recycling properties of two isoforms of the iron transporter DMT1 (NRAMP2, Slc11A2). *Biochemistry*, 45(7), pp.2294–2301.
- Larina, I.V. et al., 2009. A membrane associated mCherry fluorescent reporter line for studying vascular remodeling and cardiac function during murine embryonic development. *Anatomical Record (Hoboken, N.J.: 2007)*, 292(3), pp.333–341.
- Lauterbur, P.C., 1973. Image Formation by Induced Local Interactions: Examples Employing Nuclear Magnetic Resonance. *Nature*, 242(5394), pp.190–191.
- De León-Rodríguez, L.M. et al., 2010. MRI detection of VEGFR2 in vivo using a low molecular weight peptoid-(Gd)³⁺-dendron for targeting. *Journal of the American Chemical Society*, 132(37), pp.12829–12831.
- Lewis, C.E., De Palma, M. & Naldini, L., 2007. Tie2-expressing monocytes and tumor angiogenesis: regulation by hypoxia and angiopoietin-2. *Cancer Research*, 67(18), pp.8429–8432.

- Li, X. et al., 2012. Unfractionated heparin promotes LPS-induced endothelial barrier dysfunction: A preliminary study on the roles of angiopoietin/Tie2 axis. *Thrombosis Research*. Available at: <http://www.ncbi.nlm.nih.gov/pubmed/22455983> [Accessed April 24, 2012].
- Lim, W.A., 2010. Designing customized cell signalling circuits. *Nature Reviews. Molecular Cell Biology*, 11(6), pp.393–403.
- Lin, Y.J. & Koretsky, A P, 1997. Manganese ion enhances T1-weighted MRI during brain activation: an approach to direct imaging of brain function. *Magnetic Resonance in Medicine: Official Journal of the Society of Magnetic Resonance in Medicine / Society of Magnetic Resonance in Medicine*, 38(3), pp.378–388.
- Lino, M., Merlo, A. & Boulay, J.-L., 2010. Notch signaling in glioblastoma: a developmental drug target? *BMC Medicine*, 8(1), p.72.
- Liu, A., Joyner, A L & Turnbull, D H, 1998. Alteration of limb and brain patterning in early mouse embryos by ultrasound-guided injection of Shh-expressing cells. *Mechanisms of Development*, 75(1-2), pp.107–115.
- Livnah, O. et al., 1993. Three-dimensional structures of avidin and the avidin-biotin complex. *Proceedings of the National Academy of Sciences of the United States of America*, 90(11), pp.5076–5080.
- Llopis, J. et al., 1998. Measurement of cytosolic, mitochondrial, and Golgi pH in single living cells with green fluorescent proteins. *Proceedings of the National Academy of Sciences of the United States of America*, 95(12), pp.6803–6808.
- Louie, A.Y. et al., 2000. In vivo visualization of gene expression using magnetic resonance imaging. *Nat Biotech*, 18(3), pp.321–325.
- Majmundar, A.J., Wong, W.J. & Simon, M.C., 2010. Hypoxia-Inducible Factors and the Response to Hypoxic Stress. *Molecular Cell*, 40(2), pp.294–309.
- Mao, J. et al., 2010. The iron exporter ferroportin 1 is essential for development of the mouse embryo, forebrain patterning and neural tube closure. *Development*, 137(18), pp.3079 –3088.

- Massaad, C.A. & Pautler, Robia G, 2011. Manganese-enhanced magnetic resonance imaging (MEMRI). *Methods in Molecular Biology (Clifton, N.J.)*, 711, pp.145–174.
- McCarthy, J.R. & Weissleder, Ralph, 2008. Multifunctional magnetic nanoparticles for targeted imaging and therapy. *Advanced Drug Delivery Reviews*, 60(11), pp.1241–1251.
- Mederos y Schnitzler, M., Storch, U. & Gudermann, T., 2011. AT1 receptors as mechanosensors. *Current Opinion in Pharmacology*, 11(2), pp.112–116.
- Minami, T. et al., 2003. Ets motifs are necessary for endothelial cell-specific expression of a 723-bp Tie-2 promoter/enhancer in Hprt targeted transgenic mice. *Arteriosclerosis, Thrombosis, and Vascular Biology*, 23(11), pp.2041–2047.
- Mok, S.I., Munasinghe, J.P. & Young, W.S., 2012. Infusion-based manganese-enhanced MRI: a new imaging technique to visualize the mouse brain. *Brain Structure & Function*, 217(1), pp.107–114.
- Moore, A. et al., 1998. Measuring transferrin receptor gene expression by NMR imaging. *Biochimica Et Biophysica Acta*, 1402(3), pp.239–249.
- Moos, T. & Morgan, E.H., 2000. Transferrin and transferrin receptor function in brain barrier systems. *Cellular and Molecular Neurobiology*, 20(1), pp.77–95.
- Morello, M. et al., 2008. Sub-cellular localization of manganese in the basal ganglia of normal and manganese-treated rats: An electron spectroscopy imaging and electron energy-loss spectroscopy study. *NeuroToxicology*, 29(1), pp.60–72.
- Morris, S.M., Jr, Bhamidipati, D. & Kepka-Lenhart, D., 1997. Human type II arginase: sequence analysis and tissue-specific expression. *Gene*, 193(2), pp.157–161.
- Motoike, T. et al., 2000. Universal GFP reporter for the study of vascular development. *Genesis (New York, N.Y.: 2000)*, 28(2), pp.75–81.
- Mukhopadhyay, S. & Linstedt, A.D., 2012. Manganese blocks intracellular trafficking of Shiga toxin and protects against Shiga toxicosis. *Science (New York, N.Y.)*, 335(6066), pp.332–335.

- Murshid, A. & Presley, J.F., 2004. ER-to-Golgi transport and cytoskeletal interactions in animal cells. *Cellular and Molecular Life Sciences: CMLS*, 61(2), pp.133–145.
- Nakamura, C. et al., 1995. Iron-regulated expression and membrane localization of the magA protein in *Magnetospirillum* sp. strain AMB-1. *Journal of Biochemistry*, 118(1), pp.23–27.
- Narita, K., Kawasaki, F. & Kita, H., 1990. Mn and Mg influxes through Ca channels of motor nerve terminals are prevented by verapamil in frogs. *Brain Research*, 510(2), pp.289–295.
- Nieman, B.J. et al., 2007. MR technology for biological studies in mice. *NMR in Biomedicine*, 20(3), pp.291–303.
- Nieman, B.J., Szulc, K.U. & Turnbull, Daniel H, 2009. Three-dimensional, in vivo MRI with self-gating and image coregistration in the mouse. *Magnetic Resonance in Medicine*, 61(5), pp.1148–1157.
- Niethammer, P. et al., 2009. A tissue-scale gradient of hydrogen peroxide mediates rapid wound detection in zebrafish. *Nature*, 459(7249), pp.996–999.
- Nishimura, D.G., 1996. *Principles of magnetic resonance imaging*, Stanford University.
- De Palma, M. et al., 2005. Tie2 identifies a hematopoietic lineage of proangiogenic monocytes required for tumor vessel formation and a mesenchymal population of pericyte progenitors. *Cancer Cell*, 8(3), pp.211–226.
- De Palma, M. & Naldini, L., 2011. Angiopoietin-2 TIEs Up Macrophages in Tumor Angiogenesis. *Clinical Cancer Research*. Available at: <http://www.ncbi.nlm.nih.gov/pubmed/21576085> [Accessed June 8, 2011].
- Paproski, R.J. et al., 2011. Tyrosinase as a dual reporter gene for both photoacoustic and magnetic resonance imaging. *Biomedical Optics Express*, 2(4), pp.771–780.
- Patzer, S.I. & Hantke, K., 2001. Dual repression by Fe(2+)-Fur and Mn(2+)-MntR of the mntH gene, encoding an NRAMP-like Mn(2+) transporter in *Escherichia coli*. *Journal of Bacteriology*, 183(16), pp.4806–4813.

- Pautler, R G, 2006. Biological applications of manganese-enhanced magnetic resonance imaging. *Methods in Molecular Medicine*, 124, pp.365–386.
- Pautler, R G, Silva, A C & Koretsky, A P, 1998. In vivo neuronal tract tracing using manganese-enhanced magnetic resonance imaging. *Magnetic Resonance in Medicine*, 40(5), pp.740–748.
- Pautler, Robia G, 2004. In vivo, trans-synaptic tract-tracing utilizing manganese-enhanced magnetic resonance imaging (MEMRI). *NMR in Biomedicine*, 17(8), pp.595–601.
- Phoon, Colin K L & Turnbull, Daniel H, 2003. Ultrasound biomicroscopy-Doppler in mouse cardiovascular development. *Physiological Genomics*, 14(1), pp.3–15.
- Phoon, Colin Kit Lun, 2006. Imaging tools for the developmental biologist: ultrasound biomicroscopy of mouse embryonic development. *Pediatric Research*, 60(1), pp.14–21.
- Picard, V. et al., 2000. Nramp 2 (DCT1/DMT1) expressed at the plasma membrane transports iron and other divalent cations into a calcein-accessible cytoplasmic pool. *The Journal of Biological Chemistry*, 275(46), pp.35738–35745.
- Prescher, J.A. & Contag, C.H., 2010. Guided by the light: visualizing biomolecular processes in living animals with bioluminescence. *Current Opinion in Chemical Biology*, 14(1), pp.80–89.
- Pucci, F. et al., 2009. A distinguishing gene signature shared by tumor-infiltrating Tie2-expressing monocytes, blood “resident” monocytes, and embryonic macrophages suggests common functions and developmental relationships. *Blood*, 114(4), pp.901–914.
- Purcell, E.M., 1985. *Electricity and magnetism*, McGraw-Hill.
- Ramakrishnan, B., Ramasamy, V. & Qasba, P.K., 2006. Structural snapshots of beta-1,4-galactosyltransferase-I along the kinetic pathway. *Journal of Molecular Biology*, 357(5), pp.1619–1633.
- Ribatti, D., 2009. The paracrine role of Tie-2-expressing monocytes in tumor angiogenesis. *Stem Cells and Development*, 18(5), pp.703–706.
- Richer, E. et al., 2003. Horizontal gene transfer of “prototype” Nramp in bacteria. *Journal of Molecular Evolution*, 57(4), pp.363–376.

- Rivinoja, A. et al., 2009. Elevated Golgi pH impairs terminal N-glycosylation by inducing mislocalization of Golgi glycosyltransferases. *Journal of Cellular Physiology*, 220(1), pp.144–154.
- de Roos, A. et al., 1988. Clinical applications of gadolinium-DTPA in MRI. *Magnetic Resonance Annual*, pp.113–145.
- Roth, J.A. & Garrick, M.D., 2003. Iron interactions and other biological reactions mediating the physiological and toxic actions of manganese. *Biochemical Pharmacology*, 66(1), pp.1–13.
- Rowland, D.J. & Cherry, S.R., 2008. Small-animal preclinical nuclear medicine instrumentation and methodology. *Seminars in Nuclear Medicine*, 38(3), pp.209–222.
- Rüegg, C. & Alghisi, G.C., 2010. Vascular integrins: therapeutic and imaging targets of tumor angiogenesis. *Recent Results in Cancer Research. Fortschritte Der Krebsforschung. Progrès Dans Les Recherches Sur Le Cancer*, 180, pp.83–101.
- Saito, T., 2010. Embryonic in vivo electroporation in the mouse. *Methods in Enzymology*, 477, pp.37–50.
- Schlaeger, T.M. et al., 1997. Uniform vascular-endothelial-cell-specific gene expression in both embryonic and adult transgenic mice. *Proceedings of the National Academy of Sciences of the United States of America*, 94(7), pp.3058–3063.
- Sepúlveda, M.R. et al., 2009. Silencing the SPCA1 (secretory pathway Ca²⁺-ATPase isoform 1) impairs Ca²⁺ homeostasis in the Golgi and disturbs neural polarity. *The Journal of Neuroscience*, 29(39), pp.12174–12182.
- Shakibaei, M., Csaki, C. & Mobasheri, A., 2008. Diverse roles of integrin receptors in articular cartilage. *Advances in Anatomy, Embryology, and Cell Biology*, 197, pp.1–60.
- Shimoda, H., 2009. Immunohistochemical demonstration of Angiopoietin-2 in lymphatic vascular development. *Histochemistry and Cell Biology*, 131(2), pp.231–238.
- Silva, Afonso C et al., 2004. Manganese-enhanced magnetic resonance imaging (MEMRI): methodological and practical considerations. *NMR in Biomedicine*, 17(8), pp.532–543.

- Song, H. et al., 2009. Critical role for GATA3 in mediating Tie2 expression and function in large vessel endothelial cells. *The Journal of Biological Chemistry*, 284(42), pp.29109–29124.
- Sprinzak, D. et al., 2010. Cis-interactions between Notch and Delta generate mutually exclusive signalling states. *Nature*, 465(7294), pp.86–90.
- Stefater III, J.A. et al., 2011. Regulation of angiogenesis by a non-canonical Wnt-Flt1 pathway in myeloid cells. *Nature*, 474(7352), pp.511–515.
- Stewart, A.J. et al., 2007. Phospholipase C-eta enzymes as putative protein kinase C and Ca²⁺ signalling components in neuronal and neuroendocrine tissues. *Neuroendocrinology*, 86(4), pp.243–248.
- Stollman, T.H. et al., 2009. New targeted probes for radioimaging of angiogenesis. *Methods (San Diego, Calif.)*, 48(2), pp.188–192.
- Strauch, R.C. et al., 2011. Reporter Protein-Targeted Probes for Magnetic Resonance Imaging. *Journal of the American Chemical Society*. Available at: <http://dx.doi.org/10.1021/ja206134b> [Accessed September 30, 2011].
- Struhl, G. & Adachi, A., 1998. Nuclear access and action of notch in vivo. *Cell*, 93(4), pp.649–660.
- Takalkar, A.M. et al., 2004. Binding and detachment dynamics of microbubbles targeted to P-selectin under controlled shear flow. *Journal of Controlled Release*, 96(3), pp.473–482.
- Takata, F. et al., 2011. Brain pericytes among cells constituting the blood-brain barrier are highly sensitive to tumor necrosis factor-alpha, releasing matrix metalloproteinase-9 and migrating in vitro. *Journal of Neuroinflammation*, 8(1), p.106.
- Tannous, B.A. et al., 2006. Metabolic biotinylation of cell surface receptors for in vivo imaging. *Nature Methods*, 3(5), pp.391–396.
- Troadec, M.-B. et al., 2010. Induction of FPN1 transcription by MTF-1 reveals a role for ferroportin in transition metal efflux. *Blood*, 116(22), pp.4657–4664.
- Tsien, Roger Y., 1998. THE GREEN FLUORESCENT PROTEIN. *Annual Review of Biochemistry*, 67(1), pp.509–544.

- Turnbull, Daniel H & Mori, S., 2007. MRI in mouse developmental biology. *NMR in Biomedicine*, 20(3), pp.265–274.
- Vyas, N.K. et al., 2010. Structural insights into the dual activities of the nerve agent degrading organophosphate anhydrolase/prolidase. *Biochemistry*, 49(3), pp.547–559.
- Wadghiri, Y.Z. et al., 2004. Manganese-enhanced magnetic resonance imaging (MEMRI) of mouse brain development. *NMR in Biomedicine*, 17(8), pp.613–619.
- Wan, X.S., Devalaraja, M.N. & St Clair, D.K., 1994. Molecular structure and organization of the human manganese superoxide dismutase gene. *DNA and Cell Biology*, 13(11), pp.1127–1136.
- Wängler, C. et al., 2008. PAMAM structure-based multifunctional fluorescent conjugates for improved fluorescent labelling of biomacromolecules. *Chemistry (Weinheim an Der Bergstrasse, Germany)*, 14(27), pp.8116–8130.
- Waters, L.S., Sandoval, M. & Storz, G., 2011. The Escherichia coli MntR mini regulon includes genes encoding a small protein and an efflux pump required for manganese homeostasis. *Journal of Bacteriology*. Available at: <http://www.ncbi.nlm.nih.gov/pubmed/21908668> [Accessed September 16, 2011].
- Weissleder, R et al., 1997. MR imaging and scintigraphy of gene expression through melanin induction. *Radiology*, 204(2), pp.425 –429.
- Westmeyer, G.G., Durocher, Y. & Jasanoff, A., 2010. A secreted enzyme reporter system for MRI. *Angewandte Chemie (International Ed. in English)*, 49(23), pp.3909–3911.
- Willmann, J.K. et al., 2008. US imaging of tumor angiogenesis with microbubbles targeted to vascular endothelial growth factor receptor type 2 in mice. *Radiology*, 246(2), pp.508–518.
- Winter, P.M. et al., 2003. Molecular imaging of angiogenesis in nascent Vx-2 rabbit tumors using a novel alpha(nu)beta3-targeted nanoparticle and 1.5 tesla magnetic resonance imaging. *Cancer Research*, 63(18), pp.5838–5843.

- Wu, L.J. et al., 2004. Expression of the iron transporter ferroportin in synaptic vesicles and the blood-brain barrier. *Brain Research*, 1001(1-2), pp.108–117.
- Xiang, M., Mohamalawari, D. & Rao, R., 2005. A Novel Isoform of the Secretory Pathway Ca^{2+} , Mn^{2+} -ATPase, hSPCA2, Has Unusual Properties and Is Expressed in the Brain. *Journal of Biological Chemistry*, 280(12), pp.11608 –11614.
- Yokel, R.A., Crossgrove, J.S. & Bukaveckas, B.L., 2003. Manganese Distribution Across the Blood-Brain Barrier: II. Manganese Efflux From the Brain Does not Appear to be Carrier Mediated. *NeuroToxicology*, 24(1), pp.15–22.
- Yoshino, T., Maeda, Y. & Matsunag, T., 2010. Bioengineering of bacterial magnetic particles and their applications in biotechnology. *Recent Patents on Biotechnology*, 4(3), pp.214–225.
- Yu, X. et al., 2005. In vivo auditory brain mapping in mice with Mn-enhanced MRI. *Nature Neuroscience*, 8(7), pp.961–968.
- Zhang, Y. et al., 2009. Cab45b, a Munc18b-interacting partner, regulates exocytosis in pancreatic beta-cells. *The Journal of Biological Chemistry*, 284(31), pp.20840–20847.
- Zheng, Wei, Aschner, Michael & Gherzi-Egea, J.-F., 2003. Brain barrier systems: a new frontier in metal neurotoxicological research. *Toxicology and Applied Pharmacology*, 192(1), pp.1–11.
- Ziv, K. et al., 2010. Ferritin as a reporter gene for MRI: chronic liver over expression of h-ferritin during dietary iron supplementation and aging. *NMR in Biomedicine*, 23(5), pp.523–531.